Summer 2018

Diversity and Petrogenesis of Rhyolites from an Intra-oceanic Arc: Evidence from IODP Site U1437, Izu Bonin Rear-arc and Surrounding Area

Luan J. (Luan Jean) Heywood
Western Washington University, luan.heywood@gmail.com

Recommended Citation

Diversity and Petrogenesis of Rhyolites from an Intra-oceanic Arc: Evidence from IODP Site U1437, Izu Bonin Rear-arc and Surrounding Area

By

Luan Jean Heywood

Accepted in Partial Completion
of the Requirements for the Degree
Master of Science

ADVISORY COMMITTEE

Dr. Susan DeBari, Chair

Dr. Susanne Straub

Dr. Jackie Caplan-Auerbach

Dr. Brian Rusk

GRADUATE SCHOOL

Dr. Gautam Pillay, Dean

Master's Thesis

In presenting this thesis in partial fulfillment of the requirements for a master's degree at Western Washington University, I grant to Western Washington University the non-exclusive royalty-free right to archive, reproduce, distribute, and display the thesis in any and all forms, including electronic format, via any digital library mechanisms maintained by WWU.

I represent and warrant this is my original work, and does not infringe or violate any rights of others. I warrant that I have obtained written permissions from the owner of any third party copyrighted material included in these files.

I acknowledge that I retain ownership rights to the copyright of this work, including but not limited to the right to use all or part of this work in future works, such as articles or books.

Library users are granted permission for individual, research and non-commercial reproduction of this work for educational purposes only. Any further digital posting of this document requires specific permission from the author.

Any copying or publication of this thesis for commercial purposes, or for financial gain, is not allowed without my written permission.

Luan Heywood

August 13th, 2018

Diversity and Petrogenesis of Rhyolites from an Intra-oceanic Arc: Evidence from IODP Site U1437, Izu Bonin Rear-arc and Surrounding Area

A Thesis
Presented to
The Faculty of
Western Washington University

In Partial Fulfillment
Of the Requirements for the Degree
Master of Science

by
Luan Jean Heywood
August 2018

Abstract

Magmas from the Izu Bonin rear-arc show a geochemical signature (medium- to high-K and light rare-earth element [LREE] enriched) that resembles the average composition of the continental crust. I investigate that continent-like signature by examining a suite of rear-arc-derived mafic to felsic tephras from International Ocean Discovery Program (IODP) Site U1437, which was drilled as part of IODP Expedition 350. Volcaniclastic glasses from Site U1437 comprise a compositional series from basalt to rhyolite, aged 1.1-4.4 Ma.

Site U1437 tephras record the timespan when the Izu-Bonin arc began rifting and provide a well-dated record of changing magmatic compositions through the transition into arc rifting. Considered with context provided by a comprehensive recontextualization of published analyses of <7 Ma regional dredged rocks, magmatic compositions are shown to vary in coherent chronological and spatial trends and can be classified into three series: LREE-depleted volcanic front series; flat pattern REE rift-related series; and LREE-enriched rear-arc seamount chain-type (RASC-type) series which includes Site U1437 glasses. Each series has a distinctive characteristic basalt type whose trace element and radiogenic isotope chemistry matches rhyolite type from the same region.

Geochemical modeling shows that fractional crystallization is a viable mechanism to generate <4.4 Ma RASC-type rhyolites, via 70-80% fractional crystallization from a typical rear-arc basalt. Evidence such as lack of trace element correlation above ~73 wt. % SiO_2 and oxygen isotope systematics show that some degree of open-system processes are involved in rhyolite petrogenesis; however there is no evidence for large-scale melting of pre-existing crustal sources. The >12.9 Ma crustal sources inferred to exist within the rear-arc region cannot be the source for rear-arc rhyolites because of differing La/Yb and εHf signatures. Thus, I favor a model where fractional crystallization is the differentiation mechanism involved in the generation of intraoceanic arc rhyolites in this region.

Acknowledgements

Table of Contents

List of Figures

List of Tables

1. Introduction

The primary model for the formation of continental crust during the Phanerozoic is through geochemical output at subduction zones (Rudnick and Gao, 2003). Crustal growth is thought to occur via input from sources beneath the Moho (including melts of the mantle wedge into which slab-sourced fluid and/or melt and/or sediment diapirs have been added), coupled with intracrustal differentiation and probable recycling of dense ultramafic cumulates at the base of the crust (Kay and Kay, 1993; Leat and Larter, 2003; Behn et al., 2011). The focus of this study is on the latter process: intracrustal differentiation. There are two main end member models for how intracrustal differentiation occurs within subduction zones. These are fractional crystallization of mantle-derived basalts (Shaw, 1970) and melting of pre-existing crust (Tamura and Tatsumi, 2002). Some combination of the two is also possible (Annen et al., 2006). The details of these processes, and which of them contributes most strongly to crustal growth, remain unclear. On the one hand, fractional crystallization implies that a crustal column may become more heterogenous in geochemical characteristics through time as primary magmas change, whereas crustal melting implies a homogenization of the geochemical characteristics of the crustal column over time.

This study focuses on magmatic processes that create rhyolitic volcanism in the Izu-Bonin-Mariana subduction zone (IBM) in the Western Pacific (Figure 1), with emphasis on the Izu-Bonin rear-arc region. Throughout most of its history, the IBM has existed as an arc-backarc system, with alternating episodes of arc construction and arc rifting (e.g. Ishizuka et al., 2011). The modern (<7 Ma) arc of the Izu-Bonin has been separated based on geomorphology, eruptive history and geochemical output into a volcanic front, rift, and a rear-arc region (e.g., Stern et al.,

2004). The rear-arc is still within the main arc massif, but is behind the volcanic frontal chain

(Figure 1). Within the Izu-Bonin rear-arc region, lava erupts with a distinct geochemical

signature: medium K, light rare earth element [LREE] enriched, and lower $^{143}Nd/^{144}Nd$,

$^{176}Hf/^{177}Hf$ and $^{206}Pb/^{204}Pb$ relative to volcanic front (Tamura et al., 2015). This geochemical

signature resembles the composition of average continental crust (Rudnick and Gao, 2003) more

closely than the LREE-depleted, low-K tholeiites from the volcanic front (Straub, 2003; Bryant

et al., 2003). Although details of the hypotheses vary, most authors surmise that the origin of this

chemical distinction is due to an across-arc variation in the relative amounts of slab fluid vs. slab

melt that interact with the melting mantle and relative enrichment of the mantle (Hochstaedter et

al., 2000; Hochstaedter et al., 2001; Tamura et al., 2007; Tollstrup et al., 2010; Kimura et al.,

2010).

In this study I present major element, trace element and isotopic data for tephra layers recovered

during IODP Expedition 350 at Site U1437 in the Izu-Bonin rear-arc. The upper-most quarter of

Site U1437 contains tephras that can be provenanced to Izu-Bonin regional origin (as distinct

from Japan arcs), and provide a time-integrated record of <4.4 Ma explosive magmatism within

the Izu-Bonin rear-arc region. With the goal of understanding arc crust, I compare new

geochemical analyses performed on Site U1437 tephra to the published record of dredged lavas

and pumices from a ~250 km long segment of the northern Izu-Bonin.

During the timespan recorded by Site U1437 tephras, the Izu-Bonin arc underwent a transition to

rifting, which is recorded in changing composition of the magmatic output from the rear-arc

region. This has created a lack of interpretive clarity in the literature about which magmas

constitute the rear-arc signature, especially in regards to the diffuse volcanism from the back-arc

knolls region (Hochstaedter et al., 2000; Tollstrup et al., 2010; Haraguchi et al., 2017). With this

goal, I examine spatial and chronological patterns in across-arc variation and find that <7 Ma northern Izu-Bonin dredged lavas can be categorized into three coherent series based on rare-earth element (REE) chemistry, each with distinctive rhyolites: LREE-depleted volcanic front series; flat REE rift-related series; LREE-enriched rear-arc series, which I call rear-arc seamount-type (RASC-type) series. This study for the first time characterizes rhyolite variation inclusive of Izu-Bonin rear-arc rhyolites.

I find that the distinctive continental crust-like medium to high-K, LREE enriched RASC-type signature is present in 1.1-4.4 Ma locally-sourced tephras from basaltic to rhyolitic compositions, while it is lacking in a 12.9 Ma rhyolite sill from the same location. Among <4.4 Ma tephras, glass and mineral chemistry are consistent with rhyolite magmagenesis via extreme (>75%) fractionation of a mafic parent magma. I compare the trace element and isotopic characteristics of 4.4 Ma rhyolites to older (12.9 Ma) rhyolites from the rear-arc region and conclude that they are not cogenetic, and that scenarios requiring melting of older, less LREE-enriched crust are not sufficient to generate more modern RASC-type rhyolites.

2. Regional context for rhyolitic volcanism

The Izu-Bonin-Mariana (IBM) arc is an optimal location for studying intracrustal differentiation processes. It is an intraoceanic arc located in the western Pacific between Guam and Japan, where the Pacific Plate subducts westward underneath the Philippine Sea Plate (figure 1). The IBM is an exemplary and long-lived representation of subduction within the oceanic realm.

Within the IBM, periods of arc-construction are punctuated by arc rifting (Stern et al., 2004; Ishizuka et al., 2011). Subduction initiated around 52 Ma with the widespread eruption of forearc basalts and boninites (Reagan et al., 2010), followed by true subduction-related arc magmatism

around 43 Ma (Stern et al., 2004). This period of arc construction was interrupted ~25 Ma, when arc volcanism ceased and the arc underwent rifting and subsequent spreading to open the Shikoku and Parece Vela basin (figure 1; Ishizuka et al., 2011).

The oldest volcanism within the Izu-Bonin rear-arc manifests as a number of across-arc seamount chains that trend approximately ENE-WSW (figure 1; e.g. Taylor, 1992; Hochstaedter et al., 2000). Origins for these seamount chains are debated, with end-member hypotheses involving a tectonic origin (Bandy and Hilde, 1983; Yamazaki and Yausa, 1998) or localized heterogeneities within the sub-arc mantle (Tamura et al., 2002).

Ishizuka et al., (2003) dated dredge samples from these seamounts by ^{40}Ar-^{39}Ar and found that rear-arc volcanism initiated around 17 Ma, or ~2 Myr prior to the cessation of Shikoku Basin spreading. Until ~3 Ma, volcanism propagated from west to east within the cross-arc seamount chains, dubbed Western Seamounts by Hochstaedter et al. (2000). After 2.8 Ma, the arc began rifting and the primary locus of volcanism in the rear-arc moved eastward into the back-arc knolls region. Since ~1 Ma, volcanism has been confined to the rift depression located just behind the modern Izu-Bonin volcanic front (figure 1; Ishizuka et al., 2003).

Rhyolites are a volumetrically significant eruptive product throughout all regions of the Izu-Bonin arc, with diverse geochemical signatures that vary as a function of age as well as tectonic setting (Hochstaedter et al., 2000; Tamura and Tatsumi, 2002; Machida and Ishii, 2003). Their origin is a topic of contention. The main end-member hypotheses include extreme fractionation of mafic liquids (Hochstaedter et al., 2000; Wade et al., 2005) and widespread melting of pre-existing crust (Tamura and Tatsumi, 2002; Tamura et al., 2009).

Rhyolite petrogenesis within the Izu-Bonin rear-arc has been attributed to both mechanisms by separate workers. Fractional crystallization of a clinopyroxene-rich mineral assemblage was invoked by Hochastedter et al. (2000) to explain differentiation culminating in medium-K rhyolites. Within the adjacent back-arc knolls region, compositionally similar rhyolites were attributed by Tani et al. (2015) and Haraguchi et al., (2017) as melts of LREE-enriched Neogene rear-arc crust.

In the Izu-Bonin volcanic front and adjacent rift, Tamura et al. (2009) showed that rhyolites erupted in spatially distinct locations had different geochemical signatures, which they interpreted as melting of spatially distinct crustal sources: R1, rhyolites from dominantly basaltic islands that are purportedly derived from melting of LREE-depleted Quaternary crustal andesites; R2, flat-pattern rhyolites from rhyolite-rich submarine calderas located slightly behind the main volcanic front, interpreted to be derived from melting of Oligocene-age crustal andesites; and R3, the most LREE-enriched rhyolites from the <1 Ma rift depression and adjacent backarc knolls region which could be derived from fractionation or melting. Straub (2008) demonstrated both corroboratory and contradictory lines of evidence for either end-member differentiation hypothesis for rhyolite petrogenesis in the volcanic front but suggested that differentiation mechanisms remained the same since soon after subduction initiation, c. ~42 Ma. This lack of consensus genetic model is reflected in many arcs (Leat and Larter, 2003).

Both the Izu-Bonin volcanic front and rear-arc regions of volcanism overlay a thick midcrustal low-velocity layer (figure 1; Suyehiro et al., 1996; Kodaira et al. 2008), hypothesized to be representative of the unsubductable core that forms the nucleus of continental crust (Taira et al., 1999). The midcrust has an interpreted intermediate to felsic composition (Suyehiro et al., 1996), and must be an integral location for the creation and/or storage of felsic magmas. Studying

regional felsic magmatism lends insight into the compositions and processes that create the thick felsic midcrust, which in turn lends insight to the origins of the continental crust at large. Regardless of petrogenesis mechanism, felsic magmas are ultimately closely related to mafic systems. Thus, in order to understand felsic magma generation in a comprehensive way, methodologies must include analysis of their geochemical relationship to contemporaneous mafic magmas.

3. Site U1437 core material

Site U1437 was drilled during IODP Expedition 350 (Tamura et al., 2015; Busby et al. 2017). Many drilling cruises have focused on the Izu-Bonin forearc and volcanic front (e.g. Fryer et al., 1992; Taylor et al., 1992), but Site U1437 represents the first drilling within the rear-arc region (figure 1). In three consecutive cored holes, the JOIDES Resolution ultimately drilled down to 1806.4 meters below seafloor (mbsf), through at least 15 Myr of volcaniclastic stratigraphy, with tephra and other volcano-derived materials alternating with thick (average 40-50 cm) successions of tuffaceous mud (figure 2; Gill et al., 2018; Schmitt et al., 2018). The core was subdivided into seven lithostratigraphic units, based on proportion of mud and volcaniclastic material. This study focuses on samples from the top 730 m of the core, or 1.1-4.4 Ma (figure 2), with additional analyses performed on three samples from deeper within the core to provide additional context.

Unit I consists of the top 682.12 meters of the Site U1437 core. The lithology transitions from unlithified sediment higher in the core into consolidated rocks below ~427 mbsf. In Unit I, tuffacous mud/mudstone is intercalated with discrete layers of ash/tuff to lapilli-ash/lapilli-tuff. Typical samples included in this study were composed of 40-60 modal % volcanic ash and lapilli, 20-40 modal % phenocrysts and up to 15% lithic fragments, not accounting for other

biogenic and non-volcanic lithogenic mud components. Phenocryst minerals present varied from interval to interval. Unit I was dated as 0-~4.3 Ma using the shipboard age model developed with a combination of magnetostratigraphic and biostratigraphic techniques (Tamura et al., 2015).

Unit II (682.12-726.50 mbsf) consists of 44.38 m of fully lithified tuff intercalated with lapillituff/lapillistones with minor tuffaceous mudstone. A typical sample is composed of 85-95 modal % rhyolitic volcanic glass and 5-15 modal % phenocrysts, dominantly plagioclase and clinopyroxene with subordinate orthopyroxene, hornblende and oxides. The top of Unit II is defined by the first lapilli tuff of a sequence dominated by coarse (lapilli-size) volcaniclastics and ends at the first tuffaceous mudstone at the end of the contiguous volcaniclastic sequence. Unit II is dominantly rhyolitic in composition and is dated to ~4.3-4.4 Ma (Tamura et al., 2015). The unit is interpreted to be locally (rear-arc) derived based on its coarse-grained characteristics, moderate K_2O, and higher Zr/Y ratio than volcanic front magmas (Tamura et al., 2015).

Igneous Unit 1 is located much deeper within the core (1388.86-1390.07 mbsf) and consists of a thin (<6.5 m) rhyolitic sill emplaced within the volcaniclastic lithostratigraphic Unit VI. Rhyolite groundmass varies from cryptocrystalline to fine-grained. Phenocrysts compose 10-15 modal % and include plagioclase, hornblende, quartz, Fe-Ti oxides and rare zircons. A zircon from Igneous Unit 1 has a U-Pb age of 12.9 +/- 0.3 Ma (Schmitt et al., 2018). The upper and lower boundaries of the sill show peperitic margins which suggest that the sill intruded into unconsolidated wet sediment.

4. Methods

Tephra sampling for this study originally focused on Unit II, with the goal of identifying intervals with abundant unaltered glass with a variety of compositions. Preliminary chemical

analyses indicated that Unit II was surprisingly uniform in composition, and that intervals originally designated mafic were in fact composed of dark-colored rhyolitic glass rich in microphenocryst inclusions. In order to find a more diverse range of related compositions, sampling was expanded into Unit I intervals, aged 1 Ma and older. Preliminary scanning electron microscope back-scattered electron (SEM-BSE) and electron microprobe (EMP) analyses were performed on unaltered glass from volcaniclastic-rich intervals to identify tephra layers that contained locally-derived, medium- to high-K glass; these were selected for further analyses.

Tephras were prepared as grain mounts for Unit I samples, and thin-sections for Unit II samples. Geochemical compositions of glass shards and minerals from Site U1437 were determined using a combination of electron microprobe (EMP) for major and minor elements, laser ablation inductively coupled plasma mass spectrometer (LA-ICP-MS) for trace elements, and multi-collector inductively coupled plasma mass spectrometer (MC-ICP-MS) for isotopes in whole rock samples. New whole-rock major and trace element analyses were also obtained for a selection of 5 felsic lava samples collected during 1990s era dredging of nearby rear-arc seamounts on the *R/V Moana Wave* (c.f. Hochstaedter et al., 2000; Haraguchi et al., 2017) by X-ray fluorescence (XRF) and ICP-MS. These results are presented in Table 1.

4.1 Electron microprobe

Major element concentrations of glass shards and minerals (hornblende, pyroxenes, plagioclase, oxides) were obtained via electron microprobe (EMP) on three instruments: the Jeol 733 Superprobe at the University of Washington, Jeol JXA-8230 Superprobe at the University of Iowa and Jeol JXA-8200 at GEOMAR. All analyses used 15 kV acceleration voltage. Beam conditions were 15 nA current and <1 μm diameter for minerals and 15 nA current defocused to 5 μm diameter for glass, with counting times of 20-40 seconds for most major and minor

elements and 10-20 seconds for backgrounds. Calibration standards included an array of natural and synthetic glasses and minerals. Analytical error is <3.5% for major elements, <6% for most minor elements and higher for minor elements present in <0.2 wt. % oxide (see Appendix A). Repeat analyses of several glass shards were performed to compare inter-laboratory variation; these repeats were within error of one another. All glass analyses were normalized to 100% to account for post-depositional hydration and analyses with <88% total oxides or that were affected by microlites were discarded.

4.2 LA-ICP-MS

Trace element concentrations of glass shards were obtained via LA-ICP-MS at Western Washington University using a 213 nm Nd:YAG New Wave UP-213AS laser ablation system coupled to an Agilent 7500ce quadrupole ICP-MS, and at Oregon State University using a Photon Machines Analyte G2 laser ablation system coupled to a Thermo X-Series II quadrupole ICP-MS. Spot size was set between 50-80 μm with a 17.0-17.5 J/cm^2 energy density and 10 Hz repetition rate. Standard glasses were measured before and after each sample, or about 10-20 ablations. NIST610 and GSE-1G glass was used as the calibration standard using compositions from Jochum et al., 2011 at WWU and OSU respectively. Analyses were performed on the same spot as EMP, and silica concentration measured by EMP was used as an internal standard to normalize element ratios. BVHO-2 was used as an external standard to monitor accuracy, with results listed in Appendix A. Elements analyzed are listed with WWU average minimum detection limits in parentheses: ^{23}Na (3.53 ppm), ^{26}Mg (0.594 ppm), ^{27}Al (0.239 ppm), ^{29}Si (168 ppm), ^{31}P (10.6 ppm), ^{34}S (116 ppm), ^{39}K (3.41 ppm), ^{42}Ca (123 ppm), ^{45}Sc (0.131 ppm), ^{49}Ti (0.429 ppm), ^{51}V (0.0426 ppm), ^{56}Fe (0.706 ppm), ^{60}Ni (0.561 ppm), ^{85}Rb (0.0688 ppm), ^{88}Sr (0.0116 ppm), ^{89}Y (0.00870 ppm), ^{90}Zr (0.0183 ppm), ^{93}Nb (0.0133 ppm), ^{133}Cs (0.0176 ppm),

^{137}Ba (0.0700 ppm), ^{139}La (0.00829 ppm), ^{140}Ce (0.00872 ppm), ^{141}Pr (0.00723 ppm), ^{146}Nd (0.0448 ppm), ^{147}Sm (0.0553 ppm), ^{153}Eu (0.0133 ppm), ^{157}Gd (0.0561 ppm), ^{159}Tb (0.00849 ppm), ^{163}Dy (0.0354 ppm), ^{165}Ho (0.00937 ppm), ^{166}Er (0.0254 ppm), ^{169}Tm (0.00896 ppm), ^{172}Yb (0.0417 ppm), ^{175}Lu (0.00985 ppm), ^{178}Hf (0.0374 ppm), ^{181}Ta (0.0120 ppm), ^{208}Pb (0.0313 ppm), ^{232}Th (0.0170 ppm), ^{238}U (0.0184).

Samples analyzed at WWU were normalized for instrumental bias for some trace elements using normalization factors listed in Appendix A. Where sample allowed, repeat analysis on the same grain was performed to verify precision between different laboratories.

4.3 MC-ICP-MS

Nd, Hf, Pb, and Sr isotopic concentrations of 3 representative Unit II tephra intervals were obtained via multi-collector inductively-coupled plasma mass-spectrometer (MC-ICP-MS) at Melbourne University. Lead, Sr, Nd, and Hf aliquots for isotopic analysis were separated from a single sample from about 100-200 milligrams of powder. Sample powders were leached for 30 minutes with hot 6N HCl and then digested in a 2:1 HF + HNO3 solution prior to standard ion exchange procedures. Lead was extracted using conventional anion exchange methods and HBr-HCl media. Strontium and LREEs were extracted on EICHROM Sr-resin and RE-resin, respectively, followed by Nd purification on EICHROM LN-resin (Pin et al., 1994; Pin and Santos-Zalduegui, 1997). Hafnium is separated by the single-column method described by Münker et al. (2001).

The data were obtained using a Nu Instruments multi-collector ICP-MS that is coupled to a CETAC Aridus desolvating nebulizer operating at a sample uptake rate of ~30 μL/min for sample introduction. The instrumental mass bias is corrected by normalizing to ^{146}Nd/^{145}Nd =

2.0719425 (equivalent to ^{146}Nd/^{144}Nd = 0.7219), ^{86}Sr/^{88}Sr = 0.1194, and ^{179}Hf/^{177}Hf = 0.7325 using an exponential law. International standards measured concurrently with the samples gave the following results: ^{86}Sr/^{88}Sr for BCR2 =0.705012+18 (n=1); ^{143}Nd/^{144}Nd for JND-1 =0.512104+9 (n=1), BCR2 =0.512632+8(n=1), BHVO2 =0.512995+6 (n=1); ^{176}Hf/^{177}Hf for BCR2 =0.282868+7 (n=1), BHVO2 =0.283104+5 (n=1). ^{206}Pb/^{204}Pb, ^{207}Pb/^{204}Pb and ^{208}Pb/^{204}Pb for NIST SRM981 (n=6) gave ratios of 16.935+0.002, 15.489+0.002 for and 36.704+0.007, respectively. Further details can be found in Woodhead et al. (2001) and Maas et al. (2005).

4.4 Whole rock XRF/ICP-MS

Whole-rock major and trace element analyses were obtained for 5 dredged lavas at the Washington State University GeoAnalytical Laboratory, following the methods of Knaack et al., (1994). Altered rinds of dredged rocks were removed using a rock hammer, then fresh rock chips were powdered using tungsten carbide shatterbox for XRF beads and alumina shatterbox for ICP-MS beads. Rock powders were then oven-dried for 24 hours at 100 °C. Rock powders for XRF analysis were mixed in a 2:1 ratio of dry lithium tetraborate to rock powder, and rock powders for ICP-MS analysis were mixed with 1:1 ratio of dry lithium tetraborate. Beads were fused in a 1000 ºC pre-heated muffle oven for 20 minutes, following the methods of Johnson et al. (1999). At WSU, major element analyses were performed using a Thermo-ARL x-ray fluorescence (XRF) spectrometer. Trace element analyses were performed using an Agilent 7700 ICP-MS.

5. Results

5.1 Glass chemistry

Glass analyses come from 12 intervals in Unit I and 13 intervals in Unit II (see Fig 3b, Table 1). Intervals range in age and depth from 1.1-4.4 Ma and 132.8-715.0 mbsf. Within each interval, glass shards analyzed were chosen to depict representative populations of SiO_2, and when possible, favored glass shards larger than 50 μm diameter, in order to have sufficient spot size for LA-ICP-MS analyses. Glass shards analyzed in Unit I range from angular and vesicle-free to bubble wall shards and pumice fragments (see figure 2). Glass analyzed in Unit II ranges from small (<1 mm) pumice fragments to large (< 7 mm) vesicle-free sub-angular glass lapilli. Many intervals contained lithic fragments, identifiable via microlitic plagioclase and diagenetic pyrite. These fragments were not analyzed

Glass analyses performed in this study range from 49.3 to ~80 wt. % SiO_2 on a 100% normalized basis. As typical with sampling from the volcaniclastic record of explosive volcanism, felsic magmatism is strongly represented (Figure 3a), and almost all studied intervals contain rhyolite glass (Figure 3b). Some intervals are compositionally homogenous (SiO_2 wt. % ranges <8% relative to each other), while others are mixed in composition from basalt to rhyolite (Table 1, Figure 3). Mixed layers either a) display linear trends on Harker diagrams or b) are strongly bimodal in composition (figure 4).

On Figure 4, all intervals are plotted on major element variation diagrams, with Unit I intervals in solid symbols and Unit II intervals in open symbols. Glass compositions show remarkably coherent trends overall, with TiO_2, FeO_T, CaO, MgO behaving compatibly (decrease with increasing SiO_2), and K_2O, Na_2O behaving incompatibly (increase with increasing SiO_2).

12

Aluminum (Al_2O_3) increases until an inflection at ~68 wt. % SiO_2 where it decreases, similar to the behavior of P_2O_5.

Although most geochemical trends with SiO_2 are coherent, many rhyolitic intervals show a continuous range of K_2O of up to 1-2 relative wt. % for a given interval of otherwise restricted compositional range, even within the same 1 cm interval of rhyolite lapilli. This variation of K_2O wt. % trends negatively with SiO_2 wt. % and positively with Na_2O wt. % and electron microprobe total sum of oxides. I attribute the range to variable alteration that mobilizes sodium and potassium within glass, and for this reason, when rhyolitic glass from otherwise compositionally homogenous intervals showed a range of potassium, those with lowest totals/potassium are not shown.

In comparison to published literature trends for dredged lavas from the rear-arc, glass trends show slight offsets in Fe, Ti, and Na. In the glass dataset, Fe and Ti are elevated and Na is lower than the values at corresponding whole rock SiO_2. Similar-trending offsets in these elements are also noted in comparing whole rock and glass datasets in the IBM volcanic front (Bryant et al., 1999; Tamura et al., 2009; Tollstrup et al., 2010). I attribute these offsets to concentration of microlitic Fe-Ti oxide inclusions in glass, and diffusive migration of sodium during electron beam analysis respectively.

A small number of predominantly medium-K rhyolitic intervals also contain modally small, uniform and distinct populations of low-K rhyolitic glass. Low-K rhyolite ashfall tephras originating in the Izu-Bonin volcanic front have also been sampled from this site (Schindlbeck et al, 2018). Some back-mixing between tuff layers and between and mud and tuff layers has

occurred post deposition due to bioturbation (Tamura et al., 2015). These low-K rhyolite glasses are omitted from this study and not shown on figures.

On Figure 5, trace element variation diagrams also show coherent trends. Most of the elements plotted in Figure 5 behave incompatibly, with the exception of Sr. Rare-earth elements (REEs) and large-ion lithophile elements (LILEs) correlate positively until ~73 wt. % SiO_2, except Sr which remains constant until ~73 wt. % SiO_2 and subsequently decreases. Rhyolitic glass with SiO_2 greater than 73 wt. % has decreasing incompatible element (IE) concentrations (e.g., see Zr vs SiO_2 on figure 5). Similar trends are also noted in whole rock analyses from dredged samples proximal to the drill site. A more detailed comparison of glass trends to regional whole rock datasets is included in the discussion (see below).

5.2 Isotope data

Three glass-rich lapillituff intervals from Unit II were selected for Sr-Nd-Hf-Pb isotope analysis. All three samples fall within the Izu-Bonin RASC-type field for Pb, Nd, Hf isotopes as defined by Hochstedter et al., (2000b) (figure 6). They show less radiogenic signatures for Nd and Hf isotopes, and lower $^{208}Pb/^{204}Pb$ isotopes relative to lavas from the Izu Bonin volcanic front. Two of the three fall within the RASC-type field for Sr, but one, U1437D-31R-4 79/81, shows anomalously high Sr isotope ratio ($^{87}Sr/^{86}Sr$ = 0.704566±17; table 5; not plotted on Figure 6). This Sr isotope analysis is well above any reported Sr isotope analysis from the Izu-Bonin arc, and shows Sr isotopes closer to the marine sediment field (White, 2015). Pb isotopes fall within the RASC-type array, which together other Izu-Bonin samples form a linear array above the Northern Hemisphere Reference Line (Hart, 1984; Hochstaedter et al., 2001).

5.3 Mineral chemistry and textures

5.3.1 Plagioclase

Plagioclase is the dominant phenocryst phase and is present in all but the two most crystal-poor of the intervals studied (figure 7-8; table 2). In most Unit I intervals, it is present as isolated phenocrysts amidst glass shards, whereas in Unit II it is found both as isolated phenocrysts and embedded within rhyolite lapilli. Within Unit I intervals, plagioclase is commonly angular anhedral, with occasional sieve textures (Figure 7). Unit II commonly contain subhedral to euhedral plagioclase without visible disequilibrium textures. There was no observed relation between plagioclase texture and coexisting glass SiO_2 concentration.

Plagioclase ranges from An 27-89, with core An content of plagioclase commonly correlating with associated glass chemistry (figure 8). For example, bimodal plagioclase populations are found in intervals of bimodal glass composition, primarily albitic plagioclase in intervals with felsic glass composition.

5.3.2 Pyroxenes

Crystals are typically angular subhedral, with no visible disequilibrium textures (figure 7). Phenocrysts are commonly broken, so measurements were taken as close to the estimated core as possible.

Clinopyroxenes are mostly augites with Mg# = 48-77. Minor elements include TiO_2 (<0.7 wt. %), Al_2O_3 (<3.0 wt. %), MnO (<1.2 wt. %) and Na_2O (<0.5 wt. %) (table 3).

Orthopyroxenes are mostly bronzite-hypersthenes with a continuous range from Mg# = 49-74. Minor elements include TiO_2 (<0.3 wt. %), Al_2O_3 (<1.3 wt. %), MnO (<2 wt. %), and CaO (<2.0

wt. %) (table 3). Orthopyroxenes generally have lower Mg# than coexisting clinopyroxenes, with K_d(Fe-Mg) = 0.59-0.90 for cpx/opx, typically around 0.80.

Pyroxene populations generally correlate with glass compositions (see figure 8), with the exception that rhyolite-only Unit II contains two populations of pyroxenes: felsic coexisting cpx/opx and a significant population of mafic coexisting cpx/opx.

5.3.3 Amphibole

Amphibole has been documented as a phenocryst in some intermediate to felsic rear-arc magmas (Hochstaedter et al., 2000; Machida and Ishii, 2003; Machida et al., 2008; Straub, 2008), but not in magmas from the volcanic front. In this study, amphibole was observed in Unit II intervals and the Unit I rhyolite interval immediately overlying Unit II (~4.3 Ma).

Amphiboles are magnesiohornblende, with Mg# 61-64 (figure 8). Crystals are subhedral to euhedral. Aluminum ranges from 8-9 wt. % oxide (see table 4).

5.3.4 Fe-Ti oxides

Fe-Ti oxides occur as individual microphenocryts (10-50 μm diameter) within or among glass as well as in crystal clots with plagioclase and apatite (figure 7). They are classified as ulvospinel and ilmenite pairs. Among ulvospinels, TiO_2 contents range from 6.9-16.6 wt. %, equivalent to 35-55% ilmenite. Ilmenites have TiO_2 contents from 42.5-57.5 wt. %, equivalent to 98-100% ilmenite. Minor elements include Al_2O_3 (up to 3 wt. % oxide), V_2O_3 (up to 2.5 wt. % oxide), MgO (up to 4 wt. % oxide), MnO (up to 1.5 wt. % oxide), and minor Cr and Zn (<0.3 wt. %) (Appendix B Table 1).

5.3.5 Other mineral phases

Some rhyolitic intervals within Unit I have quartz. Other mineral phases are present as minor phases in some rhyolitic intervals, including apatite and titanite. One Unit II interval contained trace olivine. These phases are present as <1% of the mode within any interval and were not analyzed. Most intervals studied also contain diagenetic pyrite framboids.

5.4 Intensive parameters of crystallization

One of the main goals of this study is to investigate intracrustal magmatic processes, for which an important component is constraining the conditions and locations where magmas undergo processing and storage, as well as magmatic fO_2 and H_2O. I interpret these processes as recorded in erupted phenocrysts using various mineral-based themobarometric techniques.

Temperatures of crystallization were obtained using two methods: paired Fe-Ti oxide thermometry (Lepage, 2003) and 2-pyroxene thermometry (Putirka, 2008) (Appendix B).

For paired Fe-Ti oxide thermometry, intervals with unimodal or strongly bimodal glass compositions that contained both unexsolved ulvospinel and ilmenite were targeted for EMP analyses on Fe-Ti oxides. Electron microprobe analyses of ilmenite and ulvospinel were corrected for Fe and Ti peak interference after Evans et al. (2006). Choosing coexisting pairs of minerals is hampered by the fact that many intervals contain a range in magmatic compositions, and potentially multiple phenocryst populations. The Bacon & Hirschmann test for equilibrium (Bacon and Hirschmann, 1988) was used to identify coexisting pairs of Fe-Ti oxides within individual intervals. Temperatures of crystallization were estimated using ILMAT (Lepage, 2003). Fe-Ti oxide temperatures range from 930 °C in a largely basaltic andesitic interval

(U1437-20F-2 101-102) to 853 °C in a rhyolitic interval (U1437-35x-2 6-7). Unit II rhyolites have paired iron-oxide temperatures of 840-891 °C (see Appendix B Table 1).

2-pyroxene temperatures were obtained by pairing clinopyroxenes and orthopyroxenes from the same interval, using the methods of Putirka (2008). When multiple populations of pyroxenes were present, clinopyroxene/orthopyroxene populations were matched by relative Mg#, i.e. most primitive clinopyroxene with most primitive orthopyroxene. Two-pyroxene temperatures range from 957 °C in a largely basaltic andesitic interval (U1437-21F-1 93/94) to 879 degrees C in a Unit II rhyolitic interval (30r-5w 129/132) (see Appendix B Table 2).

When 2-pyx thermometry and paired Fe-Ti oxide thermometry were performed on the same interval, 2-pyx temperatures were 30-50 °C higher than Fe-Ti oxide temperatures, which is related to less efficient equilibration for pyroxene. This relationship was also observed by Straub (2008) in the Izu-Bonin volcanic front.

Temperature-dependent hornblende barometers (Anderson and Smith, 1995) gave unreasonable pressures, likely due to mismatch with overly albitic plagioclase (Appendix B Table 3). Temperature-independent hornblende barometers gave relatively low pressures of 1.42-1.73 +/- 0.20 kbar (Ridolfi and Renzulli, 2012). These latter pressures equate to amphibole crystallization depths of ~6 km.

Magmatic oxygen fugacity was determined using paired-iron oxides (LePage, 2003) (Appendix B Table 1). Paired-iron oxide data were reduced as noted above. Fugacity was consistent with the NNO to NNO+1 buffer conditions.

Water content was determined using the plagioclase-liquid hygrometer/thermometer (Lange et al., 2009) (Appendix B Table 4). In each given interval, the most mafic glass was paired with the most anorthic plagioclase analysis and applied through the Plag_Hygrometer program of Lange et al. (2009). Water contents ranged from ~4 wt. % H2O in basaltic glass/anorthite pairs increasing to ~5.5 wt. % H_2O in rhyolitic glass/albite pairs (see Appendix B Table 4).

Overall, due to tephras and phenocrysts sampled, intensive parameters of magma crystallization can only be reliably interpreted to constrain magmatic conditions for felsic magmas. Thermobarometry is suggestive of hydrous felsic magma storage in a cool, shallow midcrustal magma chamber around 6 km depth, with eruptive temperatures around 850 ºC.

6. Discussion

6.0 Comparison of Site U1437 tephras to regional magmas

To contextualize the origin of Site U1437 magmatic glasses, I compare their chemistry with that of regional magmas. The purpose of this comparison is twofold: 1) to determine the provenance of tephra layers – are they indeed locally derived and representative of magmatism in the Izu-Bonin rear-arc region?; and 2) to contrast their compositions with the compositions of magmas in the larger arc-wide regional context, in order to draw conclusions about their petrogenesis.

Site U1437 is located within a volcano-bounded basin (Tamura et al., 2014) in the Izu-Bonin rear-arc region, in between the Manji and Enpo Seamount chains and adjacent backarc knolls region. These regions were volcanically active during the timespan recorded in the Site U1437 core (Ishizuka et al., 2003), but are not the only regional volcanic source. Tephras from numerous distal sources have been documented at Site U1437 (Schindlbeck et al., 2018)

including tephras from other sources within the Izu-Bonin (volcanic front and rift) and minor distal ashfall from Japanese arc volcanism located within a 400-800 km radius from the drill site.

Unit II tephras are coarse-grained, with Izu-Bonin RASC-type isotopes and likely represent a relatively proximal eruption from a nearby seamount in the Manji Seamount chain, likely Manji or Meireki which are both <20 km away. However the finer-grained Unit I tephras are from unknown, possibly distal locations. In order to determine source, Unit I tephras were compared to published tephra and dredged rock literature from Japanese arcs and the Izu-Bonin arc.

6.1 Comparison of Site U1437 tephras to Japanese tephras

During the timespan recorded in the Site U1437 core, Japanese arcs had voluminous volcanic output resulting in widespread regional ash deposition (Kimura et al., 2015) which are a possible source of distal tephras at Site U1437. Tephras from Japanese arcs (Kyushu, SW Japan arc, NE Japan arc) have been documented at Site U1437 in the <1.1 Ma section of core (Schindlbeck et al., 2018) and are likely to exist deeper within the core as well.

Especially among rhyolites, Japanese tephras have some overlapping major and trace element characteristics with RASC-type tephras, e.g. medium-K, LREE-enriched (figure 9), but key differences rule out Japanese sources for the intervals considered in this study. Following the methods of Schindlbeck et al. (2018), Unit I tephra intervals from this study were compared to a catalog of 80 widespread tephra layers of well-constrained age <5 Ma from Japanese subduction zone volcanoes compiled by Kimura et al. (2015). Japanese tephras and IBM tephras have overlapping ranges of trace element concentrations and ratios (e.g. Th and Ba/La) but these do not covary in the same way and can be used to discriminate between Japanese and IBM tephras

(figure 9). Japanese tephras have higher Th and/or Ba/La than all Site U1437 tephras included in this study.

An additional way to rule out Japanese sources is via isotope geochemistry: Pb, Hf, Nd and Sr isotopes have regionally distinctive isotopic signatures between Japanese arcs and the Izu-Bonin arc (Hanyu et al., 2006). Unit II rhyolites plot within the Izu-Bonin RASC-type field (figure 6; Japanese isotopes not shown) but Unit I intervals in this study were not analyzed for isotope ratios.

6.2 Comparison of Site U1437 tephras to Izu-Bonin dredged rocks

Magmas from within the Izu-Bonin arc have well-documented differences in major, trace and isotopic composition that vary in space and time, but also in geomorphological characteristics of the eruption edifice (c.f. Hochstedter et al., 2000; Tollstrup et al., 2009; Ishizuka et al., 2003). I compared samples from this study to a literature database of ~1200 samples retrieved through dredge and ROV sampling from the Izu-Bonin arc segment from Torishima to Aogashima and west to 138.9° longitude (see figure 10; data from Fiske, 2001; Gill et al., 1994; Haraguchi et al., 2017; Hochstaedter et al., 1990a; Hochstaedter et al., 1990b; Hochstaedter et al., 2000; Hochstaedter et al., 2001; Ikeda and Yasua, 1989; Ishizuka et al., 2002; Ishizuka et al., 2003; Ishizuka et al., 2007; Jordan et al., 2011; Machida et al., 2008; Ossaka et al., 1990; Shukuno et al., 2006; Tamura et al., 2007; Tamura et al., 2009 and references therein; Tani et al., 2008; Yuasa, 1995; additional data retrieved from Data and Sample Research System for Whole Cruise Information in JAMSTEC (DARWIN), 2014).

I characterize this data into three categories: volcanic front volcanism, rift-related volcanism, and RASC-type volcanism (figure 10). Geochemical data were first separated using the eruption

location/geomorphic classifications of Hochstaedter et al. (2000), then further revised using La/Yb, which results in categories that are broadly correlative to geomorphic region (see Figure 10-11). Each newly defined across-arc category shows a coherent and unique geochemical trend from basalts to rhyolites (figure 11), although dredge datasets have poor representation of intermediate magmas, which makes determining precise relationships challenging.

A key outcome of this re-categorization is to deconvolve the different types of magmas that erupt from the back-arc knolls region, which is the descriptive term for the geomorphic province of diffuse submarine volcanic knolls located anywhere between the modern rift depression and the across-arc seamount chain region (Hochstaedter et al., 2000). Rocks dredged from throughout the knolls region encompass a large range of time and chemistry (Hochstedter et al., 2000; Ishizuka et al., 2003; Tollstrup et al., 2010; Haraguchi et al., 2017; La/Yb from 0.77-6.55); however, the vast majority of dredged lavas from the back-arc knolls region show what I term a "RASC-type signature" showing similarities to dredged rocks from the across-arc seamount chains. Dredged rocks from the eastern portion of the back-arc knolls geomorphic province showing rift-related chemistry have been grouped with rocks dredged from the rift itself, and henceforth back-arc knolls only refers to rocks that have these two characteristics: 1.) inferred or observed origin in the back-arc knolls geomorphic province, and 2.) RASC-type geochemistry.

Another key outcome, as discussed below, is the re-categorization grouping R2 rhyolites with rift-related magmatism based on chemistry, rather than with Oligocene-aged crustal components as suggested by Tamura et al. (2009).

6.2.1 Volcanic-front volcanism

This group is representative of volcanism from the large, subaerial edifices in the Izu-Bonin volcanic front and comprises Quaternary lavas sampled from Aogashima, Sumisu and Torishima volcanoes, inclusive of the LREE-depleted rhyolites dubbed R1 by Tamura et al. (2009).

Volcanic front volcanism is dominantly basaltic with minor rhyolites (Tamura and Tatsumi, 2002) and forms a low-K series with characteristic LREE depletion (La/Yb 0.4-1.2, see figure 11-12). Rare-earth elements increase with increasing silica and normalized REE trends stay roughly sub-parallel, with the development of an Eu anomaly starting around 57 wt. % SiO_2 (figure 12). La/Sm increases slightly from average 0.85 in basalts to 1.12 in rhyolites, while Dy/Yb decreases slightly from average 1.54 in basalts to 1.50 in rhyolites (figure 11). Zr/Y increases steadily from average 1.66 in basalts to average 2.41 among rhyolites.

Volcanic front basalts through rhyolites have little variation in Pb and Nd isotopes ($^{143}Nd/^{144}Nd$ = 0.51306-0.51312), but rhyolites on average have higher $^{87}Sr/^{86}Sr$ than basalts (rhyolite average $^{87}Sr/^{86}Sr$ = 0.70371, basalt average $^{87}Sr/^{86}Sr$ = 0.70350, figure 13). Elevated $^{87}Sr/^{86}Sr$ in modern volcanic front rhyolites cannot be explained by assimilation or melting of Eocene-Oligocene sources, as Eocene-Oligocene tephras show similar $^{87}Sr/^{86}Sr$ but lower $^{143}Nd/^{144}Nd$ than volcanic front rhyolites (Straub et al., 2010, see figure 6).

6.2.2 Rift-related volcanism (sensu lato)

This group comprises the dominantly basaltic volcanism from the <1 Ma rift/intra-arc depression, grouped together with rhyolites from the submarine rhyolitic calderas, referred to by Tamura et al., (2009) as R2 volcanism, and a portion of the rift-adjacent knolls region, referred to Hochstaedter et al. (2000) as Backarc Knolls (figure 10). This category is inclusive of rift

rhyolites that Tamura et al. (2009) had previously included in the generalized category of behind-arc rhyolites referred to as R3 type rhyolites from the rift and back-arc knolls region.

Grouping R2 rhyolites and rift magmatism follows the precedence of Haraguchi et al. (2017), who studied dredged lavas from the intra-arc rift region—excluding the submarine rhyolitic calderas—and found that R2-signature rhyolitic volcanism is not limited to these centers but is regionally pervasive through the rift and eastern portion of the back-arc knolls (figure 10). Rift-signature basaltic magmatism is observed as far west as 139.4°, or 38 km from the volcanic front (most <26 km from the volcanic front)), and I group these basalts together on the basis of their geochemical similarities (figure 11). This represents a departure from previous groupings, which linked R2 rhyolites from the submarine rhyolitic volcanic centers with volcanic front volcanism, on the basis of geomorphology and distance to volcanic front.

Considered together, rift-related rocks form a low-K series with flat rare-earth patterns (La/Yb 1.3-2.2; figure 11-12). Rift-related rocks can be differentiated from the rear-arc (inclusive of adjacent backarc knolls) because they show a smaller degree of LREE-enrichment (La/Yb <2.2, most basalt La/Nd under ~0.47) and are also younger than 1 Ma. In rift-related rocks, rare-earth element abundances increase with increasing silica and increase in degree of MREE depletion (figure 12). La/Sm increases from an average 1.3 in basalts to 1.7 in dacites and rhyolites, while Dy/Yb decreases from average 1.8 in basalts to 1.5 in dacites and rhyolites. Zr/Y increases steadily from an average of 2.9 in basalts to 4.2 in dacites and rhyolites (figure 11). Considered together, the mafic/felsic trends show the same covariation as in other regions of the Izu-Bonin (e.g. enrichment in incompatible elements, increasing Zr/Y, progressive MREE depletion), but with distinct mafic end-members (figure 11).

Rift-reflated basalts and rhyolites have similar but not identical isotopic compositions (figure 13). Rift-related Pb isotopes form an array that is parallel to the NHRL, with basalt and rhyolite fields overlapping (figure 6). Rift basalt and rhyolites have identical Nd isotopes ($^{143}Nd/^{144}Nd =$ 0.51303-0.51312). R2 rhyolites have higher $^{87}Sr/^{86}Sr$ than rift basalts, similar to that of Eocene-Oligocene crust (Tamura et al., 2009), but the one $^{87}Sr/^{86}Sr$ analysis from a rift rhyolite outside the volcanic front-adjacent R2 center (Tamura et al., 2009) overlaps rift basalts (figure 13). Hf isotope signature for rift basalts and Eocene-Oligocene crust are distinct (figure 6); however, it is unclear how this extends to rift rhyolites: there are few published Hf isotopic analyses for rift rhyolites and none from R2 rhyolitic calderas.

Tamura et al., (2009) suggested that the geochemical similarity of R2 rhyolites to Oligocene tephras is evidence that R2 rhyolites originate as crustal melts of Oligocene-age midcrust (figure 14). The resemblance of R2 rhyolites to certain Oligocene lavas is undeniable, shown by comparing R2 rhyolites to the Oligocene Komahashi Daini Seamount (Haraguchi et al., 2003); however, R2 rhyolites also share an undeniable resemblance to rift basalts which erupt in the same time and place. R2 rhyolites could indeed be derived from an Oligocene crustal component, but rift basalts could not. Thus, R2 rhyolites may just as easily share a genetic relationship with rift basalts as Eocene-Oligocene crust.

6.2.3 Rear-arc seamount chain-type (RASC-type) volcanism (<7 Ma)

This group comprises two subgroups of volcanism, classically categorized as dredge rocks from the cross-chain seamounts, dubbed Western Seamounts, and most of the smaller volcanic cones and ridges to the east of the seamount chains as back-arc knolls. Western Seamount volcanism initiated around 17 Ma at seamounts now located around 138º 30' E and progressed eastward to form ENE trending seamount chains, observed today with volcano-bounded basins interspersed

between them. Focused seamount-chain magmatism gradually transitioned to diffuse back-arc knolls style volcanism on the east side of the rear-arc region, which was the primary locus of volcanism after ~2.8 Ma. In the timespan/area depicted in this study, both Western Seamounts and back-arc knolls magmatism occurred concurrently with overlapping chemistry and longitude, but distinct geomorphic expression (Ishizuka et al., 1998; Hochstaedter, 2000; Ishizuka et al., 2003; Tani et al., 2015). This study does not consider Western Seamounts dredges older than 7 Ma, since the paucity of dated rhyolitic dredges before 7 Ma (Ishizuka et al., 2003) make interpreting mafic-felsic relationships difficult. As defined in this study, I characterize Western Seamounts and back-arc knolls volcanism within the overarching geochemical category of 'RASC-type volcanism' but at times discuss them separately.

There is some ambiguity within the literature about what comprises the back-arc knolls signature. Previously published classifications show dredged rocks from seamounts in the back-arc knolls region show a variety of REE signatures (LREE-depleted to LREE-enriched), with the majority of dredged rocks from the back-arc knolls showing rear-arc REE signatures that overlap with <7 Ma Western Seamounts dredged rocks (figure 11; Hochstaedter et al., 2000; Tollstrup et al., 2010). By reclassifying the outliers (rocks dredged from the back-arc knolls which show REE signatures similar to volcanic front or rift-related dredged rocks), I show a unified, LREE-enriched geochemical signature for back-arc knolls, which can also be grouped with <7 Ma Western Seamounts dredges.

RASC-type magmas form a medium-K series, with seamount-forming Western Seamounts magmas tending to a trend of greater potassium enrichment than knoll-forming back-arc knolls magmas (Figure 11). REE patterns show LREE enrichment (La/Yb 2.2-6.5), and increase in rare earth element concentration with increasing silica (figure 12). Normalized REE trends show

increasing MREE depletion with increasing silica, with La/Sm increasing from 2.2 in basalts to 2.8 in rhyolites and Dy/Yb decreasing from 1.8 in basalts to 1.5 in rhyolites. Western Seamounts rhyolites have slightly higher La/Sm (average 3.2) than back-arc knolls rhyolites (average 2.7). Overall rear-arc Zr/Y increases steadily from an average 2.9 in basalts to 4.5 in rhyolites.

RASC-type dredged rocks have overlapping Hf and Sr isotopic characteristics with rift-related rocks, e.g. lower epsilon Hf and $^{87}Sr/^{86}Sr$ than the volcanic front, but typically have lower epsilon Nd than rift-related samples. There is no difference in isotopic signature between Western Seamounts and back-arc knolls samples (figure 6, figure 13), and basalts through rhyolites have the same range. As with the rift-related series, RASC-type rocks have significantly lower epsilon Hf than Eocene-Oligocene tephras and drilled rocks from the Eocene rear-arc (figure 6; Straub et al., 2010; Hocking, 2016).

RASC-type and rift-related magmatism have a similar degree of progressive MREE depletion with increasing SiO_2 (figure 11). Haraguchi et al., (2017) used this to interpret that back-arc knolls basalts and rhyolites are non-cogenetic, but this could be caused by fractionation of a phase that preferentially partitions MREEs, e.g. amphibole or clinopyroxene.

6.2.4 Rear-arc origin of Site U1437 tephras

One important result of this study is the definitive evidence that RASC-type rhyolites were an important eruptive product from the Western Seamounts and back-arc knolls from 4.4-1.1 Ma. Whereas Ishizuka et al. (2003) dated only minor felsic rocks younger than 2.8 Ma, the existence of RASC-type rhyolites younger than 2.8 Ma was hinted at by undated back-arc knolls rhyolites from Haraguchi et al. (2017), the 2.6 Ma granodiorite Daisan West-Sumisu Knoll (Tani et al., 2015) and a hypothesized medium-K LREE-enriched felsic source for younger, RASC-type rear-

arc mud (Gill et al., 2018). The Site U1437 core contains rear-arc-derived felsic tephras

contiguously throughout the entire 4.4-1.1 Ma span sampled (figure 3). This well-dated tephra

dataset complements the record of rear-arc regional dredges, which have good representation of

mafic magmas, but poor representation of dated felsic magmas.

Tephras analyzed in this study from both Unit I and Unit II have rear-arc-like REE patterns

(most La/Yb 2.2-3.8), but most rhyolitic glass shards have lower, back-arc knolls-like La/Sm

(2.2-3.0), including rhyolitic glass from Unit II, despite Unit II's seamount-proximal regional

origin and Western Seamounts-like potassium enrichment (Figure 11). The youngest two

intervals considered in this study, U1437B-20F-2W-101/102 and U1437B-21F-1W-93/94, at

~1.1 Ma, contain dacites with a transitional chemistry between rift-related magmatism and

RASC-type magmatism (low to medium-K dacites and CaO/Al_2O_3 between rift-related and

RASC-type trends).

6.2.5 Potential source for Unit II rhyolites

Modally significant volcanic lapilli from Site U1437 Unit II tephras indicate that eruption was

relatively proximal to the drill site, within the Western Seamounts region (Busby et al, 2017).

Several Western Seamounts volcanoes are nearby, including Manji Seamount and Meireki

Seamount, both located within < 20 km of Site U1437 (figure 1). Both Manji and Meireki were

targeted for dredging by the R/V *Moana Wave* in the 1990s. Manji was the subject of more

intensive study than Meireki, due to the discovery of a porphyry copper-type hydrothermal

system on its summit (Ishizuka et al., 2002). Dredged rocks from Manji are basaltic andesites

through rhyolites, and dredged rocks from Meireki are basalts through rhyolites. K-Ar and

$^{40}Ar/^{39}Ar$ dating showed that Manji was active around 6-7 Ma (Ishizuka et al., 2002), while

Meireki was active later at 3.76 Ma (Ishizuka et al., 1998). The latter age is closer to the age of Unit II, which is 4.4 Ma.

Although ages of Unit II are closer to Meireki, geochemical comparison between samples from Meireki and Unit II do not provide a conclusive match (figure 15). Meireki rhyolites have considerably higher La/Yb than Unit II high-silica rhyolites, and lower Zr/Y than Unit II. One problem with the comparison to Meireki is that all the dredged Meireki rhyolites have identical geochemistry, perhaps representing sampling bias involved in dredging. If there is any compositional variation that could have provided a better match to Unit II, that was not sampled.

In addition, Jutzeler and Nichols (2016) showed seismic profiles and interpreted Unit II deposits ~2.7 km laterally towards a satellite cone on the flanks of Manji. Their interpretation is that Unit II represents mass wasting off of this satellite cone, and identifies Manji as the source of Unit II. If Manji is the source of Unit II, Unit II represents a 2 Myr extension of the known eruptive history of Manji.

6.2.6 Across-arc Trends in Felsic Magmas <7 Ma

Despite the fact that the Izu-Bonin subduction zone is perhaps the most well-studied intraoceanic arc on Earth, a common pitfall of ongoing work is the difficulty of integrating datasets from different studies. Dredge- and ROV-based studies (c.f. Hochstaedter et al., 2000; Tamura et al., 2009; Haraguchi et al., 2017) commonly provide broad geochemical datasets with good constraints on eruption location, but sparse geochronological information, while drillcore-based studies provide broad geochemical datasets with precise timing, but little information on eruption site beyond "proximal" or "distal". Within the Izu-Bonin, some degree of intercalation between

timing and eruption location is aided by the eastward progression of rear-arc volcanism over time.

Integrating the results from Site U1437 drilling and new dredge analyses (Haraguchi et al., 2017), I was able to reproduce the findings of Hochstaedter et al (2000) and Tollstrup et al. (2010). The Site U1437 tephra dataset fills in a gap in the literature of well-dated samples from 1-4 Ma, which represents the transition into arc extension/rifting and cessation of RASC-type magmatism.

Figure 16 illustrates this by plotting the composition of felsic magmas by distance to the volcanic front, and age as a proxy for distance to volcanic front. Felsic magmas show progressively more potassium-enrichment with distance to the volcanic front.

Among trace elements, some parameters show monotonically decreasing change along with distance from the volcanic front and age. Parameters that indicate slab signature change with distance to volcanic front and age, e.g. dacite and rhyolite La, Nb/Zr, Th, (figure 16), which is mirrored in the basaltic trends.

Other parameters do not vary monotonically across the arc: felsic magmas from the volcanic front and rift show step-wise decreases in Ba/La (figure 16) and increases in Zr/Y and ^{87}Sr/^{86}Sr (not shown), but there is no variation within each group with distance from the volcanic front.

This study for the first time provides a clear conceptual framework for variations in felsic magmas across time and space in the Izu-Bonin. Further discussion focuses on interpreting the petrogenetic origin of RASC-type rhyolites and implications for the development of the continental crust.

6.3 Differentiation within the Izu-Bonin rear-arc region

In the previous discussion, I have demonstrated a distinction between volcanic front, rift-related and RASC-type series, and how rhyolites vary geochemically across the arc. I have also shown a clear relationship between basalt type and rhyolite type within these segments. The next focus is to use the relationships between basalt and rhyolite types and speculate on the magmatic processes responsible for the origin of RASC-type rhyolites.

Determining the mechanism for rhyolite petrogenesis has important implications for understanding intracrustal differentiation leading to crustal growth. Within the Izu-Bonin and other intraoceanic subduction zones, the primary mechanism for intracrustal differentiation is contested. Traditional views suggest that felsic magmas are created through extreme crystal fractionation (Hochsteadter et al., 2000; Haraguchi et al., 2003; Wade et al., 2005), but many recent workers have suggested felsic magmas are created by anataxis of a heterogeneous crust that largely originated in the Oligocene (Kodaira et al., 2008; Tamura et al., 2009 Hariguchi et al., 2017). Many of the geochemical arguments in favor of crustal melting hinge on the fact that co-erupting mafic and felsic magmas have some different trace element characteristics (e.g. different Zr/Y, La/Sm, Dy/Yb; Tamura et al., 2000; Haraguchi et al., 2017). Considering this precedence in the literature, there is a need for consideration of geochemical relationships in contiguous magmatic suites from mafic to felsic, inclusive of intermediate magmas. Given that Site U1437 tephras form a continuous series representing RASC-type liquids of basaltic to rhyolitic composition, I consider different explanations for petrogenesis of Site U1437 rhyolites.

6.3.1 Evidence for fractional crystallization

Fractional crystallization has long been a main proposed mechanism in generating new felsic arc crust in the absence of ancestral sialic crust (Tuttle and Bowen, 1958), and is supported by a large body of literature on the role of fractional crystallization in the petrogenesis of intermediate and silicic magmas in intraoceanic settings. This has been recently highlighted in both modern arcs (e.g. Bryant et al., 2003; Machida and Ishii, 2003; Wade et al., 2005, Barker et al., 2012) and ancient accreted analogs (c.f. Greene et al., 2006; Jagoutz, 2010; Morris, 2017).

I examine one permissible scenario of differentiation through closed-system fractional crystallization of mafic magmas. Without the benefit of the corresponding cumulates and with a sample set biased towards silicic compositions, it is difficult to put geologic constraints on crystallization assemblage and order, especially at early crystallizing stages. Given limited information, I aim to reproduce the characteristics of felsic compositions representative of the RASC-type signature.

Differentiation of RASC-type magmas was modeled for both major and trace elements. Major element evolution used multi-step subtraction mass-balancing, using observed crystal chemistries with modal abundances chosen to best fit the observed glass chemistry liquid line of descent (LLD). Trace element evolution was modeled using the Rayleigh fractionation equation using mineral proportions obtained from major element modeling.

6.3.2 Subtraction modeling

I selected a primitive Unit I glass shard from this dataset as the parental liquid for subtraction modeling, U1437B-45X-1 79/80 basaltic glass with 50.5 wt. % SiO_2 (Mg# 42, shown with a black star on Figure 17). This does not necessarily reflect the true primary magma—comparison

with whole-rock analyses of previous RASC-type dredged lavas (Tollstrup et al., 2010) shows a subset of basalts with higher whole rock Mg#—but was chosen as the most primitive glass composition within our dataset at the beginning of a coherent trend in major and trace elements.

The fractionation sequence used was based on observed minerals within Site U1437 tephras, as well as observed minerals in the Cretaceous Alisitos Arc (Morris, 2017). The Alisitos Arc is an accreted mid- to upper-crustal section from an extensional intraoceanic arc that has been cited as an analog to the crust of the Izu-Bonin arc (Busby et al., 2006; Medynski et al., 2016; Morris, 2017). Mineral compositions are from mineral populations observed within the Site U1437 tephra suite as well as one amphibole composition observed in the Jurassic Talkeetna Arc (Johnson, MS thesis) which was used to represent a felsic amphibole (Mg# 49) typical of hydrous fractionation in a mid-to-upper crustal arc pluton.

The liquid line of descent represented by glass shard data (figure 17) was approximated in 3 stages, with different fractionating phases and proportions as follows (full modeling parameters are in Appendix C Table 1).

Step 1 fractionation models the change in parental magma from basalt to basaltic andesite (50.3-54.4 wt. % SiO_2) with a gabbronorite fractionating assemblage consisting of 39% plagioclase, 31% clinopyroxene, 16% orthopyroxene, and 14% FeTi oxides. This required 35% fractionation, from a melt fraction of F = 1 to F = 0.65.

Step 2 fractionation models the next step, from basaltic andesite to dacite (54.4-68.9 wt. % SiO_2) with a hornblende gabbronorite fractionating assemblage consisting of 32% plagioclase, 32% clinopyroxene, 5% orthopyroxene, 14% Fe-Ti oxides, 16% hornblende and 1% apatite. This required 35% fractionation, from a melt fraction of F = 0.65 to F = 0.3.

Step 3 fractionation attempts to model the most silicic compositions, from dacite to rhyolite

(68.9-76.4 wt. % SiO_2) with a hornblende gabbronorite fractionating assemblage consisting of

58% plagioclase, 19% clinopyroxene, 4% orthopyroxene, 12% FeTi oxides, 4% hornblende and

3% apatite. This required 7.5% fractionation, from a melt fraction of F = 0.30 to where the model

was terminated at F = 0.225 (76.4 wt. % SiO_2). Complications at this stage and higher SiO_2 are

discussed later in the text.

Modeled liquids generally reproduce the observed trends shown in the LLDs (figure 17),

indicating that simple fractional crystallization as modeled is a viable solution to create the major

element characteristics of rear-arc rhyolites. A few issues remain unresolved with major element

modeling: 1.) Subtraction modeling was unable to create the highest-K rhyolites represented

among Site U1437 tephras, but achieved appropriate compositions for medium-K rhyolites with

around 75-80% crystallization. Medium-K rhyolites, as modeled, are a common eruptive product

in the back-arc knolls portion of the rear-arc region. Higher percentages of K_2O were able to be

successfully produced by modeling K as a completely incompatible element, which is reflective

of mismatch between subtraction modeling and trace element modeling and is discussed below.

2.) Using erupted Fe-Ti oxide phenocrysts as a modeling phase results in rapid and unreasonable

depletion of magmatic TiO_2 (not shown). This has been noted in previous studies (e.g. Straub,

2008 and others) who suggest that erupted FeTi oxides may not be representative of the oxides

that contribute to early stages of differentiation, or alternatively that modeling fractionation with

observed phenocryst phases might not appropriately describe major element trends.

In order to evaluate fit, model liquid compositions were compared to observed glass

compositions at the end of Step 1 fractionation (F = 0.65, 54.4 wt. % SiO_2) and the end of Step 2

fractionation (F = 0.3, 68.1 wt. % SiO_2). Oxide values of modeled liquids were compared to the

average of glass oxide values within a SiO_2 range of 2.5 wt. %. Error, as expressed by [Model value]/[Average of glass +/- 2.5 wt. % SiO_2], was under 20%, except in a few instances where abundances were low (e.g. MgO at the end of Stage 2 modeling) and mismatch between model and glasses were on the order of analytical error (figure 18). Error was not evaluated for TiO_2, MnO, or Na_2O. In all major elements, error propagated as the model went on, resulting in the highest degree of error at the end of Step 3 fractionation (dacite to rhyolite).

6.3.3 Trace element modeling

Crystallizing assemblages and proportions from the major element subtraction model were used in trace element fractionation modeling of the same glass populations. The same basaltic shard from U1437B-45x-1 79-80 (50.5 wt. % SiO_2) was chosen as the parental liquid, and liquid evolution was modeled with the same three different fractionating assemblages as described for major elements (full details in Appendix C Table 3). Partition coefficients were chosen from literature values (Appendix C Table 4). Where K_D sets were incomplete, values from the literature were interpolated.

Modelling of the REEs show good agreement with observed REEs in basaltic through rhyolitic glass shards (Figure 19, modelled liquids shown in dashed lines). On Figure 20, trace element covariances of observed glass compositions are closely modeled by the calculated liquid from basalt to rhyolites, with the exception of rhyolites with $SiO_2 > 73$ wt. %. This corresponds to the silica value within the sample set above which REEs no longer behave as incompatible elements (see figure 5) and is not modelled.

Major element subtraction and trace element modeling are independently successful at modelling rhyolites with the characteristic RASC-type signature, however there are slight problems in

reconciling the two. Modeled REE patterns match measured glass REEs, but in comparison to major element modeling, trace element modeling requires a higher degree of crystallization (i.e. lower melt fraction) to reproduce the characteristics of rhyolitic glass. Two sources of error likely contribute to this: 1.) incorrect fractionation assemblage, and 2.) error in selecting appropriate partition coefficients from the literature. Previous studies have commented on the difficulty of modeling fractionation of mafic magmas in arc settings (Gill, 1981; Straub, 2008). Both mafic glasses and crystals are underrepresented in explosive records and the bulk of mafic differentiation likely occurs far from the surface, which leads to poor preservation of this part of the differentiation process. Attempts to amend the mafic fractionating assemblage were unsuccessful using the observed phenocrysts and it is likely that observed phenocrysts in Site U1437 tephras are not representative of the hidden mafic/ultramafic cumulates involved in this stage of fractionation. Another possibility is that the individual or bulk partition coefficients used in this study do not accurately represent the conditions of differentiation, especially for felsic magmas that are saturated with accessory minerals (e.g. apatite, titanite, zircon) whose published partition coefficients vary widely and can strongly influence trace element systematics in the residual liquid (Rollinson, 1993; Glazner et al., 2008).

Although in some ways the mismatch between the major element and trace element modeling is problematic, creating rhyolites with a higher degree of crystallization remedies the problem of insufficiently high rhyolite K_2O as observed in major element subtraction modeling. As an exercise, potassium was modeled as a purely incompatible element ($D = 0$) and fractionated alongside other elements. Figure 20 shows that the 2.5-3.5 wt. % K_2O present in high-K rhyolites in Site U1437 tephras is matched by the model at $F = 0.2$-0.125, whereas the 1.5-2.5 wt. % K_2O present in medium-K rhyolites is effectively matched by the model at $F = 0.3$-0.2.

Above 73 wt. % SiO$_2$, rhyolites fall off the modeled trace element trend and generally show a greater degree of trace element heterogeneity (figure 20). This is in accordance with an increasingly large body of literature that suggests that felsic magma chambers exhibit many factors that cause them to deviate from normal fractional crystallization behavior. Felsic eruptive products may represent eruption of interstitial liquid from a cool, rheologically locked crystal mush (Bachmann and Bergantz, 2004; Hildreth and Wilson, 2007; Cooper and Kent, 2014). Shallow crustal magma chambers are likely saturated with small modal percents of non-ferromagnesian accessory phases (e.g. apatite, titanite, zircon) as well as hornblende, which are important reservoirs for rare earth elements (Glazner et al., 2008; Brophy, 2008) and can enhance geochemical variability among rhyolites. Although fractionation at this stage is not quantitatively modeled, examining variation among rhyolites shows that with enriching silica, rhyolites evolve to higher La/Sm and lower Dy/Lu (figure 20). This suggests that fractionation at this phase may be controlled by a phase that preferentially partitions MREEs, e.g. hornblende, apatite or titanite.

6.3.4 Role for amphibole

An important result from this trace element modeling regards the fractionation of amphibole. Amphibole is an important phenocryst phase in arc magmatism and the generation of continental crust-like geochemical signature (Ridolfi et al., 2009), but there is disagreement how, where, and when amphibole crystallization typically occurs: early in the differentiation process (Greene et al., 2006; Davidson et al., 2007; Jagoutz, 2010) or as a late-stage crystallizing phase (Morris, 2017); in lower crustal hot zones (Annen et al., 2006, Davidson et al., 2007) or midcrustal magma chambers (Barker et al., 2012; Morris, 2017).

Various lines of evidence can be extended to support amphibole as a late-stage crystallizing phase. Within the Izu-Bonin, all regions except the volcanic front show progressive MREE depletion between co-spatial mafic and felsic magmas. Rear-arc seamount chain-type samples with Mg# > 35 (generally basalts through andesites) have higher Dy/Lu (average 11.8) than in more evolved magmas (Mg# < 35, SiO_2 > 63 %), which trend towards lower Dy/Lu (average 10.1) (figure 11). This decrease in Dy/Lu is reproduced in the results of subtraction modeling described earlier, which fractionate amphibole starting in Step 2 (SiO_2 wt. % 54.4-68.01) and continuing to more felsic magmatic compositions.

Since the partition coefficients for amphibole follow the same trends as partition coefficients for clinopyroxene (high K_{DS} for MREEs) and because of the non-unique nature of fractionation modeling, trace element modeling does not rule out fractionation of minor amphibole at an earlier stage in the differentiation process and/or a lower level; however, amphibole K_{DS} are generally higher than clinopyroxene K_{DS} (Davidson et al., 2007) thus early amphibole crystallization would raise early bulk distribution coefficients. Izu-Bonin RASC-type magmas show steadily increasing REE concentrations with increasing silica, whereas magmas that experience significant early amphibole crystallization are predicted to have constant REE concentrations (Brophy, 2008).

Arguments from petrography and thermobarometry suggest shallow, late-stage crystallization of amphibole-bearing magmas. Amphiboles within Unit II rhyolites yielded shallow midcrustal pressures (1.4-1.7 kbar or ~6 km). Within the rear-arc, amphibole has been most commonly observed in association with rhyolitic magmas (Hochstaedter et al, 2000; Machida et al., 2008; Straub, 2008), and is a modally significant phenocryst phase in felsic plutonic rocks from the Izu-Bonin arc (Haraguchi et al., 2003; Tani et al., 2015).

6.3.5 Criticisms for fractional crystallization

One of the major criticisms for fractional crystallization as a predominant mode for the petrogenesis of silicic arc magmas is that creating the large volumes of silicic magmas that are erupted require a large degree of fractional crystallization and would create an enormously large reciprocal volume of mafic and ultramafic cumulates within the crust. However, if a crustal anatexis model is favored, this problem would necessitate similarly large volumes of mafic restites to exist within or at the base of the crust. Typical solutions to this problem involve delamination of crustal roots (Tatsumi, 2005; Jagoutz, 2010) which has been observed in the Mariana forearc, where Philippine Sea Plate-signature crustal xenoliths are exposed embedded in lithospheric mantle (Reagan et al., 2017). Tatsumi et al. (2008) modeled a seismically invisible layer of mafic/ultramafic restites or cumulates within the Izu-Bonin that was 3-9 times greater than the base of the seismically defined lower-crust on the basis of thermal arguments, which could potentially delaminate and recycle into the mantle (Tatsumi et al., 2014). Additional models for the petrogenesis of intermediate and felsic magmas (e.g. Straub et al., 2008) offer ways to solve the problems posed by crustal mass balance.

6.4 Role for crustal melting?

Although the traditional view on generation of silicic magmas in intraoceanic arcs has been through fractional crystallization, an increasing body of literature explains intraoceanic arc rhyolites as the products of large-scale melting of pre-existing crust (Tamura and Tatsumi, 2002; Tamura et al., 2009). These hypotheses involve melting of basaltic or andesitic crustal components typically occurring within the midcrust. In these scenarios, the composition of pre-existing crust is a strong control of the composition of rhyolites produced by melting. Because of this and other reasons, developing a more holistic understanding of midcrustal composition has

been a topic of much inquiry (Johnson et al., 2014; Tani et al., 2015; Haraguchi et al., 2017) and has important implications for understanding crustal mass balance and the bulk architecture of the crust, in arc settings and beyond.

One method to probe the composition of the midcrust is to examine regional eruptive products, especially felsic magmas, which must be representative of compositions added or removed from the midcrust. To this end, I examine two in-situ/near-in-situ rhyolites from Site U1437: Unit II, a near-in-situ 4.4 Ma rhyolitic tephra, and Igneous Unit 1, a 12.9 Ma intrusive rhyolitic sheet. Despite their similar location, the two rhyolitic bodies have very different chemistries (figure 21). The 12.9 Ma rhyolitic sill is low-K in character, with flat- to mildly- LREE-enriched REE patterns (La/Sm = 1.9-2.4) and overall lower REE abundances (Table 6). The same low-K, less LREE-enriched signature is also found in >12.9 Ma lava clasts from Site U1437 Unit VII, showing that the chemistry of 12.9 Ma rhyolites corresponds with the chemistries of contemporaneous 12.9 Ma mafic and intermediate volcanics (Sato et al., submitted). This contrasts with the med-high K, LREE-enriched character of Unit II (La/Sm = 2.4-3.3), which is well in line with <6 Ma RASC-type signature.

Rhyolites from the Izu-Bonin show remarkable coherency in their composition as a function of space and time, which is problematic considering petrogenesis scenarios that call for widescale melting of pre-existing crust, e.g. Tamura et al., 2009. Rhyolites produced by crustal melting must reflect the isotope, K_2O and REE signature of their crustal sources (Sisson et al., 2005; Tani et al., 2016). If the low-K rhyolitic sill is representative of a regional low-K crustal signature at 12.9 Ma, a med- to high-K rhyolite produced by crustal melting at 4.4 Ma must then be from preferentially melting of only young (<12.9 Ma), K-enriched crust. Neither the geochemical character of inferred Eocene and Oligocene crust (figure 21; Straub et al., 2010; Ishizuka et al.,

2011; Hocking, 2016) nor the observed 12.9 Ma crustal contributions are compatible as a primary source for melting and/or a significant mixing end-member to explain geochemical trends culminating in the characteristic RASC-type rhyolites of the Site U1437 tephras.

Within Izu-Bonin magmas there is evidence for open-system processes, although estimates vary for the amount open-system processes contribute to differentiation. Complex relationships involving mixing are ubiquitous among mid-crustal exposures of accreted arcs (DeBari and Greene, 2011; Morris, 2017), even where simple fractionation is interpreted as the main mechanism of intracrustal differentiation. Machida and Ishii (2003) examined bulk rock trace element geochemistry and mineralogical textures among a subset of Izu-Bonin RASC-type magmas and determined that <5 Ma felsic magmas were created via coupled fractionation and open-system magma mixing. Unit II plagioclase crystals show low $\delta 18O$ values, which Barker et al. (2016) used to reason that rear-arc rhyolites are created through assimilation-fractional crystallization (AFC; DePaolo, 1981; Bohrson and Spera, 2007) involving around 30% assimilation of high temperature altered mafic volcanics.

Our fractional crystallization modeling does not account for open-system processes, but consideration of isotopic and REE evidence suggests that open-system processes, if present, involve predominantly younger (<12.9 Ma) RASC-type signature crustal sources. This has been hypothesized by Sisson et al. (2014) to explain magmatic diversity within the Cascades, where the primary assimilants involved in AFC are previously intruded magmas from the same volcanic system. This is difficult to distinguish from predominantly closed-system fractional crystallization models and cannot be ruled out without careful consideration of isotopes. However, if the products of contemporaneous fractionation are the predominant crustal

assimilant within the Izu-Bonin, large-scale melting of <12.9 Ma midcrust should not be called upon to contribute volume and chemistry to voluminous rhyolitic volcanism.

7. Summary

Volcanism within the studied region of the Izu-Bonin Arc can be divided into three regions, each with their own geochemical signature. These geochemical signatures represent three coherent suites of magmas, from basalts through rhyolites with distinct trace element and isotope systematics. The volcanic front series consists of low-K, LREE-depleted magmas from the dominantly basaltic edifices of the volcanic front. The rift-related series consists of low-K, flat-pattern REE magmas from the <1 Ma rift, R2 rhyolitic centers in and slightly behind the main volcanic front (described by Tamura et al., 2009), and the eastern portion of the backarc knolls region. The rear-arc seamount chain type (RASC-type) series consists of med- to high-K, LREE-enriched magmas from the western portion of the backarc knolls region and the eastern portion of the Western Seamounts across-arc seamount chains. Magmas with these three geochemical signatures have coherent differences in space and time. This analysis is not inclusive of magmas older than 7 Ma or west of 138º 50', where additional complexity has been documented (Hochstaedter et al., 2000, Machida and Ishii, 2003, Sato et al., submitted).

I describe a suite of rear-arc derived, RASC-type signature tephras from IODP Site U1437, aged 4.4-1.1 Ma. Glass compositions from Site U1437 tephras form a medium- to high-K series, LREE-enriched signatures with REE abundances increasing with SiO_2 then decreasing above 73 wt. % SiO_2. The sample suite contains abundant RASC-type signature rhyolites throughout the 4.4-1.1 Ma timespan, which is the first documentation of RASC-type rhyolites of this age.

Among the intervals studied are rhyolitic intervals from Unit II, a deposit of rhyolite lapillituffs/lapillistones of relatively proximal origin to Site U1437. Manji and Meireki Seamounts, within the Manji Seamount Chain, are both within 20 km to Site U1437 and are potential sources for Unit II. However, higher La/Yb and interpretation of seismic profiles (Jutzeler and Nichols, 2016) point to sourcing from a satellite cone on the flank of Manji Seamount. If Unit II is derived from Manji, this would represent volcanism that is 2 Myr younger than other dated Manji volcanics.

Geochemical modeling demonstrates that the major and trace element characteristics of rear-arc magmas can be explained via closed-system fractional crystallization as the main driver of differentiation. RASC-type signature rhyolites can be produced through 70-80% fractionation from a basaltic parent. Amphibole is involved primarily at the later stages of differentiation, which is interpreted to occur in shallow mid-crustal magma chambers. Above 73 wt. % SiO_2, rhyolitic glass REE abundances decrease, along with increasing La/Sm and decreasing Dy/Yb. I interpret this to result from late stage crystallizing phase that preferentially partitions MREEs, such as hornblende, apatite or titanite.

Occasional mineral disequilibrium textures, mafic enclaves in felsic plutons (Tani et al, 2015), decreased oxygen isotopes (Barker et al., 2016), and non-perfect fractionation trends indicate that open-system processes are likely partially involved in RASC-type rhyolite petrogenesis. However, the <7 Ma RASC-type rhyolite signature is very different from older RASC-type rhyolites, as seen in the 12.9 Ma Igneous Unit 1.   Melting of crustal sources that are cogenetic to Igneous Unit 1 cannot create rhyolites with compatible K_2O or REE systematics to Unit II. The 12.9 Ma or older crust does not have the appropriate compositions to be either a crustal source for melting or a mixing end member involved in the petrogenesis of <7 Ma rear-arc magmas.

Thus I favor a model that relies on fractional crystallization to generate intermediate to felsic magmas, with only a limited role for magma mixing and crustal anatexsis. The latter, if present, must only involve young (<12.9 Ma) RASC-type signature sources, as older Eocene-and Oligocene sources have incompatible Hf isotopic signatures.

If fractionation is the dominant mechanism for intracrustal differentiation, midcrustal processes must be dominantly constructive and act to enhance mid-crustal diversity over time though the addition of new material. This contributes to the development of chemically heterogeneous mid-crustal low-velocity layer, which in turn is inherited as the unsubductable nucleus of continental crust.

Works Cited

Anderson, J. L., & Smith, D. R. (1995). The effects of temperature and fO$_2$ on the Al-in-hornblende barometer. *American Mineralogist*, *80*(5–6), 549–559.

Annen, C., Blundy, J. D., & Sparks, R. S. J. (2005). The genesis of intermediate and silicic magmas in deep crustal hot zones. *Journal of Petrology*, *47*(3), 505–539.

Arth, J. G. (1976). Behavior of trace elements during magmatic processes: a summary of theoretical models and their applications. J. Res. US Geol. Surv.;(United States), 4(1).

Bachmann, O., & Bergantz, G. W. (2004). On the origin of crystal-poor rhyolites: extracted from batholithic crystal mushes. *Journal of Petrology*, *45*(8), 1565–1582.

Bacon, C. R., & Hirschmann, M. M. (1988). Mg/Mn partitioning as a test for equilibrium between coexisting Fe-Ti oxides. *American Mineralogist*, *73*(1–2), 57–61.

Bandy, W. L., & Hilde, T. W. (1983). Structural features of the Bonin arc: implications for its tectonic history. *Tectonophysics*, *99*(2–4), 331–353.

Barker A., Muir D., Harris C., & Troll V. (2016) *Goldschmidt Abstracts*, 2016 162

Barker, S. J., Wilson, C. J. N., Baker, J. A., Millet, M.-A., Rotella, M. D., Wright, I. C., & Wysoczanski, R. J. (2012). Geochemistry and petrogenesis of silicic magmas in the intra-oceanic Kermadec arc. *Journal of Petrology*, *54*(2), 351–391.

Behn, M. D., Kelemen, P. B., Hirth, G., Hacker, B. R., & Massonne, H.-J. (2011). Diapirs as the source of the sediment signature in arc lavas. *Nature Geoscience*, *4*(9), 641.

Bouvier, A., Vervoort, J. D., & Patchett, P. J. (2008). The Lu–Hf and Sm–Nd isotopic composition of CHUR: Constraints from unequilibrated chondrites and implications for the bulk composition of

terrestrial planets. Earth and Planetary Science Letters, 273(1), 48–57.

https://doi.org/10.1016/j.epsl.2008.06.010

Brophy, J. G. (2008). A study of rare earth element (REE)–SiO 2 variations in felsic liquids generated by

basalt fractionation and amphibolite melting: a potential test for discriminating between the two

different processes. *Contributions to Mineralogy and Petrology*, *156*(3), 337–357.

Bryant, C. J., Arculus, R. J., & Eggins, S. M. (1999). Laser ablation–inductively coupled plasma–mass

spectrometry and tephras: a new approach to understanding arc-magma genesis. *Geology*, *27*(12),

1119–1122.

Bryant, C. J., Arculus, R. J., & Eggins, S. M. (2003). The geochemical evolution of the Izu-Bonin arc

system: A perspective from tephras recovered by deep-sea drilling. *Geochemistry, Geophysics,*

Geosystems, *4*(11).

Busby, C., Adams, B. F., Mattinson, J., & Deoreo, S. (2006). View of an intact oceanic arc, from surficial

to mesozonal levels: Cretaceous Alisitos arc, Baja California. *Journal of Volcanology and*

Geothermal Research, *149*(1–2), 1–46.

Cooper, K. M., & Kent, A. J. (2014). Rapid remobilization of magmatic crystals kept in cold

storage. *Nature*, *506*(7489), 480.

Data and Sample Research System for Whole Cruise Information in JAMSTEC (DARWIN). (2014).

Rock sample data for Aogashima volcano. Retrieved from

http://www.godac.jamstec.go.jp/darwin/e

Davidson, J., Turner, S., Handley, H., Macpherson, C., & Dosseto, A. (2007). Amphibole "sponge" in arc

crust? *Geology*, *35*(9), 787–790.

DeBari, S. M., & Greene, A. R. (2011). Vertical stratification of composition, density, and inferred

    magmatic processes in exposed arc crustal sections (pp. 121–144). Springer.

Drake, M. J., & Weill, D. F. (1975). Partition of Sr, Ba, Ca, Y, Eu2+, Eu3+, and other REE between

    plagioclase feldspar and magmatic liquid: an experimental study. Geochimica et Cosmochimica

    Acta, 39(5), 689–712.

Evans, B. W., Scaillet, B., & Kuehner, S. M. (2006). Experimental determination of coexisting iron–

    titanium oxides in the systems FeTiAlO, FeTiAlMgO, FeTiAlMnO, and FeTiAlMgMnO at 800

    and 900 C, 1–4 kbar, and relatively high oxygen fugacity. *Contributions to Mineralogy and*

    Petrology, *152*(2), 149–167.

Fiske, R. S., Naka, J., Iizasa, K., Yuasa, M., & Klaus, A. (2001). Submarine silicic caldera at the front of

    the Izu-Bonin arc, Japan: Voluminous seafloor eruptions of rhyolite pumice. *Geological Society*

    of America Bulletin, *113*(7), 813–824.

Fryer, P., & Pearce, J. A. (1992). Introduction to the scientific results of Leg 125. *Proceedings of the*

    Ocean Drilling Program, Scientific Results, 125, 3-11.

Fujimaki, H. (1986). Partition coefficients of Hf, Zr, and REE between zircon, apatite, and

    liquid. *Contributions to Mineralogy and Petrology*, *94*(1), 42–45.

Fujimaki, H., Tatsumoto, M., & Aoki, K. (1984). Partition coefficients of Hf, Zr, and REE between

    phenocrysts and groundmasses. *Journal of Geophysical Research: Solid Earth*, *89*(S02).

Gill, J. B. (1981). Orogenic andesites and plate tectonics. Berlin: Springer-Verlag.

Gill J. B., Bongiolo E. M., Miyazaki T., Hamelin C., Jutzeler M., DeBari S., … Yakavonis M. (2018).

    Tuffaceous Mud is a Volumetrically Important Volcaniclastic Facies of Submarine Arc

Volcanism and Record of Climate Change. *Geochemistry, Geophysics, Geosystems*, *0*(0). https://doi.org/10.1002/2017GC007300

Gill, J. B., Hiscott, R. N., & Vidal, P. (1994). Turbidite geochemistry and evolution of the Izu-Bonin arc and continents. *Lithos*, *33*(1–3), 135–168.

Glazner, A. F., Coleman, D. S., & Bartley, J. M. (2008). The tenuous connection between high-silica rhyolites and granodiorite plutons. *Geology*, *36*(2), 183–186.

Green, T. H., & Pearson, N. J. (1985). Experimental determination of REE partition coefficients between amphibole and basaltic to andesitic liquids at high pressure. *Geochimica et Cosmochimica Acta*, *49*(6), 1465–1468.

Greene, A. R., Debari, S. M., Kelemen, P. B., Blusztajn, J., & Clift, P. D. (2006). A detailed geochemical study of island arc crust: the Talkeetna arc section, south–central Alaska. *Journal of Petrology*, *47*(6), 1051–1093.

Hanyu, T., Tatsumi, Y., Nakai, S., Chang, Q., Miyazaki, T., Sato, K., … Yoshida, T. (2006). Contribution of slab melting and slab dehydration to magmatism in the NE Japan arc for the last 25 Myr: Constraints from geochemistry. *Geochemistry, Geophysics, Geosystems*, *7*(8).

Haraguchi, S., Ishii, T., Kimura, J.-I., & Ohara, Y. (2003). Formation of tonalite from basaltic magma at the Komahashi-Daini Seamount, northern Kyushu-Palau Ridge in the Philippine Sea, and growth of Izu-Ogasawara (Bonin)-Mariana arc crust. *Contributions to Mineralogy and Petrology*, *145*(2), 151–168.

Haraguchi, S., Kimura, J.-I., Senda, R., Fujinaga, K., Nakamura, K., Takaya, Y., & Ishii, T. (2017). Origin of felsic volcanism in the Izu arc intra-arc rift. *Contributions to Mineralogy and Petrology*, *172*(5), 25.

Hart, S. R. (1984). A large-scale isotope anomaly in the Southern Hemisphere mantle. *Nature*, *309*(5971), 753.

Hildreth, W., & Wilson, C. J. (2007). Compositional zoning of the Bishop Tuff. *Journal of Petrology*, *48*(5), 951–999.

Hochstaedter, A. G., Gill, J. B., Kusakabe, M., Newman, S., Pringle, M., Taylor, B., & Fryer, P. (1990a). Volcanism in the Sumisu Rift, I. Major element, volatile, and stable isotope geochemistry. *Earth and Planetary Science Letters*, *100*(1–3), 179–194.

Hochstaedter, A. G., Gill, J. B., & Morris, J. D. (1990b). Volcanism in the Sumisu Rift, II. Subduction and non-subduction related components. *Earth and Planetary Science Letters*, *100*(1–3), 195–209.

Hochstaedter, A. G., Gill, J. B., Taylor, B., Ishizuka, O., Yuasa, M., & Monta, S. (2000). Across-arc geochemical trends in the Izu-Bonin arc: Constraints on source composition and mantle melting. *Journal of Geophysical Research: Solid Earth*, *105*(B1), 495–512.

Hochstaedter, A., Gill, J., Peters, R., Broughton, P., Holden, P., & Taylor, B. (2001). Across-arc geochemical trends in the Izu-Bonin arc: Contributions from the subducting slab. *Geochemistry, Geophysics, Geosystems*, *2*(7).

Hocking, B. D. (2016). *Implications of Hf-Nd Isotopes in West Philippine Basin Basalts for the Initiation and Early History of the Izu-Bonin-Mariana Arc.* MS thesis, University of South Carolina.

Ikeda, Y., & Yuasa, M. (1989). Volcanism in nascent back-arc basins behind the Shichito Ridge and adjacent areas in the Izu-Ogasawara arc, northwest Pacific: evidence for mixing between E-type MORB and island arc magmas at the initiation of back-arc rifting. *Contributions to Mineralogy and Petrology*, *101*(4), 377–393.

Ishizuka, O., Uto, K., Yuassa, M., & Hochstaedter, A. (1998). K–Ar ages from seamount chains in the back-arc region of the Izu–Ogasawara arc. Island Arc, 7(3), 408–421.

Ishizuka, O., Yuasa, M., & Uto, K. (2002). Evidence of porphyry copper-type hydrothermal activity from a submerged remnant back-arc volcano of the Izu-Bonin arc: implications for the volcanotectonic history of back-arc seamounts. Earth and Planetary Science Letters, 198(3), 381–399.

Ishizuka, O., Uto, K., Yuasa, M., & Hochstaedter, A. G. (2003). Volcanism in the earliest stage of back-arc rifting in the Izu-Bonin arc revealed by laser-heating 40Ar/39Ar dating. *Journal of Volcanology and Geothermal Research*, *120*(1), 71–85.

Ishizuka, O., Yuasa, M., & Uto, K. (2002). Evidence of porphyry copper-type hydrothermal activity from a submerged remnant back-arc volcano of the Izu-Bonin arc: implications for the volcanotectonic history of back-arc seamounts. *Earth and Planetary Science Letters*, *198*(3), 381–399.

Ishizuka, O., Taylor, R. N., Yuasa, M., Milton, J. A., Nesbitt, R. W., Uto, K., & Sakamoto, I. (2007). Processes controlling along-arc isotopic variation of the southern Izu-Bonin arc. Geochemistry, Geophysics, Geosystems, 8(6).

Ishizuka, O., Taylor, R. N., Yuasa, M., & Ohara, Y. (2011). Making and breaking an island arc: A new perspective from the Oligocene Kyushu-Palau arc, Philippine Sea. Geochemistry, Geophysics, Geosystems, 12(5).

Jagoutz, O. E. (2010). Construction of the granitoid crust of an island arc. Part II: a quantitative petrogenetic model. *Contributions to Mineralogy and Petrology*, *160*(3), 359–381.

Johnsen, M. (2007). *Geochemical composition of the Western Talkeetna Island arc crustal section, Lower Cook Inlet region, Alaska: implications for crustal growth along continental margins*. Western Washington University.

Johnson, D., Hooper, P., & Conrey, R. (1999). XRF Method XRF Analysis of Rocks and Minerals for

    Major and Trace Elements on a Single Low Dilution Li-Tetraborate Fused Bead. *Advances in X-*

    Ray Analysis, *41*, 843–867.

Johnson, J. A., Hickey-Vargas, R., Fryer, P., Salters, V., & Reagan, M. K. (2014). Geochemical and

    isotopic study of a plutonic suite and related early volcanic sequences in the southern Mariana

    forearc. *Geochemistry, Geophysics, Geosystems*, *15*(3), 589–604.

Johnson, M. (2007) *Geochemical Composition of the Western Talkeetna Island Arc Crustal Section,*

    Lower Cook Inlet Region, Alaska: Implications for Crustal Growth Along Continental Margins.

    MS thesis, Western Washington University.

Jordan, E. K., Lieu, W, Stern, R. J., Carr, M. J., Feigenson, M. D., & Gill, J. B. (2012): CentAm & IBM

    Geochem Database version 1.02. Interdisciplinary Earth Data Alliance (IEDA).

    http://dx.doi.org/10.1594/IEDA/100053. Accessed 21 May 2018.

Jutzeler, M. & Nichols, A. (2015) Provenance and characteristics of Unit II, IODP Expedition 350 Post-

    cruise Meeting, Marrakesh, Morocco, 2016.

Kay, R. W., & Kay, S. M. (1993). Delamination and delamination magmatism. Tectonophysics, 219(1–

    3), 177–189.

Kimura, J.-I., Kent, A. J., Rowe, M. C., Katakuse, M., Nakano, F., Hacker, B. R., … Stern, R. J. (2010).

    Origin of cross-chain geochemical variation in Quaternary lavas from the northern Izu arc: using

    a quantitative mass balance approach to identify mantle sources and mantle wedge

    processes. *Geochemistry, Geophysics, Geosystems*, *11*(10).

Kimura Jun-Ichi, Nagahashi Yoshitaka, Satoguchi Yasufumi, & Chang Qing. (2015). Origins of felsic

    magmas in Japanese subduction zone: Geochemical characterizations of tephra from caldera-

forming eruptions <5 Ma. *Geochemistry, Geophysics, Geosystems*, *16*(7), 2147–2174. https://doi.org/10.1002/2015GC005854

Klemme, S., Günther, D., Hametner, K., Prowatke, S., & Zack, T. (2006). The partitioning of trace elements between ilmenite, ulvospinel, armalcolite and silicate melts with implications for the early differentiation of the moon. *Chemical Geology*, *234*(3), 251–263.

Knaack, C., Cornelius, S. B., & Conrey, R. M. (1994). Trace Element Analysis of Rocks and Minerals by ICP-MS, GeoAnalytical Lab, Washington State University.

Kodaira, S., Sato, T., Takahashi, N., Yamashita, M., No, T., & Kaneda, Y. (2008). Seismic imaging of a possible paleoarc in the Izu-Bonin intraoceanic arc and its implications for arc evolution processes. *Geochemistry, Geophysics, Geosystems*, *9*(10).

Lange, R. A., Frey, H. M., & Hector, J. (2009). A thermodynamic model for the plagioclase-liquid hygrometer/thermometer. *American Mineralogist*, *94*(4), 494–506.

Leat, P. T., & Larter, R. D. (2003). Intra-oceanic subduction systems: introduction. *Geological Society, London, Special Publications*, *219*(1), 1–17.

Lepage, L. D. (2003). ILMAT: an Excel worksheet for ilmenite–magnetite geothermometry and geobarometry. *Computers & Geosciences*, *29*(5), 673–678.

Machida, S., & Ishii, T. (2003). Backarc volcanism along the en echelon seamounts: The Enpo seamount chain in the northern Izu-Ogasawara arc. *Geochemistry, Geophysics, Geosystems*, *4*(8).

Machida, S., Ishii, T., Kimura, J.-I., Awaji, S., & Kato, Y. (2008). Petrology and geochemistry of cross-chains in the Izu-Bonin back arc: Three mantle components with contributions of hydrous liquids from a deeply subducted slab. *Geochemistry, Geophysics, Geosystems*, *9*(5).

Maas, R., Kamenetsky, M.B., Sobolev, A.V., Kamenetsky, V.S., Sobolev, N.V., 2005. Sr-Nd-Pb isotopic evidence for a mantle origin of alkali chlorides and carbonates in the Udachnaya kimberlite, Siberia. Geology, 35: 549-552.

McDonough, W. F., & Sun, S.-S. (1995). The composition of the Earth. *Chemical Geology*, *120*(3–4), 223–253.

Medynski, S., Busby, C., DeBari, S. M., Morris, R., Andrews, G. D., Brown, S. R., & Schmitt, A. K. (2016). The Upper- to Middle-Crustal Section of the Alisitos Oceanic Arc, (Baja, Mexico): an Analog of the Izu-Bonin-Marianas (IBM) Arc. AGU Fall Meeting Abstracts, 13, V13C–2866. Retrieved from http://adsabs.harvard.edu/abs/2016AGUFM.V13C2866M

Morris, R. A. (2017). *Building Arc Crust – Plutonic to Volcanic Connections in an Extensional Island Arc, the Alisitos Arc Crustal Section (Southern Rosario Segment), Baja California.* MS thesis, Western Washington University.

Münker, C., Weyer, S., Scherer, E., Mezger, K., 2001. Separation of high field strength elements (Nb, Ta, Zr, Hf) and Lu from rock samples for MC-ICPMS measurements. Geochem Geophys Geosys, 2(12): doi:10.1029/2001GC000183.

Nash, W. P., & Crecraft, H. R. (1985). Partition coefficients for trace elements in silicic magmas. *Geochimica et Cosmochimica Acta*, *49*(11), 2309–2322.

Pearce, J. A., & Norry, M. J. (1979). Petrogenetic implications of Ti, Zr, Y, and Nb variations in volcanic rocks. *Contributions to Mineralogy and Petrology*, *69*(1), 33–47.

Pin, C., Briot, D., Bassin, C., Poitrasson, F., 1994. Concomitant separation of strontium and samarium-neodymium for isotopic analysis in silicate samples, based on specific extraction chromatography. Analytica Chimica Acta, 298: 209-217.

Pin, C., Santos-Zalduegui, J.F., 1997. Sequential separation of light rare-earth elements, thorium and

uranium by miniaturized extraction chromatography: Application to isotopic analyses of silicate

rocks. Analytica Chimica Acta, 339: 79-89.

Putirka, K. D. (2008a). Thermometers and barometers for volcanic systems. *Reviews in Mineralogy and Geochemistry*, *69*(1), 61–120.

Putirka, K. D. (2008b). Thermometers and Barometers for Volcanic Systems. *Reviews in Mineralogy and Geochemistry*, *69*(1), 61–120. https://doi.org/10.2138/rmg.2008.69.3

Reagan, M. K., Heywood, L., Goff, K., Michibayashi, K., Foster, C. T., Jicha, B., … Righter, M. (2018). Geodynamic implications of crustal lithologies from the southeast Mariana forearc. *Geosphere*, *14*(1), 1–22.

Reagan, M. K., Ishizuka, O., Stern, R. J., Kelley, K. A., Ohara, Y., Blichert-Toft, J., … Hanan, B. B. (2010). Fore-arc basalts and subduction initiation in the Izu-Bonin-Mariana system. *Geochemistry, Geophysics, Geosystems*, *11*(3).

Reubi, O., & Blundy, J. (2009). A dearth of intermediate melts at subduction zone volcanoes and the petrogenesis of arc andesites. *Nature*, *461*(7268), 1269.

Ridolfi, F., & Renzulli, A. (2012). Calcic amphiboles in calc-alkaline and alkaline magmas: thermobarometric and chemometric empirical equations valid up to 1,130° C and 2.2 GPa. *Contributions to Mineralogy and Petrology*, *163*(5), 877–895.

Ridolfi, F., Renzulli, A., & Puerini, M. (2010). Stability and chemical equilibrium of amphibole in calc-alkaline magmas: an overview, new thermobarometric formulations and application to subduction-related volcanoes. *Contributions to Mineralogy and Petrology*, *160*(1), 45–66.

Rollinson, H. (1993). Using geochemical data. Longman, London.

Rudnick, R. L., & Gao, S. (2003). Composition of the continental crust. *Treatise on Geochemistry*, *3*, 659.

Sato, T., Miyazaki, T., Tamura Y., Gill, J. B., Jutzeler, M., Senda, R., & Kimura, J.-I., in prep. The

    earliest stage of Izu rear arc volcanism revealed by drilling at Site U1437, IODP Expedition 350.

    Submitted to *Geochemistry, Geophysics, Geosystems.*

Schindlbeck, J. C., Kutterolf, S., Straub, S. M., Andrews, G. D., Wang, K.-L., & Mleneck-Vautravers, M.

    J. (2018). One Million Years tephra record at IODP S ites U1436 and U1437: Insights into

    explosive volcanism from the J apan and Izu arcs. *Island Arc*, e12244.

Schmitt, A. K., Konrad, K., Andrews, G. D. M., Horie, K., Brown, S. R., Koppers, A. A. P., … Tamura,

    Y. (2018). 40Ar/39Ar ages and zircon petrochronology for the rear arc of the Izu-Bonin-Marianas

    intra-oceanic subduction zone. International Geology Review, 60(8), 956–976.

    https://doi.org/10.1080/00206814.2017.1363675

Shaw, D. M. (1970). Trace element fractionation during anatexis. *Geochimica et Cosmochimica*

    Acta, *34*(2), 237–243.

Shukuno, H., Tamura, Y., Tani, K., Chang, Q., Suzuki, T., & Fiske, R. S. (2006). Origin of silicic

    magmas and the compositional gap at Sumisu submarine caldera, Izu–Bonin arc, Japan. *Journal*

    of Volcanology and Geothermal Research, *156*(3), 187–216.

Sisson, T. W., Ratajeski, K., Hankins, W. B., & Glazner, A. F. (2005). Voluminous granitic magmas from

    common basaltic sources. Contributions to Mineralogy and Petrology, 148(6), 635–661.

Sisson, T. W., Salters, V. J. M., & Larson, P. B. (2014). Petrogenesis of Mount Rainier andesite: Magma

    flux and geologic controls on the contrasting differentiation styles at stratovolcanoes of the

    southern Washington Cascades. *GSA Bulletin*, *126*(1–2), 122–144.

    https://doi.org/10.1130/B30852.1

Stern, R. J., Fouch, M. J., & Klemperer, S. L. (2004). An overview of the Izu-Bonin-Mariana subduction factory. Inside the Subduction Factory, 138, 175–222.

Straub, S. M. (2003). The evolution of the Izu Bonin-Mariana volcanic arcs (NW Pacific) in terms of major element chemistry. *Geochemistry, Geophysics, Geosystems*, *4*(2).

Straub, S. M. (2008). Uniform processes of melt differentiation in the central Izu Bonin volcanic arc (NW Pacific). *Geological Society, London, Special Publications*, *304*(1), 261–283.

Straub, S. M., A. B. LaGatta, A. L. Martin-Del Pozzo, and C. H. Langmuir. (2008). Evidence from high-Ni olivines for a hybridized peridotite/pyroxenite source for orogenic andesites from the central Mexican Volcanic Belt. *Geochemistry Geophysics. Geosystems*, 9.

Straub, S. M., Goldstein, S. L., Class, C., Schmidt, A., & Gomez-Tuena, A. (2010). Slab and mantle controls on the Sr–Nd–Pb–Hf isotope evolution of the post 42 Ma Izu–Bonin volcanic arc. *Journal of Petrology*, *51*(5), 993–1026.

Suyehiro, K., Takahashi, N., Ariie, Y., Yokoi, Y., Hino, R., Shinohara, M., … Taira, A. (1996). Continental crust, crustal underplating, and low-Q upper mantle beneath an oceanic island arc. *Science*, *272*(5260), 390–392.

Taira, A., Saito, S., Aoike, K. A. N., Morita, S., Tokuyama, H., Suyehiro, K., … Naka, J. (1998). Nature and growth rate of the Northern Izu–Bonin (Ogasawara) arc crust and their implications for continental crust formation. *Island Arc*, *7*(3), 395–407.

Tamura, Y., & Tatsumi, Y. (2002). Remelting of an andesitic crust as a possible origin for rhyolitic magma in oceanic arcs: an example from the Izu–Bonin arc. *Journal of Petrology*, *43*(6), 1029–1047.

Tamura, Y., Tatsumi, Y., Zhao, D., Kido, Y., & Shukuno, H. (2002). Hot fingers in the mantle wedge: new insights into magma genesis in subduction zones. *Earth and Planetary Science Letters*, *197*(1–2), 105–116.

Tamura, Y., Tani, K., Chang, Q., Shukuno, H., Kawabata, H., Ishizuka, O., & Fiske, R. S. (2007). Wet and dry basalt magma evolution at Torishima Volcano, Izu–Bonin Arc, Japan: the possible role of phengite in the downgoing Slab. *Journal of Petrology*, *48*(10), 1999–2031.

Tamura, Y., Gill, J. B., Tollstrup, D., Kawabata, H., Shukuno, H., Chang, Q., … Kodaira, S. (2009). Silicic magmas in the Izu–Bonin oceanic arc and implications for crustal evolution. *Journal of Petrology*, *50*(4), 685–723.

Tamura, Y., Barker, A. K., Busby, C. J., Berger, J. L. R., Blum, P., Bongiolo, E. M., … Yang, Y. (2014). *Izu-Bonin-Mariana Rear Arc - The missing half of the subduction factory, 30 March – 30 May 2014*(Report). https://doi.org/Tamura, Y., Barker, A. K., Busby, C. J., Berger, J. L. R., Blum, P., Bongiolo, E. M., Guèrin, G., Bordiga, M., Andrews, G. D. M., DeBari, S. M., Gill, J. B. , Kars, M. A. C., Hamelin, C., Kita, Z. A., Jia, Jihui, Konrad, K., John, E. H., Mahony, S. H., Jonas, A.-S., Martini, M., Jutzeler, M., Miyazaki, T., Musgrave, R. J., Schindlbeck, J. C. , Nascimento, N. B., Schmitt, A. K., Nichols, A. R. L., Straub, S. M., Ribeiro, J. M., Vautravers, M. J., Sato, T. and Yang, Yang and IODP Expedition 350 (2014) Izu-Bonin-Mariana Rear Arc - The missing half of the subduction factory, 30 March – 30 May 2014.   .   IODP Preliminary Report, 350 . , 172 pp.   DOI 10.14379/iodp.pr.350.2014 <http://dx.doi.org/10.14379/iodp.pr.350.2014>.

Tani, K., Fiske, R. S., Tamura, Y., Kido, Y., Naka, J., Shukuno, H., & Takeuchi, R. (2008). Sumisu volcano, Izu-Bonin arc, Japan: site of a silicic caldera-forming eruption from a small open-ocean island. *Bulletin of Volcanology*, *70*(5), 547–562.

Tani, K., Dunkley, D. J., Chang, Q., Nichols, A. R., Shukuno, H., Hirahara, Y., Tatsumi, Y. (2015). Pliocene granodioritic knoll with continental crust affinities discovered in the intra-oceanic Izu–Bonin–Mariana Arc: Syntectonic granitic crust formation during back-arc rifting. *Earth and Planetary Science Letters*, *424*, 84–94.

Tatsumi, Y. (2005). The subduction factory: how it operates in the evolving Earth. *GSA Today*, *15*(7), 4.

Tatsumi, Y., Shukuno, H., Tani, K., Takahashi, N., Kodaira, S., & Kogiso, T. (2008). Structure and growth of the Izu-Bonin-Mariana arc crust: 2. Role of crust-mantle transformation and the transparent Moho in arc crust evolution. *Journal of Geophysical Research: Solid Earth*, *113*(B2).

Tatsumi, Y., Suzuki, T., Ozawa, H., Hirose, K., Hanyu, T., & Ohishi, Y. (2014). Accumulation of 'anti-continent'at the base of the mantle and its recycling in mantle plumes. *Geochimica et Cosmochimica Acta*, *143*, 23–33.

Taylor, R. N., Lapierre, H., Vidal, P., Nesbitt, R. W., & Croudace, I. W. (1992). Igneous geochemistry and petrogenesis of the Izu-Bonin forearc basin.

Tollstrup, D., Gill, J., Kent, A., Prinkey, D., Williams, R., Tamura, Y., & Ishizuka, O. (2010). Across-arc geochemical trends in the Izu-Bonin arc: Contributions from the subducting slab, revisited. *Geochemistry, Geophysics, Geosystems*, *11*(1).

Tuttle, O. F., & Bowen, N. L. (1958). *Origin of granite in the light of experimental studies in the system: NaAlSi3O8*(Vol. 74). Geological Society of America.

Wade, J. A., Plank, T., Stern, R. J., Tollstrup, D. L., Gill, J. B., O'Leary, J. C., … Trusdell, F. (2005). The May 2003 eruption of Anatahan volcano, Mariana Islands: Geochemical evolution of a silicic island-arc volcano. *Journal of Volcanology and Geothermal Research*, *146*(1), 139–170.

Watson, E. B., & Harrison, T. M. (1983). Zircon saturation revisited: temperature and composition effects

    in a variety of crustal magma types. Earth and Planetary Science Letters, 64(2), 295–304.

White, W. M. (2015) Isotope Geochemistry. Hoboken, New Jersey: Wiley-Blackwell.

Wilke, M., & Behrens, H. (1999). The dependence of the partitioning of iron and europium between

    plagioclase and hydrous tonalitic melt on oxygen fugacity. *Contributions to Mineralogy and*

    Petrology, *137*(1–2), 102–114.

Woodhead, J.D., Hergt, J.M., 2001. Strontium, neodymium and lead isotope analyses of NIST glass

    certified reference materials: SRM 610, 612, 614. Geostandards and Geoanalytical Research, 25:

    261-26.

Yamazaki, T., & Yuasa, M. (1998). Possible Miocene rifting of the Izu–Ogasawara (Bonin) arc deduced

    from magnetic anomalies. *Island Arc*, *7*(3), 374–382.

Yuasa, M. (1995). Myojin Knoll, Izu–Ogasawara arc: submersible study of submarine pumice

volcano. *Bulletin of the Volcanology Society of Japan*, *40*, 277–284.
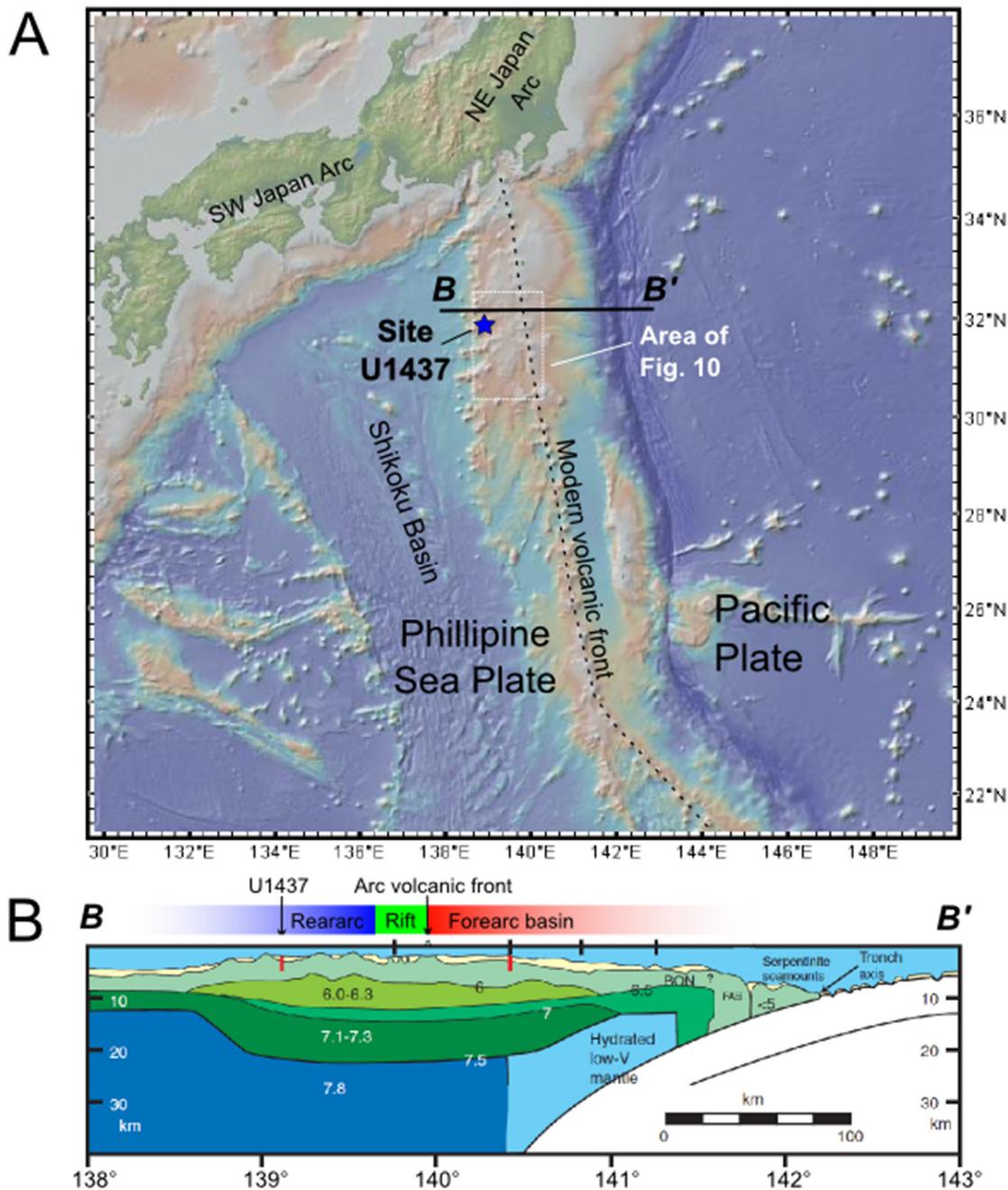
Figure 1: A. The Izu-Bonin-Mariana Arc is an intraoceanic subduction zone located in the Western Pacific Ocean, where the Pacific Plate subducts underneath the Philippine Sea Plate. IODP Site U1437 noted by blue star. Location of cross section is denoted by line B-B'. The area depicted in Figure 10 is denoted by the white box. Map created using GeoMapApp.
B. Schematic cross section of the Izu-Bonin at latitude 32°15'N modified after Tamura et al., 2014 and Suyehiro et al., 1996. Within the cross section, different colors denote different layers with seismic velocities in km/s from Suyehiro et al., 1996, with crustal layers denoted in greens and mantle layers denoted in blues. The crust contains a thick 6-6.3 km/s low-velocity layer which is interpreted as a thick intermediate to felsic midcrust and is thought to represent the unsubductable nucleus of continental crust (Leat and Larter, 2003). Above the cross section, the labeled colored bar shows the different geomorphic provinces of the Izu-Bonin arc. Rear-arc, by the definition used in this study, includes the region to the west of the <1 Ma rift depression.
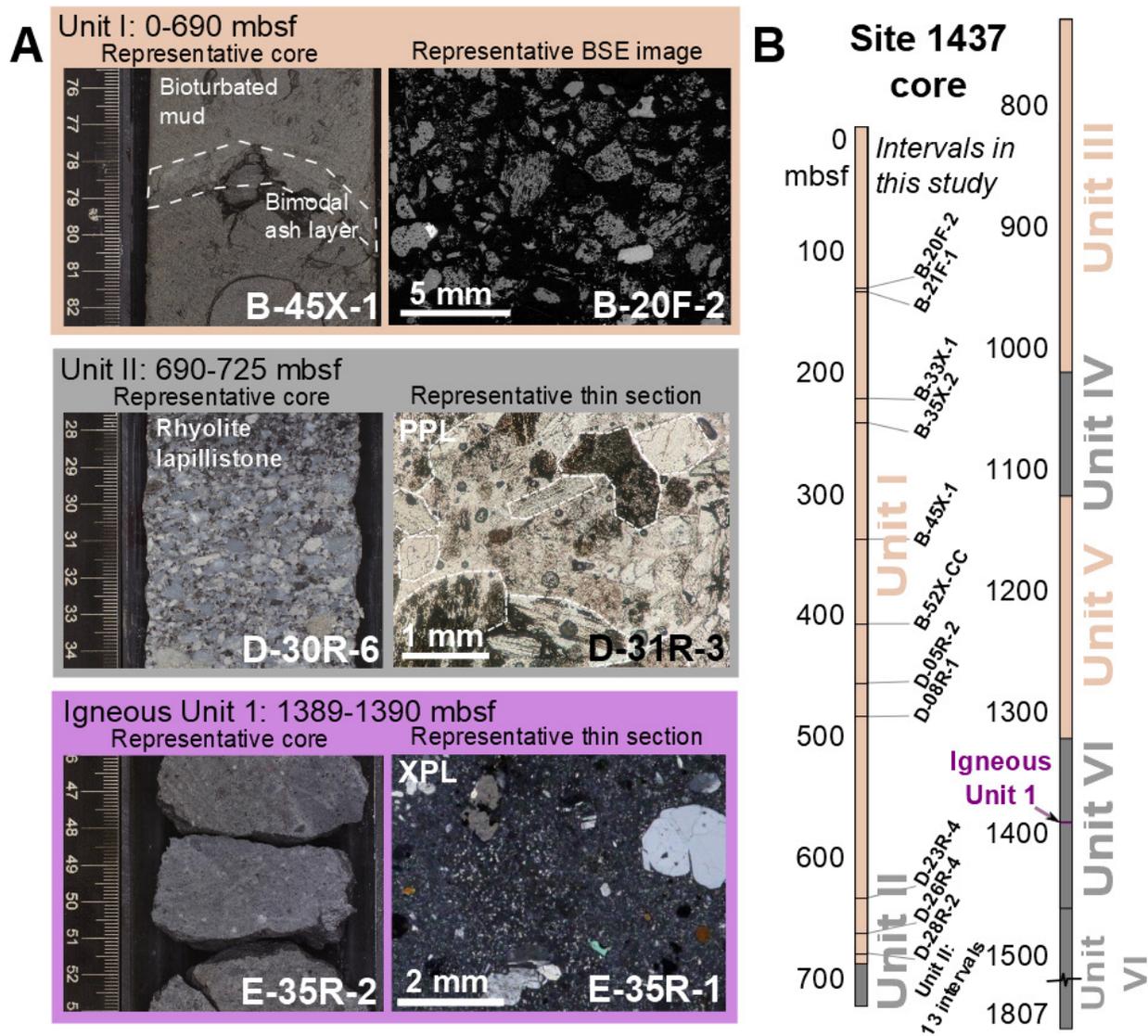
Figure 2: A. Representative core and microscopic images of intervals used in this study. Unit I backscatter-electron (BSE) image is taken on a grain mount with mud fraction removed. Unit II photomicrograph shows individual glass lapilli highlighted in white. B. Schematic diagram of the Site U1437 core showing depths of lithostratigraphic units and samples used in this study. On the core, tan colors denote units where tuffaceous mud/mudstone is the dominant lithology and grey colors denote units dominated by coarser volcaniclastic material. The location of Igneous Unit 1 is located in purple.
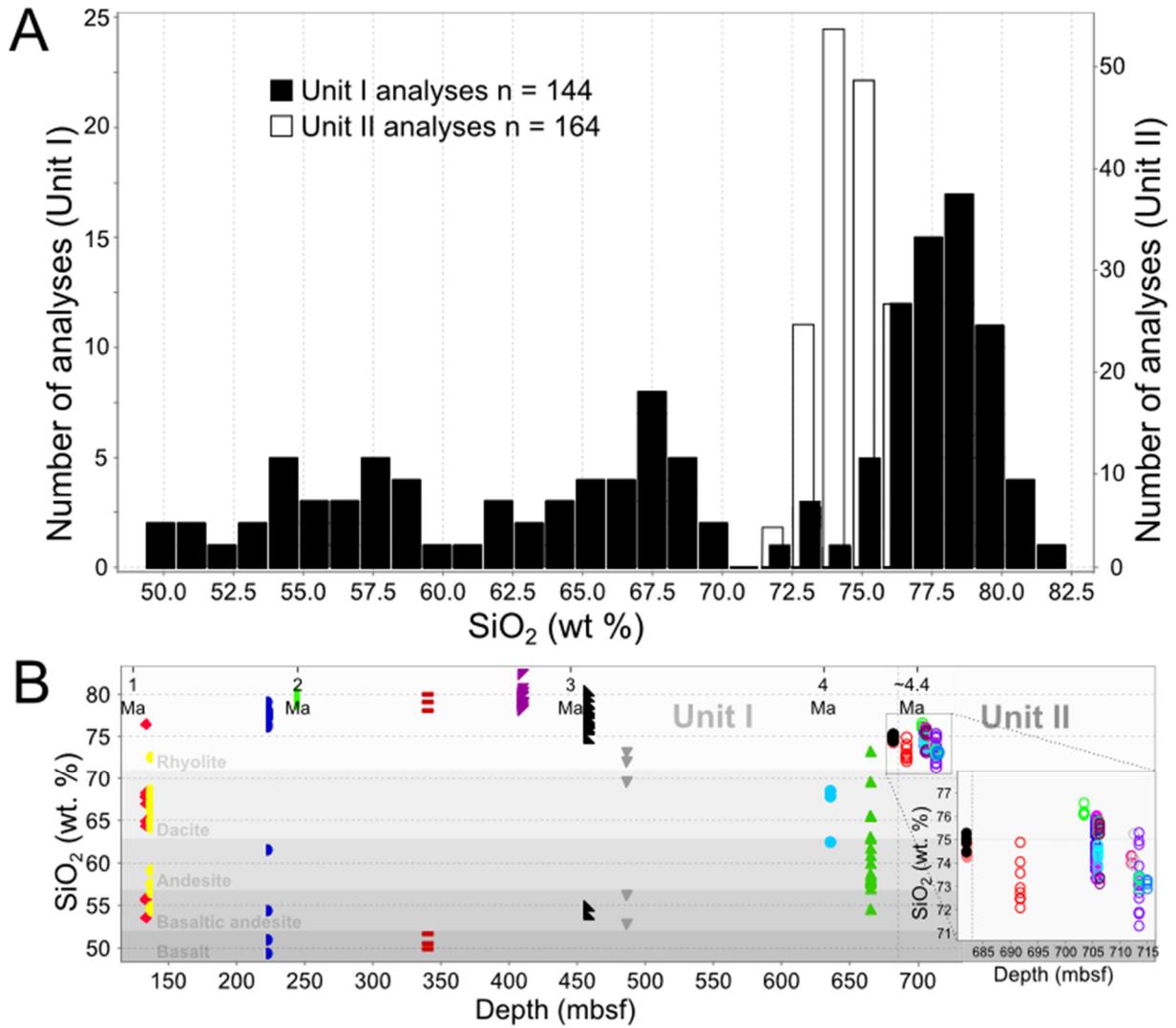
Figure 3: A. Histogram of SiO$_2$ compositions of glass shards considered in this study. All wt. % oxides are shown on a 100% normalized anhydrous basis. Unit I contains a variety of compositions, whereas Unit II contains only rhyolitic glass. B. SiO$_2$ of intervals shown plotted against depth and age of interval (using age model after Tamura et al., 2014). Unit I is dated to 0-4.4 Ma and Unit II is ~4.4 Ma. Different intervals are shown in different colors and symbol shapes, with open symbols representing Unit II. IUGS names are indicated by shades of grey on the background.
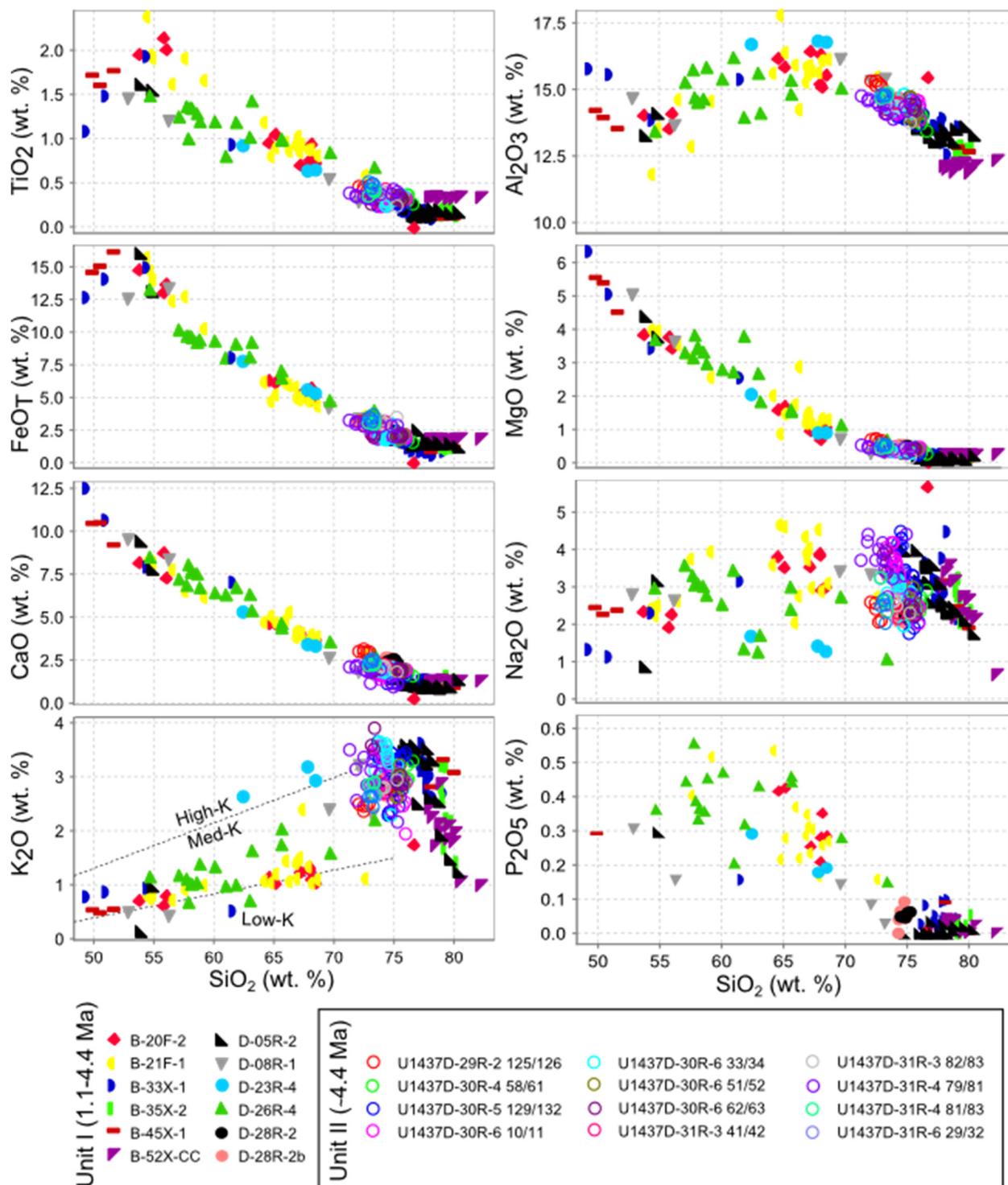
Figure 4: Harker diagrams of glass shard major element compositions as measured via electron microprobe, with different intervals denoted by different colors/shapes (as in Figure 3). Open symbols represent glass from Unit II rhyolitic tephras. All wt. % oxides are shown on 100% normalized anhydrous basis. K_2O series boundaries are from Gill, 1981. The two youngest intervals (B-20-F-2 and B-21F-1) have slightly lower K_2O than older glasses of similar SiO_2.

63
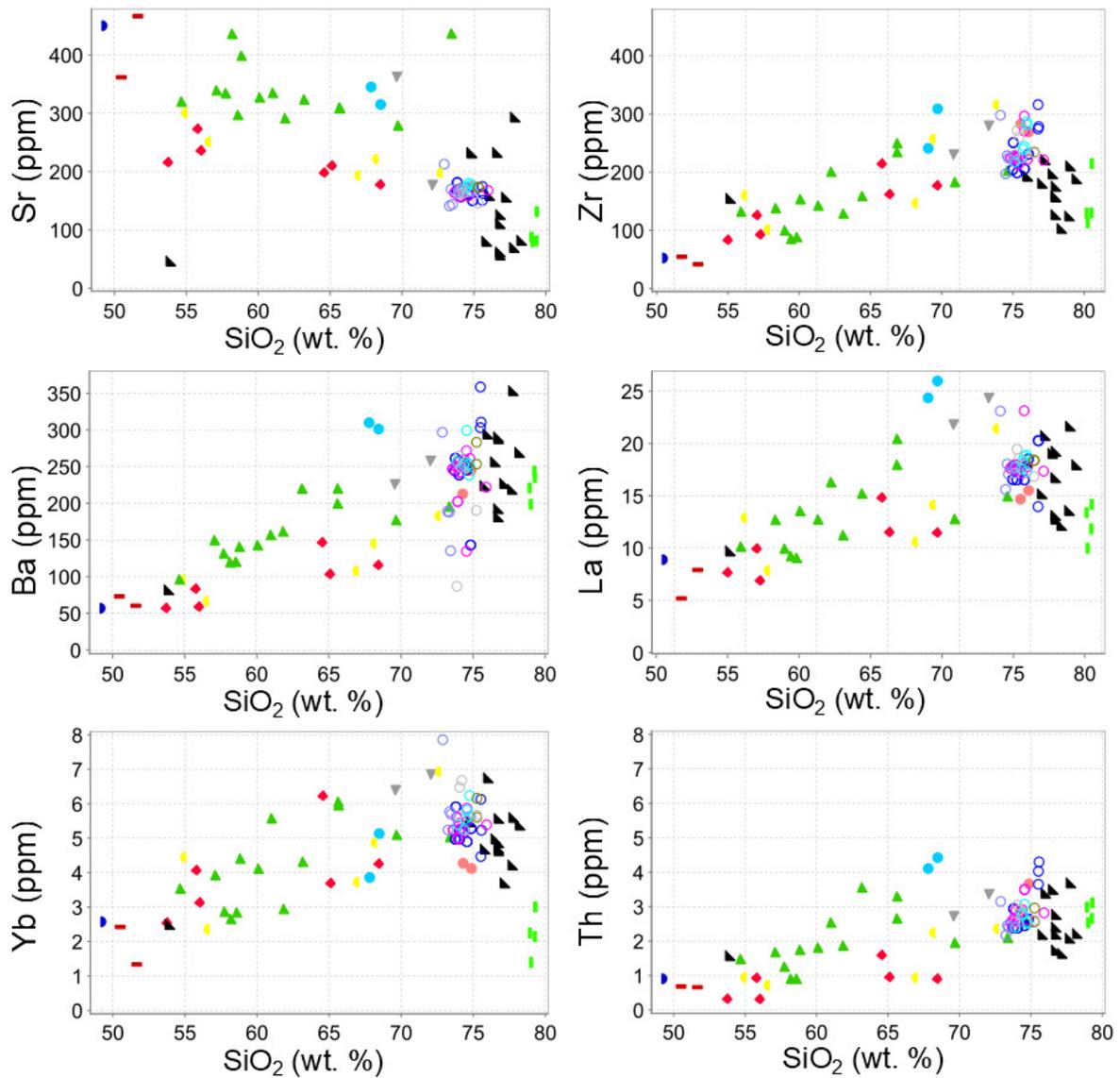
Figure 5: Trace elements in ppm obtained via LA-ICP-MS of glass shards. Color and symbols represent different intervals, as in Figure 4. Open symbols represent Unit II rhyolitic glass. The two youngest intervals (B-20F-2 and B-21F-1, ~1.1 Ma) have slightly lower-K (see figure 4) and deviate off trace element trends formed by glass analyses in intervals aged 1.7 to 4.4 Ma.
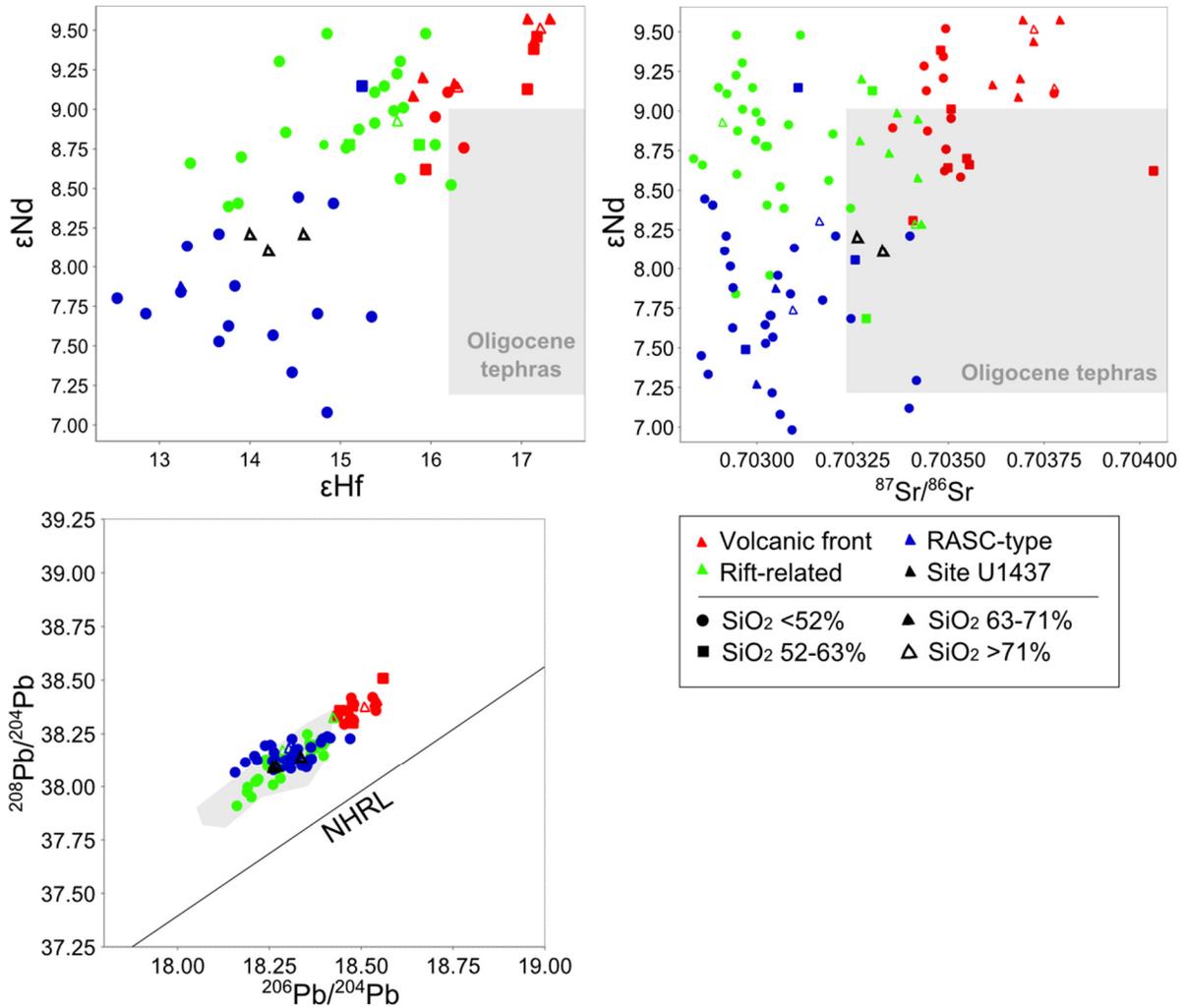
Figure 6: Sr-Nd-Hf-Pb isotope systematics of three Unit II rhyolitic tephras from Site U1437 (black open triangles). Different colors represent the three different across-arc regions of the Izu-Bonin arc (red representing volcanic front, green representing the <1 Ma rift, and blues representing <7 Ma samples with rear-arc seamount chain-type (RASC-type) signature), with symbol shape representing dredge SiO_2. The range of isotopic values found in Eocene-Oligocene tephras is denoted by the grey field, representing modern-day isotopes measured on Eocene-Oligocene tephras collected in the Izu-Bonin fore-arc (Straub et al., 2010); relevance of Eocene-Oligocene tephras is discussed later in the text. NHRL is the Northern Hemisphere Reference Line (Hart, 1984). Epsilon Hf and Nd using chondritic uniform reservoir values (CHUR) from Bouvier et al., 2008. Data sources for samples other than Unit II and Eocene-Oligocene tephra are: Fiske, 2001; Gill et al., 1994; Haraguchi et al., 2017; Hochstaedter et al., 1990a; Hochstaedter et al., 1990b; Hochstaedter et al., 2000; Hochstaedter et al., 2001; Ikeda and Yasua, 1989; Ishizuka et al., 2002; Ishizuka et al., 2003; Ishizuka et al., 2007; Jordan et al., 2011; Machida et al., 2008; Ossaka et al., 1990; Shukuno et al., 2006; Tamura et al., 2007; Tamura et al., 2009 and references therein; Tani et al., 2008; Yuasa, 1995.
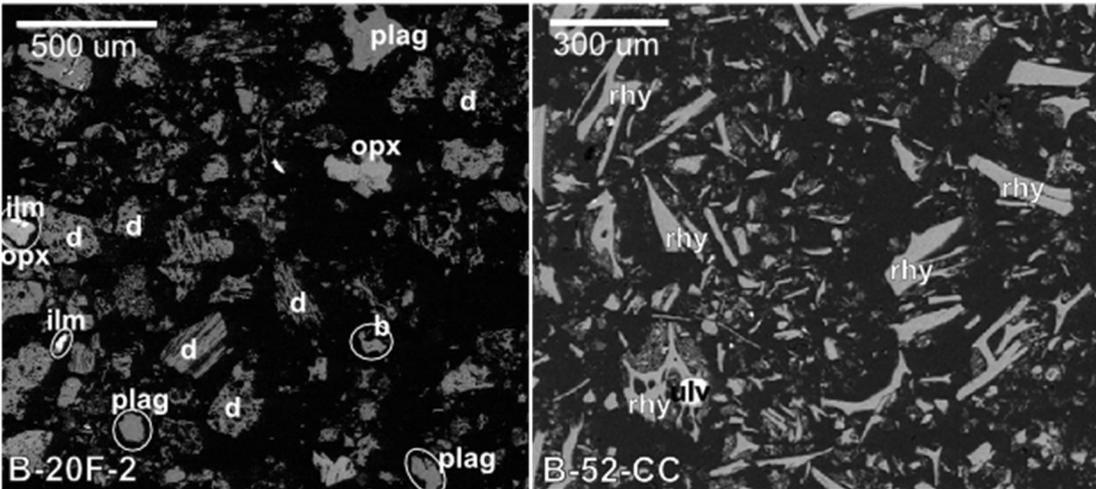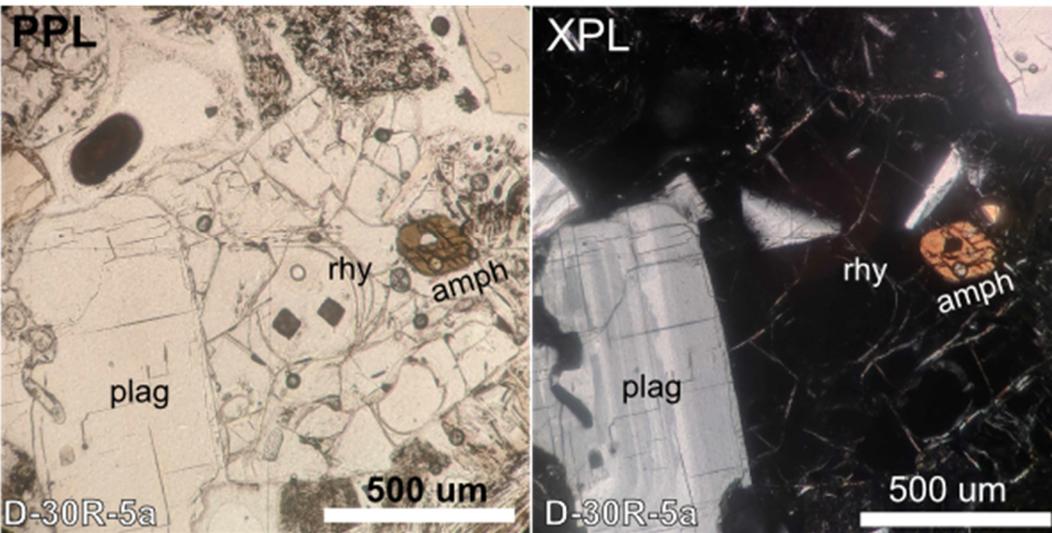
Figure 7: Microscopic images of typical Unit I and Unit II intervals. A. Representative Unit I intervals (SEM-BSE image of B-20F-2 and B-52-CC grain mounts) with angular glass shards and broken, angular anhedral phenocrysts. B. Representative Unit II interval (photomicrograph of D-30R-5a thin section) containing hypocrystalline lapilli with subhedral to euhedral phenocrysts in a glassy groundmass. Abbreviations are: b = basalt glass, d = dacite glass, rhy = rhyolite glass, opx = orthopyroxene, plag = plagioclase, amph = amphibole, ilm = ilmenite, ulv = ulvospinel.
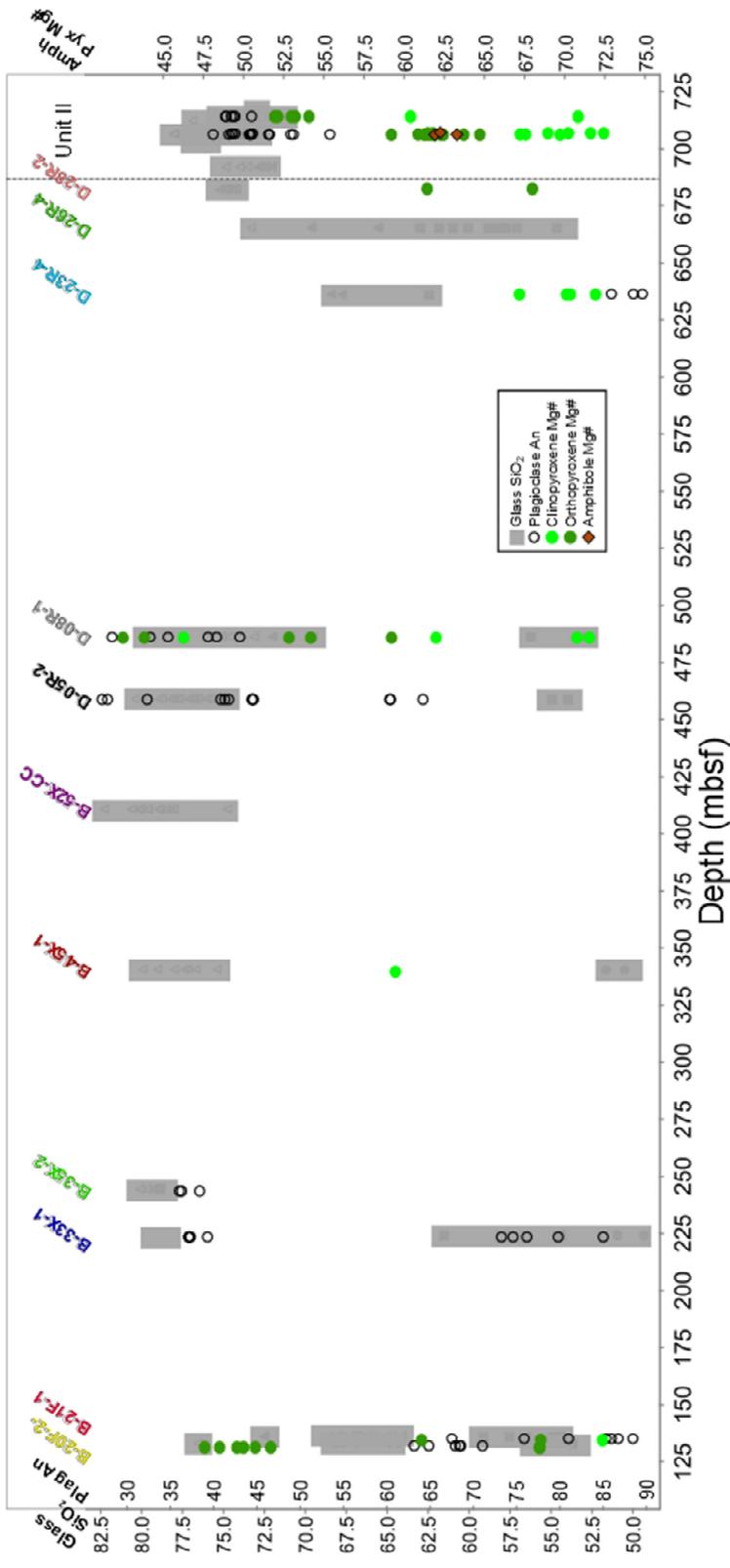
Figure 8: Diagram showing compositions of glass (grey boxes) and phenocrysts (symbols) from Unit I and II tephras with tephra depth plotted as the x-axis. Phenocryst mineral compositions are plotted overtop glass compositions: amphibole and pyroxene mineral compositions are represented by Mg# (Mg / [Mg+ Fe]) (see y-axis on right) and plagioclase composition is represented by % anorthite component (see y-axis on left).
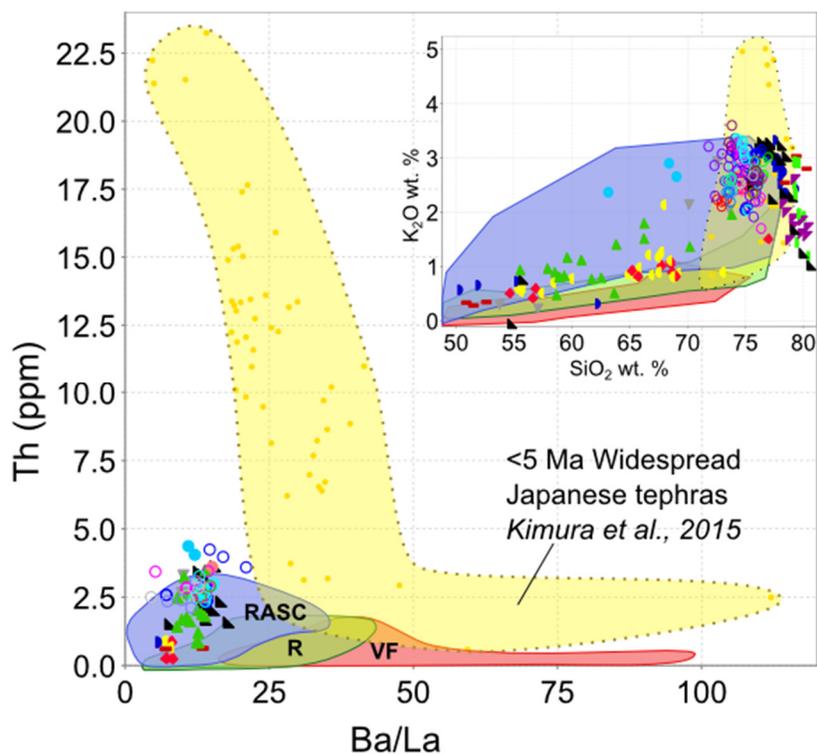
Figure 9: Bivariate diagram showing Th (ppm) plotted against Ba/La with inset of K_2O Harker diagram. The four colored fields represent glass or whole rock compositions from the three across-arc regions of the Izu-Bonin arc (VF = volcanic front, R = rift-related, RASC = rear-arc seamount chain-type) and widespread tephras originating in Japanese subduction zones (yellow) from Kimura et al., 2015. Site U1437 glass compositions are shown in colors/shapes representing different intervals from this study, as in figure 4. Japanese tephras have overlapping major element compositions with glass compositions in this study, but trace element systematics show that Japanese sources are not represented in Site U1437 tephras considered in this study. Site U1437 tephras (this study) and Japanese tephras (Kimura et al., 2015) are EMP/LA-ICP-MS performed on glass shards, and Izu-Bonin literature samples (closed circles) are mainly XRF/ICP-MS performed on whole-rock samples (data sources listed in figure 6).
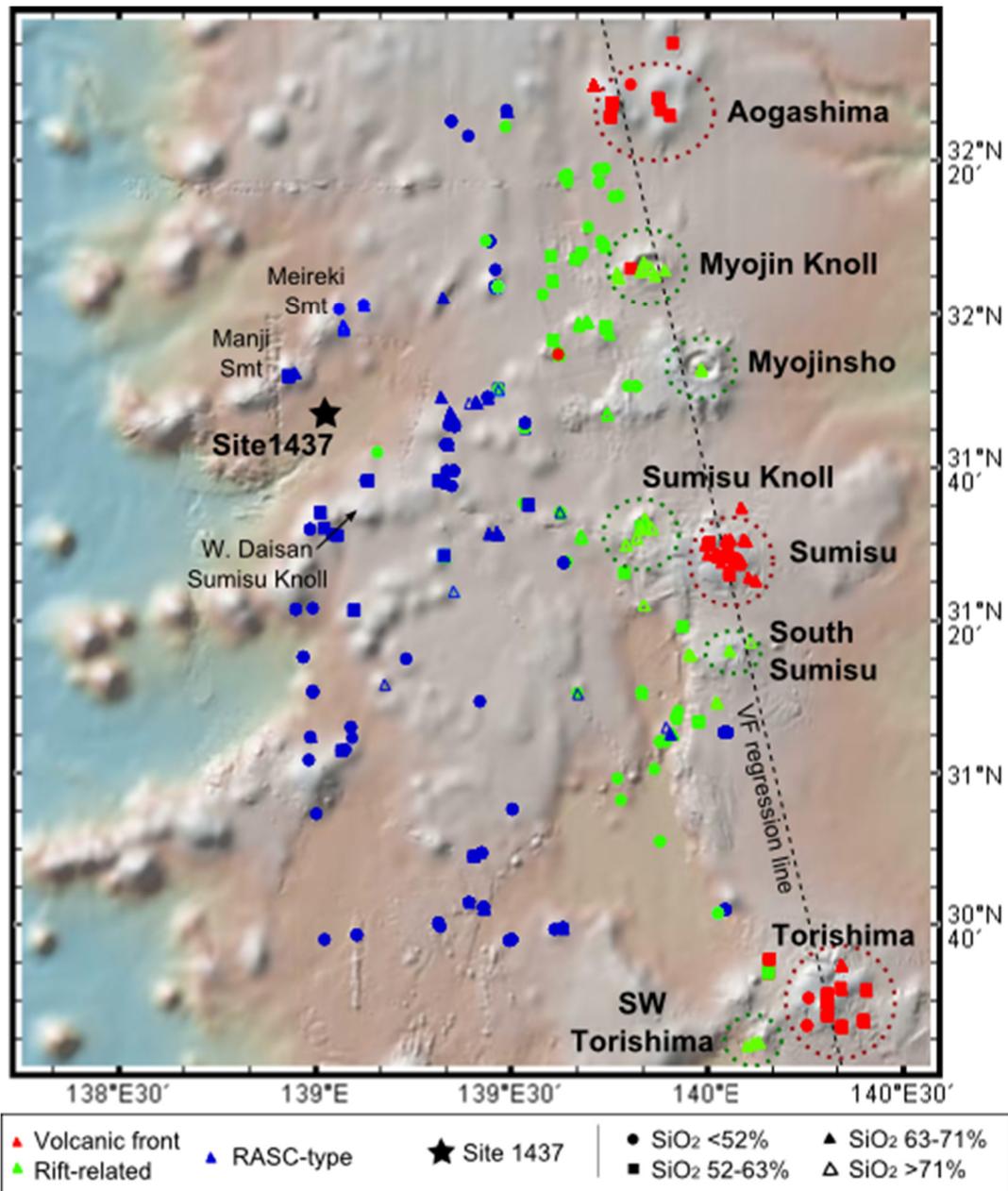
Figure 10: Map showing the location of dredged rocks from the Izu-Bonin, overlain on a DEM of bathymetry. Color of point corresponds to the three different geochemical signatures present in <7 Ma dredge rocks: red is volcanic front signature, green is rift-related signature, and blues are rear-arc seamount chain-type (RASC-type) signature; symbol shapes represent the SiO_2 of rocks dredged in this location. Site U1437 is denoted by a black star. The major modern eruptive centers are circled and labeled, with R1 basalt-dominated centers circled in red, and R2 rhyolite-dominated centers circled in green (after Tamura et al., 2009). Data sources are indicated in figure 6. Volcanic front regression line used to calculate distance to volcanic front is shown as the black dotted line. Figure made using GeoMapApp.
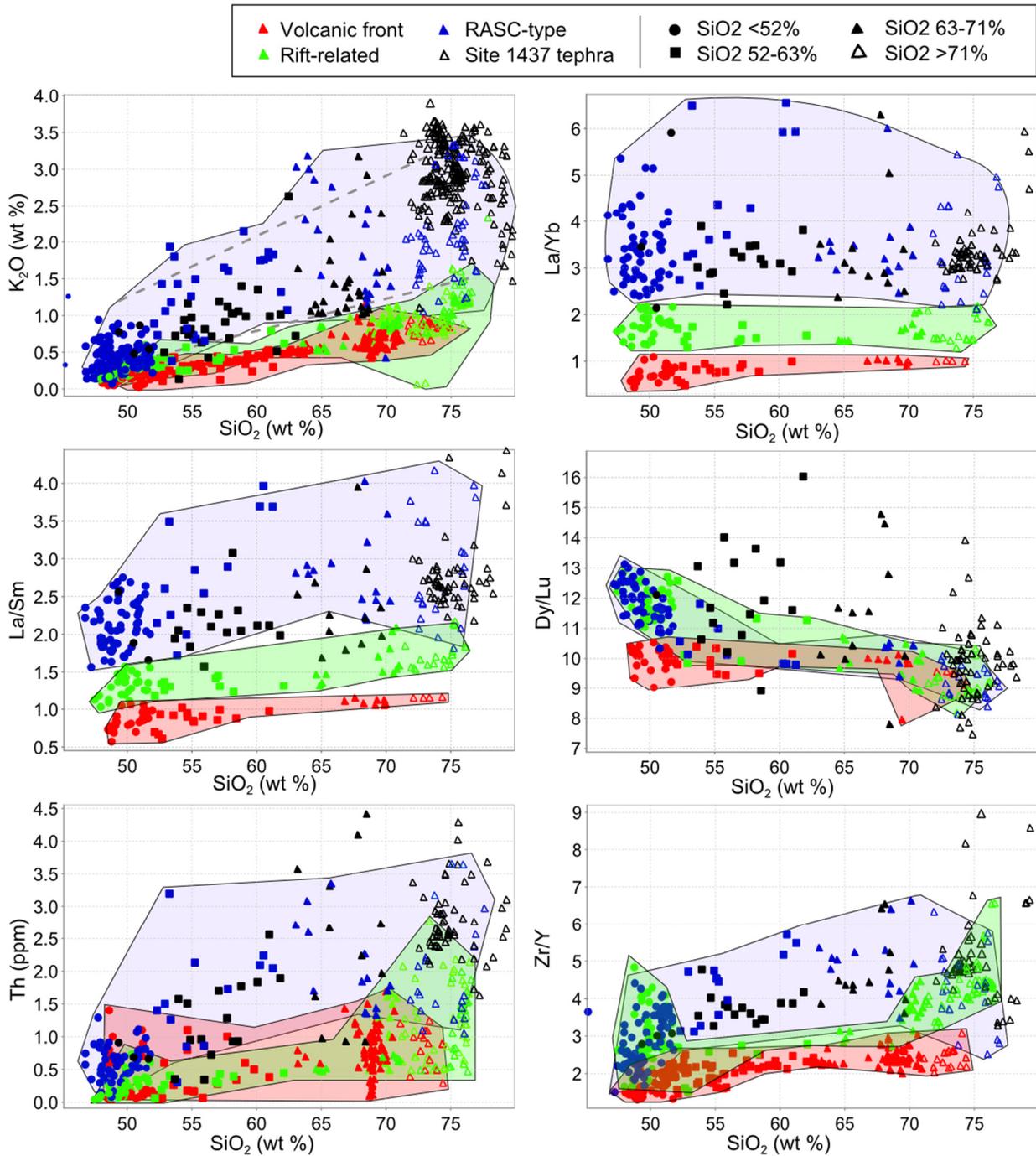
Figure 11: Major and trace elements of Izu-Bonin regional dredges (red, green and blue symbols) and Site U1437 tephras (black symbols). Shading colors represent across-arc region and symbol shapes represent SiO2 content (as in figures 6 and 10). Literature data from dredged samples, as in figure 10, are generally whole-rock analyses via XRF/ICP-MS (data sources in figure 6) and Site U1437 tephra analyses are via glass shard EMP/LA-ICP-MS. Site U1437 tephras show RASC-type signature (e.g. La/Yb over 2.3). K2O series boundaries after Gill, 1981.
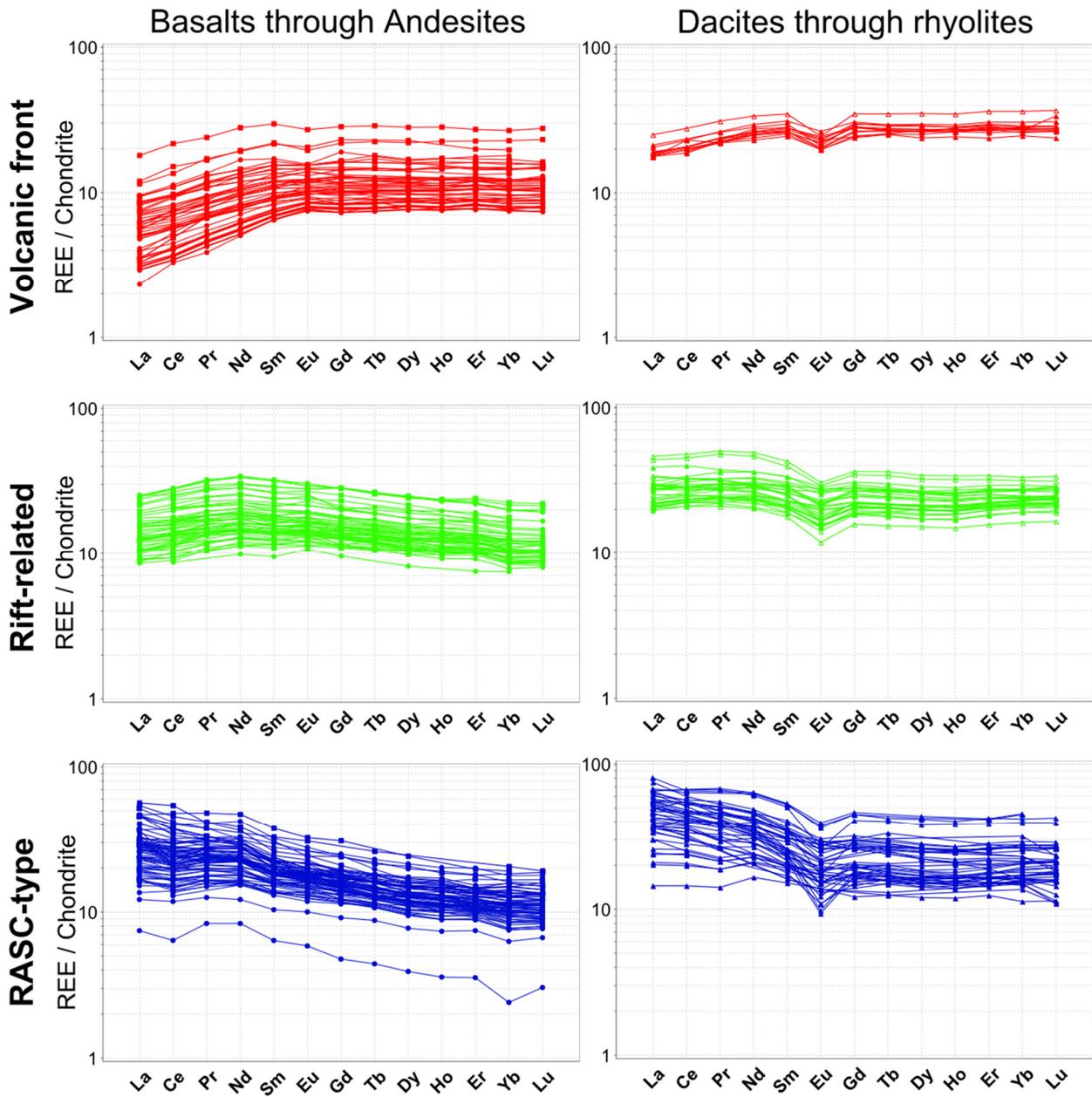
Figure 12: Rare-earth element diagram showing REE patterns of published analyses separated into three across-arc regional signatures characterized by this study. REEs are normalized to C1 chondrites using the values of Sun and McDonough, 1995. Colors and symbol shapes as in figure 6, and basalts through andesites are shown separately from dacites and rhyolites. Western Seamounts samples only include dredges <7 Ma. Data sources listed in text.
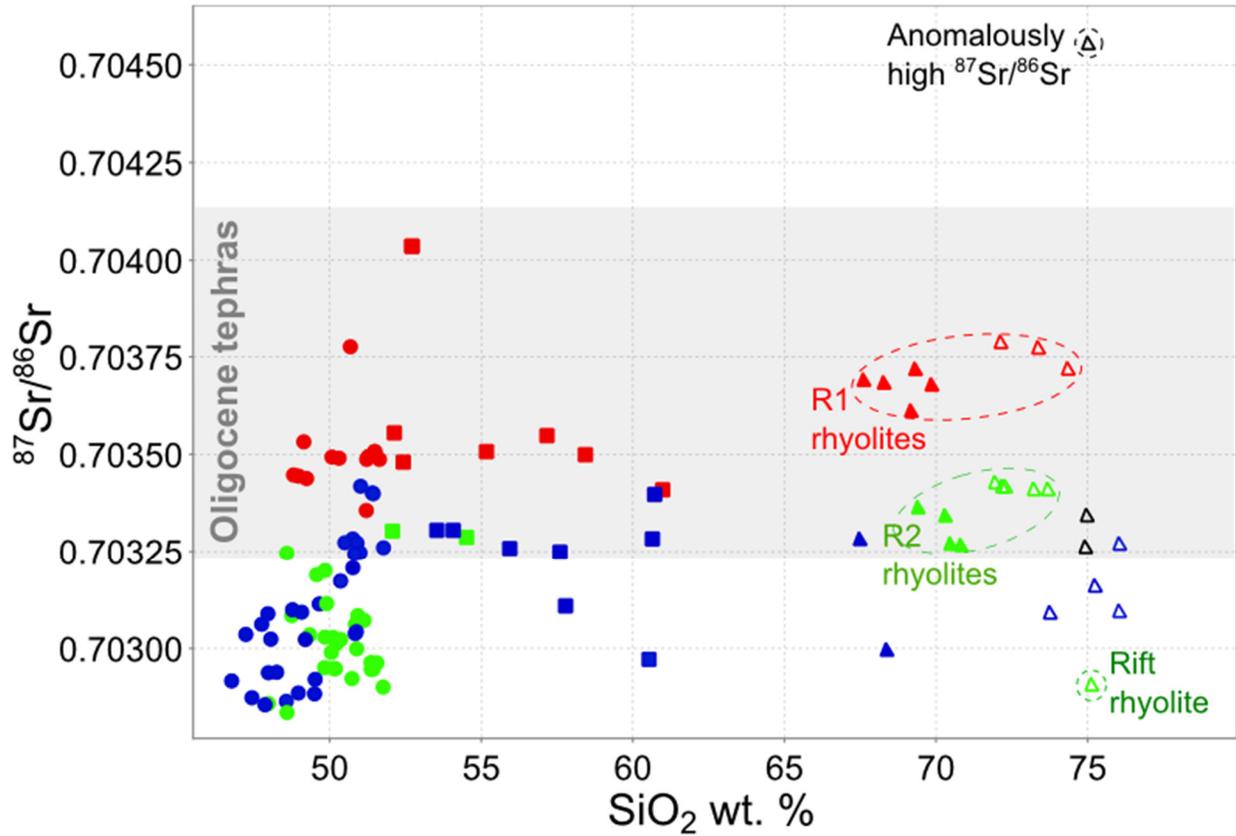
Figure 13: $^{87}Sr/^{86}Sr$ isotope systematics of published dredge samples from the Izu-Bonin compared to three new Sr isotopic analyses on Site U1437 intervals from Unit II rhyolitic tephra (open black triangles). Colors correspond to across-arc region and symbol shapes correspond to SiO_2, as in figures 6. The range of modern $^{87}Sr/^{86}Sr$ values observed in Eocene-Oligocene fore-arc tephras (Straub et al., 2010) is indicated by the grey field. R1 and R2 rhyolites (after Tamura et al., 2009) are circled by dashed lines, as is the only published isotope analysis of a rift signature rhyolite that is not from an R2 rhyolitic center (from Tamura et al., 2009). Other data sources listed in Figure 6. One of the Site U1437 tephra analyses has anomalously high Sr isotopic ratio (higher than all other Izu-Bonin samples) but the other two plot squarely in the RASC-type field.
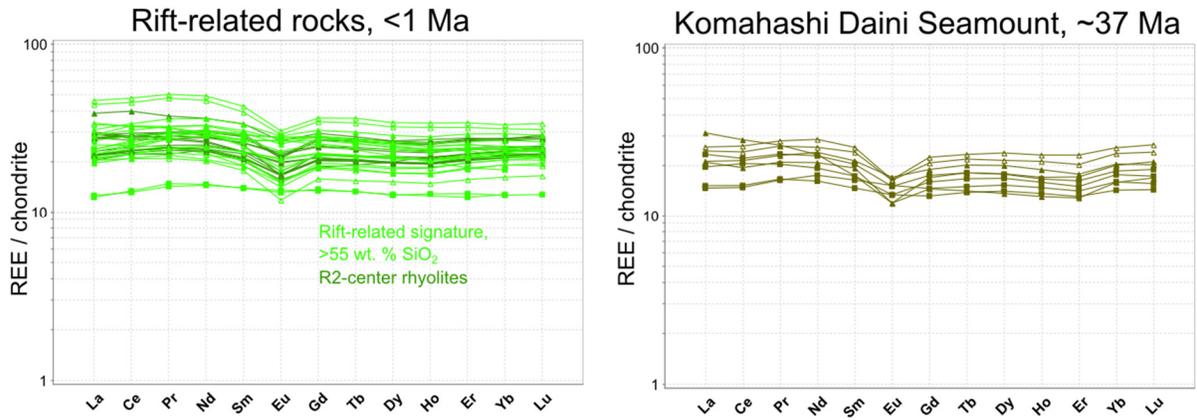
Figure 14: A. REE diagrams showing rift-signature dredged rocks from the modern (<1 Ma) Izu-Bonin rift region and other related rocks; and B. REE patterns from rocks from the Oligocene Komahashi Daini Seamount (KDS; Haraguchi et al., 2003). Note the strikingly similar patterns. Because KDS samples have SiO_2 compositions >55 wt. %, only rift-signature dredged rocks with >55 wt. % SiO_2 are shown. R2-center rhyolites are shown in a slightly darker green than other rift-related rocks, and show overlapping REE patterns. Symbol shapes correspond to SiO_2 as in figure 6 and 10. Data sources listed in figure 6. REE patterns are normalized using C1 chondrite values from Sun and McDonough, 1995.
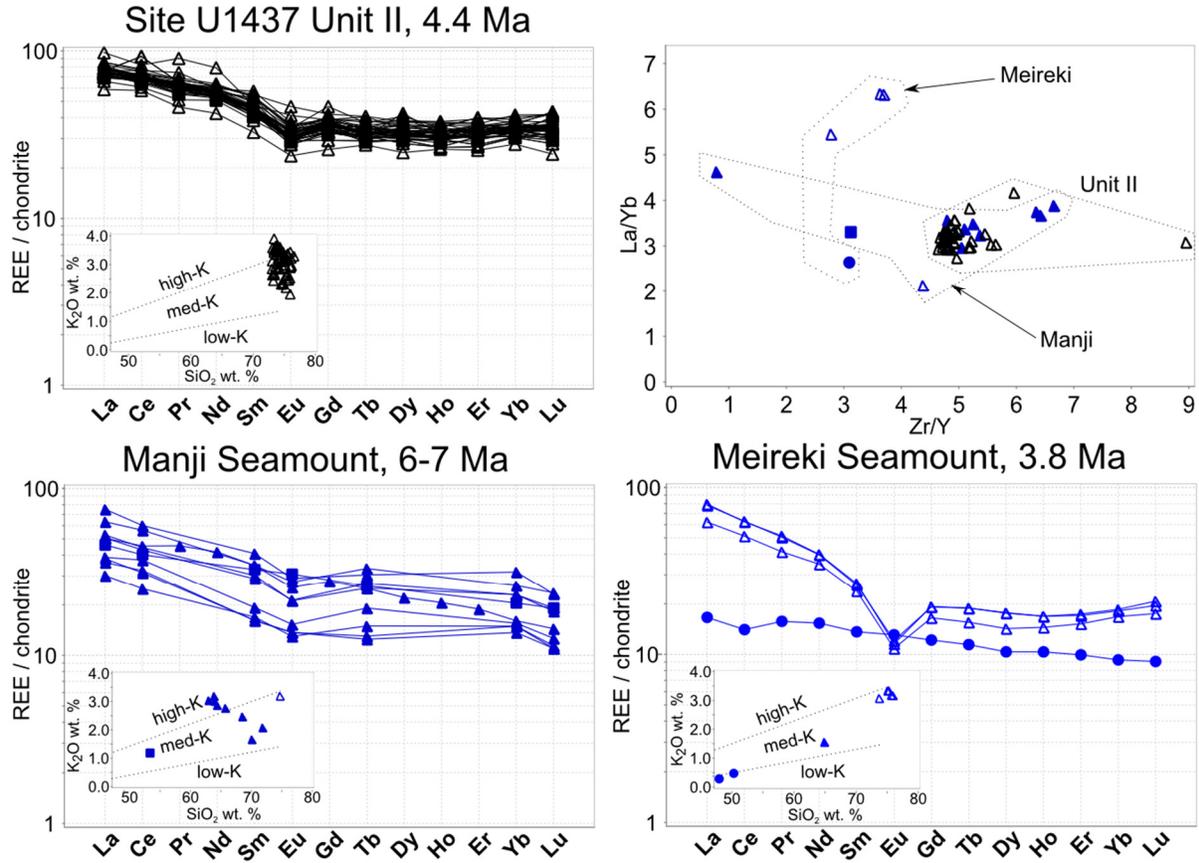
Figure 15: Trace element characteristics of volcaniclastic glasses and volcanic rocks erupted local to Site U1437, with inset K_2O. Rhyolites from Meireki have higher La/Yb in comparison to Unit II rhyolites and Manji rhyolites. Symbol shapes correspond to SiO_2 as in figure 6 and 10. Data is from Hochstaedter et al., 2000, Ishizuka et al., 2002, Tollstrup et al., 2010, and this study. K_2O series boundaries from Gill, 1981. REE patterns are normalized using C1 chondrite values from Sun and McDonough, 1995.
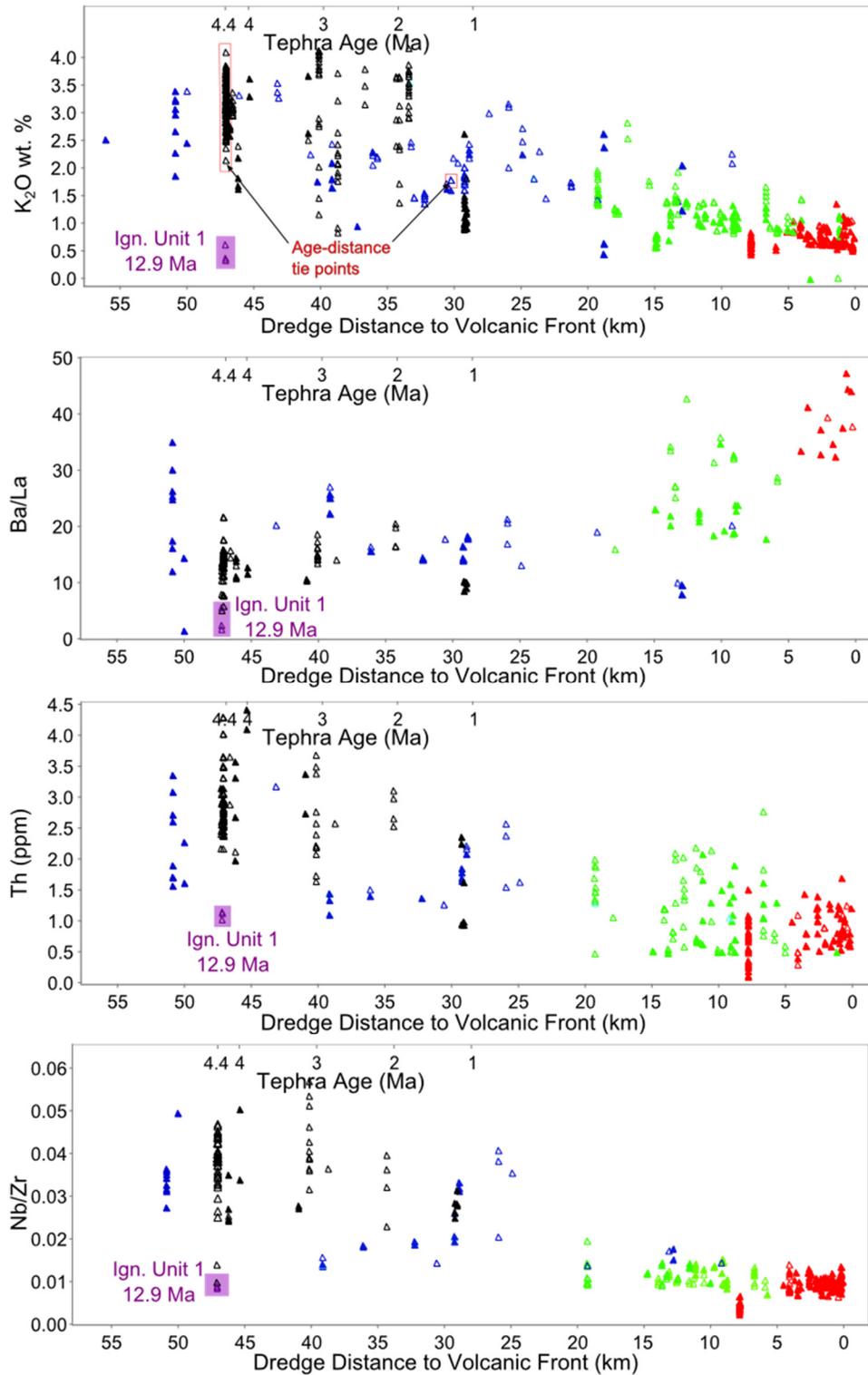
Figure 16: Figure showing evolution of various major and trace elements in Izu Bonin dacites and rhyolites over time and space. Dredge analyses from the literature (data sources as in figure 6) are plotted by distance to volcanic front, and Site U1437 tephra analyses are plotted by their age. Age and distance datasets are interpolated using two points where rocks are well-dated with known eruption location, indicated as the age-distance tie-points. Colors correspond to across-arc region and symbol shapes correspond to SiO_2, as in figure 6, with Site U1437 Igneous Unit 1 rhyolitic sill (12.9 Ma) shown in purple for comparison.

75
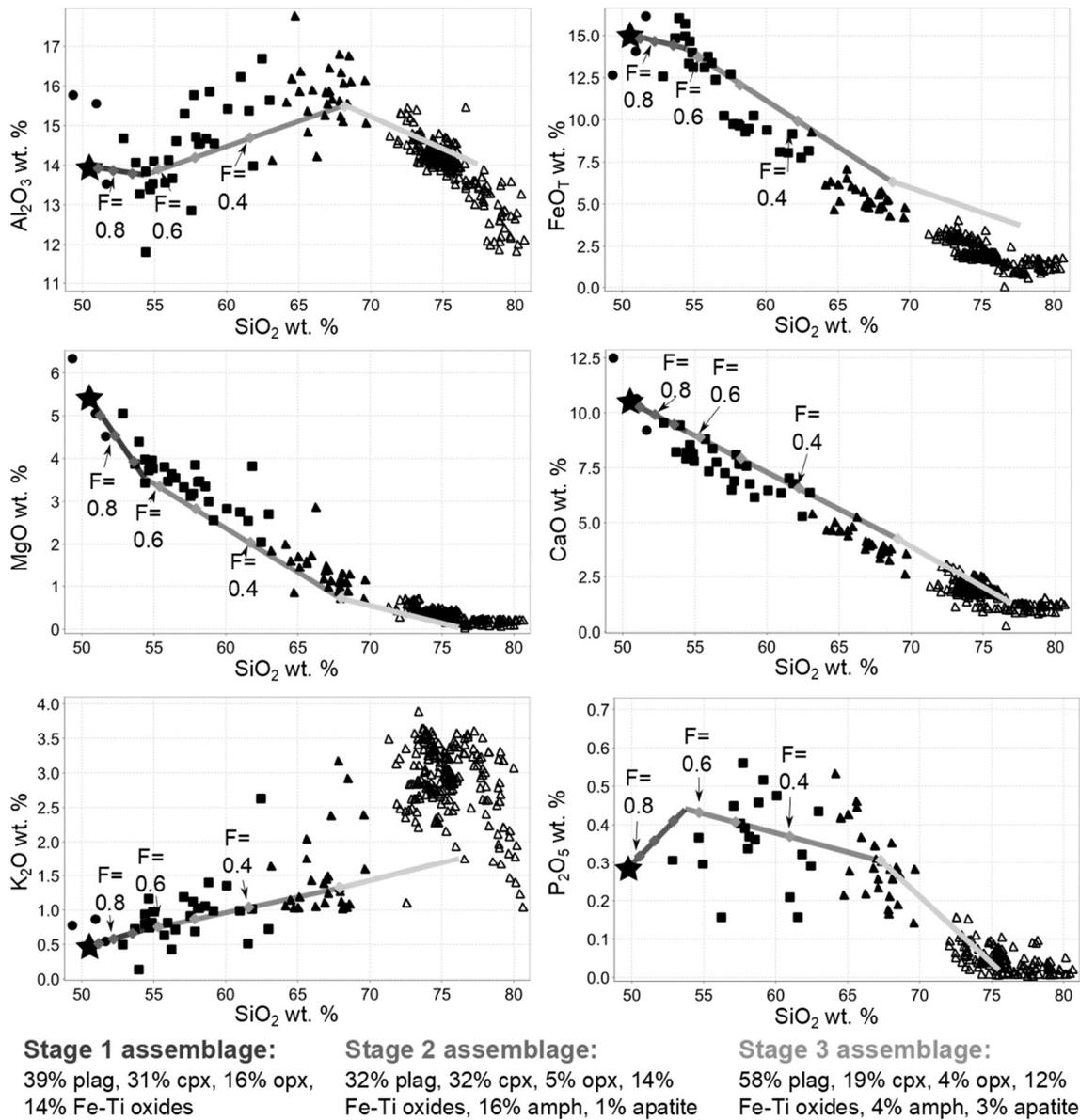
Figure 17: Major element subtraction modeling compared to Site U1437 glass analyses. Starting composition (B-45X-1_glass1) is shown by a black star. There are three different fractionating assemblages: Stage 1 assemblage fractionated from F = 1.0-0.65, Stage 2 assemblage fractionated from F = 0.65-0.30, Stage 3 assemblage fractionated from F = 0.3-0.23. Symbol shapes represent SiO_2, as in Figure 6.
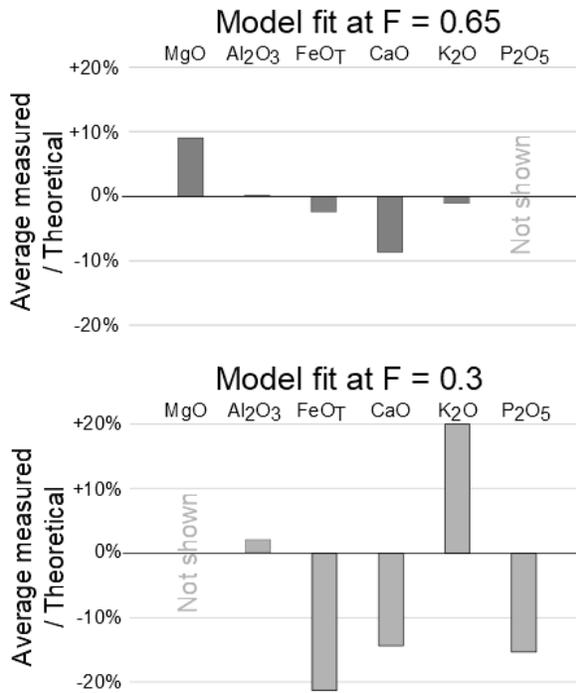
Figure 18: Comparison of modeled liquid to observed site U1437 glasses, at modeled F = 0.65 and F = 0.30. Oxide values of modeled liquids were compared to the average of glass oxide values within a SiO_2 range of 2.5 wt. %. Error was not evaluated for TiO_2, MnO or Na_2O, and not shown when error was smaller than EMP instrument error.
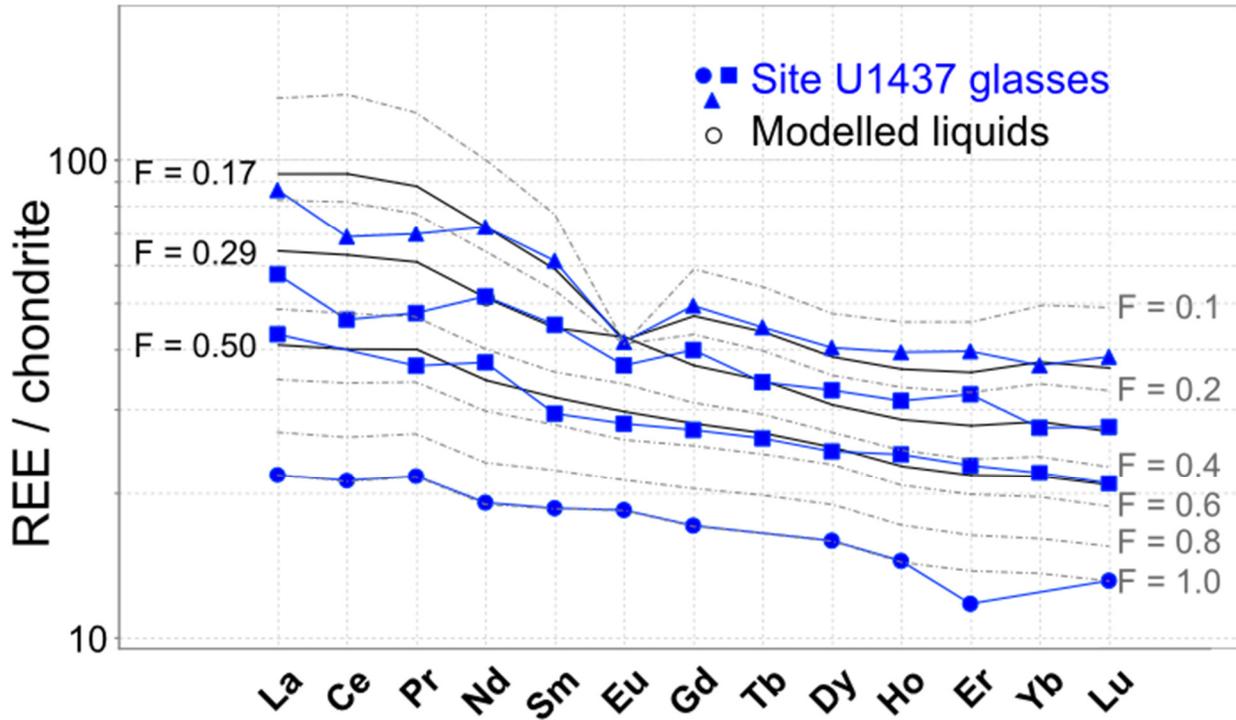
Figure 19: Rare-earth element modeling (black dashed lines) compared to Site U1437 glass REEs. Starting composition (interpolated from B-45X-1_glass1) is shown by F = 1.0. Specific modeling results at F = 0.50, F = 0.29, and F = 0.17 are highlighted with solid black lines. There are three different fractionating assemblages, as shown in Figure 17: Stage 1 assemblage fractionated from F = 1.0-0.65, Stage 2 assemblage fractionated from F = 0.65-0.30, Stage 3 assemblage fractionated from F = 0.3-0.1. Modelled liquids closely match measured liquids but do not duplicate the negative Ce anomaly present in some glasses. Symbol shapes represent SiO_2, as in Figure 6.
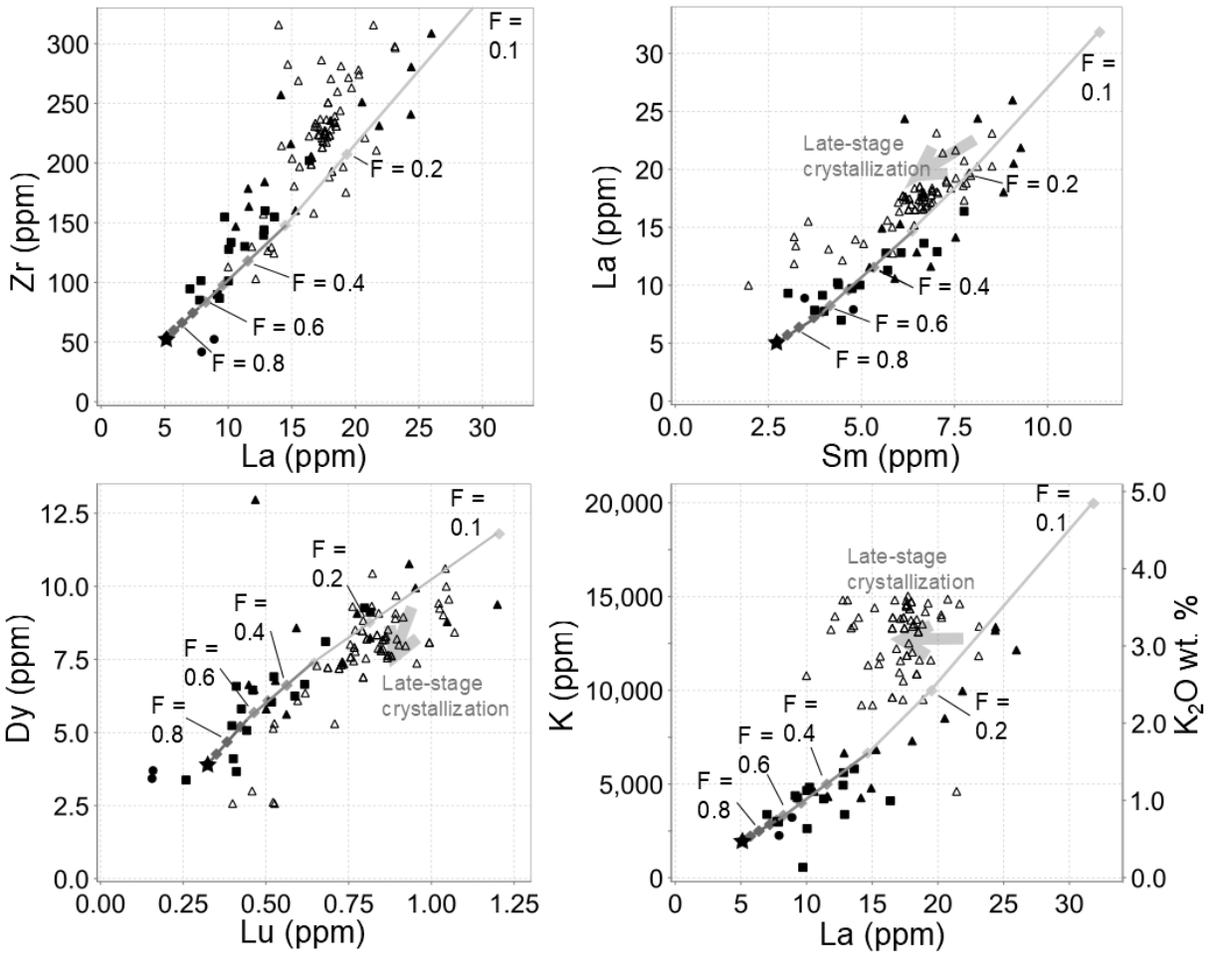
Figure 20: Trace element modeling compared to Site U1437 glasses. Starting composition (B-45X-1_glass1) is shown by the black star. There are three different fractionating assemblages, as shown in Figure 17: Stage 1 assemblage fractionated from F = 1.0-0.65, Stage 2 assemblage fractionated from F = 0.65-0.30, Stage 3 assemblage fractionated from F = 0.3-0.1. Late stage fractionation (above 73 wt. % SiO_2, where REEs no longer behave incompatibly) was not modeled but is indicated schematically by grey arrows. Symbol shapes represent SiO_2, as in Figure 6.
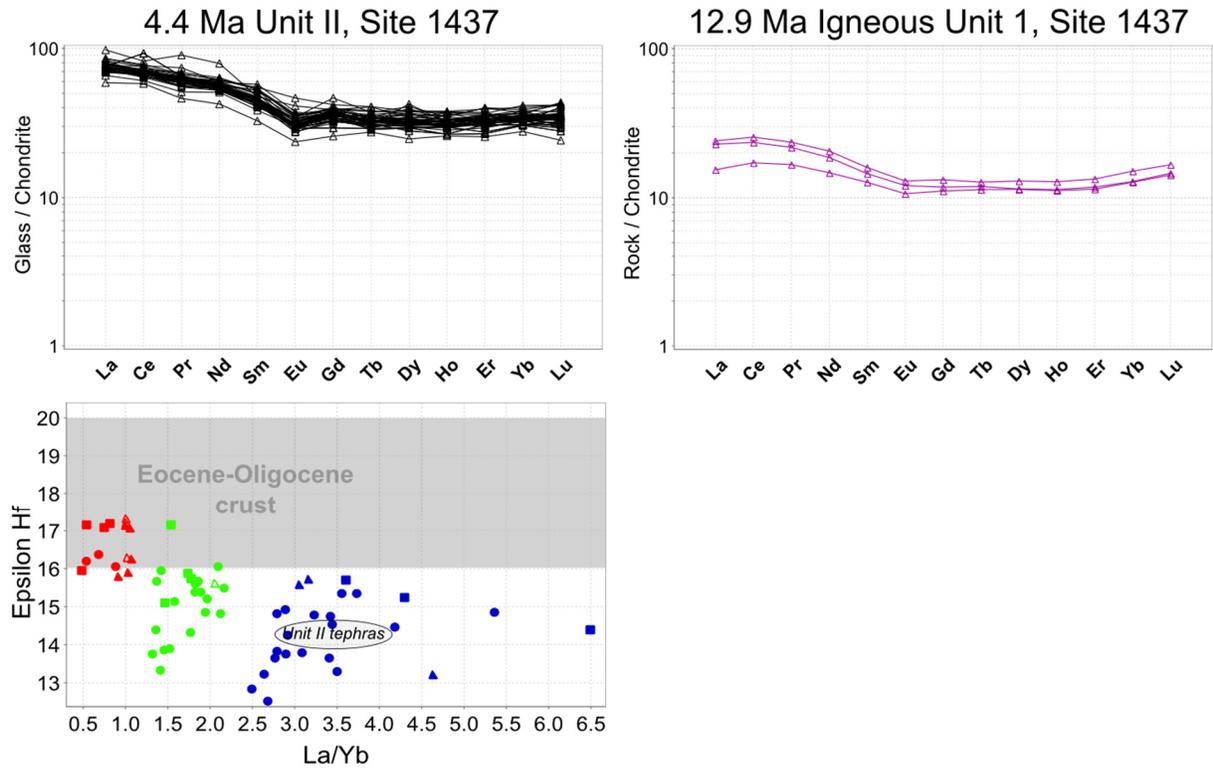
Figure 21: Trace element and isotopic characteristics of Site U1437 Unit II, potential crustal sources (Igneous Unit I and Eocene-Oligocene crust), and dredged rock analyses from the literature (data sources as in figure 6). Unit II rhyolitic tephras and Igneous Unit 1 rhyolitic sill show distinct REE chemistry (La/Yb = 1.9-2.4). Unit II and all other RASC-type magmas show distinct Hf isotopes from Eocene-Oligocene tephras (Straub et al., 2010), Eocene-Oligocene Kyushu-Palau Ridge (Ishizuka et al., 2011), and Eocene crust (Hocking, 2016). Colors correspond to across-arc regions and symbols correspond to SiO_2 as in figure 6. REE patterns are normalized using C1 chondrite values from Sun and McDonough, 1995. Epsilon Hf calculated using chondritic uniform reservoir values (CHUR) from Bouvier et al., 2008.

Table 1: Site U1437 glass chemistry

Interval	U1437B-20F-2-101/102						
ID	B-20F-2_glass1	B-20F-2_glass2	B-20F-2_glass3	B-20F-2_glass4	B-20F-2_glass5	B-20F-2_glass6	B-20F-2_glass7
Depth (mbsf)	132.81	132.81	132.81	132.81	132.81	132.81	132.81
Age (Ma	1.12	1.12	1.12	1.12	1.12	1.12	1.12
Major Elements (wt. %)							
SiO2	53.69	55.73	55.96	64.51	65.19	67.12	67.90
TiO2	1.96	2.15	2.02	0.96	1.06	0.71	0.73
Al2O3	14.07	13.56	14.13	16.20	15.91	16.47	15.25
FeO*	14.84	13.10	13.75	6.37	6.21	5.25	5.70
MnO	0.26	0.27	0.24	0.27	0.22	0.26	0.26
MgO	3.87	3.80	3.46	1.62	1.72	1.00	1.01
CaO	8.22	8.81	7.34	4.67	4.65	4.13	3.69
Na2O	2.36	1.94	2.29	3.83	3.55	3.57	3.92
K2O	0.73	0.63	0.82	1.15	1.04	1.25	1.33
P2O5	0.00	0.00	0.00	0.42	0.43	0.26	0.21
Total	100.00	100.00	100.00	100.00	100.00	100.00	100.00
Trace Elements (ppm)							
Sc	41.3	51.4	42.7	29.2	27.2		
Ni	6.59	2.73	5.27	49.76	4.07		
Rb	11.7	12.2	12.3	19.1	16.4		
Sr	218	275	238	200	212		
Y	24.1	33.3	25.0	48.1	37.4		
Zr	85	128	95	216	164		
Nb	2.82	4.08	2.39	6.77	4.54		
Cs	0.26	0.32	0.42	0.43	0.51		
Ba	58	85	60	148	105		
La	7.8	10.0	7.0	14.9	11.6		
Ce	20.7	26.8	22.6	43.0	31.5		
Pr	3.15	3.80	3.15	6.24	4.37		
Nd	13.4	18.7	14.4	26.8	24.1		
Sm	4.00		4.46		6.87		
Eu	1.28	2.05	1.43	1.86	1.82		
Gd	4.48	6.31	5.25	8.81	6.84		
Tb	0.60	1.18	0.72				
Dy	3.38	6.45	4.10	9.08			
Ho		1.45	0.97	2.36	1.70		
Er	1.93	3.93	3.23	6.04	4.79		
Tm	0.38	0.42		1.04			
Yb		4.10	3.16	6.26	3.72		
Lu	0.26		0.40	0.78	0.56		
Hf	2.14	3.73	2.05	3.37	4.21		
Ta	0.04	0.19	0.16	1.35	0.25		
Pb	3.89	3.75	1.96	54.25	5.44		
Th	0.35	0.96	0.34	1.62	0.98		
U	0.24	0.25	0.30	0.56	0.41		

Table 1: Site U1437 glass chemistry

Interval	U1437B-20F-2-101/102				U1437B-21F-1-93/94		
ID	B-20F-2_glass8	B-20F-2_glass9	B-20F-2_glass10	B-20F-2_glass11	B-21F-1_glass1	B-21F-1_glass2	B-21F-1_glass3
Depth (mbsf)	132.81	132.81	132.81	132.81	135.93	135.93	135.93
Age (Ma	1.12	1.12	1.12	1.12	1.15	1.15	1.15
Major Elements (wt. %)							
SiO2	67.93	68.36	68.83	76.58	54.38	54.70	54.88
TiO2	0.77	0.95	0.74	0.01	2.38	1.94	1.91
Al2O3	16.36	15.19	15.67	15.48	11.81	13.39	13.54
FeO*	4.86	5.82	5.28	0.07	15.70	14.65	13.98
MnO	0.14	0.19	0.22	0.03	0.33	0.30	0.29
MgO	0.73	1.16	1.11	0.04	3.98	3.81	3.95
CaO	3.78	3.89	3.75	0.31	8.20	8.22	8.14
Na2O	3.87	2.96	3.04	5.70	2.43	2.23	2.49
K2O	1.28	1.13	1.05	1.76	0.80	0.74	0.81
P2O5	0.28	0.36	0.29	0.02	0.00	0.00	0.00
Total	100.00	100.00	100.00	100.00	100.00	100.00	100.00
Trace Elements (ppm)							
Sc			21.3				56.2
Ni			0.94				8.97
Rb			19.6				12.7
Sr			180				301
Y			37.4				49.0
Zr			179				160
Nb			5.04				4.85
Cs			0.59				0.29
Ba			117				96
La			11.6				12.9
Ce							29.8
Pr			4.07				4.71
Nd			20.5				
Sm			5.22				7.04
Eu			1.91				2.21
Gd			6.28				9.17
Tb			0.97				1.58
Dy			6.77				9.12
Ho			1.43				
Er			3.73				5.66
Tm			0.68				
Yb							
Lu			0.53				0.82
Hf			3.96				4.05
Ta			0.21				0.38
Pb			4.88				2.98
Th			0.93				0.95
U			0.53				0.50

Table 1: Site U1437 glass chemistry

Interval	U1437B-21F-1-93/94						
ID	B-21F-1_glass4	B-21F-1_glass5	B-21F-1_glass6	B-21F-1_glass7	B-21F-1_glass8	B-21F-1_glass9	B-21F-1_glass10
Depth (mbsf)	135.93	135.93	135.93	135.93	135.93	135.93	135.93
Age (Ma	1.15	1.15	1.15	1.15	1.15	1.15	1.15
Major Elements (wt. %)							
SiO_2	56.50	57.55	59.13	64.65	64.73	65.12	66.24
TiO_2	1.62	1.91	1.66	1.19	0.80	0.90	0.96
Al_2O_3	14.61	12.86	14.55	15.73	17.78	16.39	15.98
FeO*	12.38	12.71	10.25	6.22	4.69	5.20	6.11
MnO	0.26	0.29	0.26	0.23	0.17	0.20	0.23
MgO	3.54	3.12	2.56	2.03	0.87	1.46	1.76
CaO	7.75	6.50	6.16	4.73	5.05	4.65	4.86
Na_2O	2.63	3.74	3.94	3.61	4.65	4.60	2.05
K_2O	0.72	0.91	0.99	1.08	1.04	1.20	1.45
P_2O_5	0.00	0.40	0.52	0.54	0.22	0.28	0.37
Total	100.00	100.00	100.00	100.00	100.00	100.00	100.00
Trace Elements (ppm)							
Sc	40.8						
Ni	1.31						
Rb	11.5						
Sr	251						
Y	28.4						
Zr	102						
Nb	2.88						
Cs	0.29						
Ba	66						
La	7.9						
Ce	23.4						
Pr	3.16						
Nd							
Sm	3.74						
Eu	1.51						
Gd	5.11						
Tb	0.88						
Dy	5.23						
Ho	1.07						
Er	2.70						
Tm							
Yb	2.35						
Lu	0.40						
Hf	2.24						
Ta	0.15						
Pb	2.22						
Th	0.72						
U	0.34						

Table 1: Site U1437 glass chemistry

Interval	U1437B-21f-1-93/94						
ID	B-21F-1_glass11	B-21F-1_glass12	B-21F-1_glass13	B-21F-1_glass14	B-21F-1_glass15	B-21F-1_glass16	B-21F-1_glass17
Depth (mbsf)	135.93	135.93	135.93	135.93	135.93	135.93	135.93
Age (Ma	1.15	1.15	1.15	1.15	1.15	1.15	1.15
Major Elements (wt. %)							
SiO_2	66.41	66.80	67.08	67.12	67.18	67.31	67.84
TiO_2	0.86	0.92	0.95	0.85	1.03	0.93	0.87
Al_2O_3	14.27	15.27	15.90	15.89	15.61	15.68	15.64
FeO^*	5.93	5.78	4.95	4.83	4.91	5.11	4.72
MnO	0.30	0.21	0.18	0.19	0.16	0.11	0.18
MgO	2.88	1.18	1.38	1.40	1.51	1.14	1.10
CaO	5.30	3.82	4.18	3.97	4.10	4.04	3.62
Na_2O	2.76	4.33	3.91	4.03	3.74	2.97	4.53
K_2O	1.06	1.39	1.12	1.50	1.46	2.39	1.33
P_2O_5	0.22	0.29	0.35	0.23	0.31	0.30	0.17
Total	100.00	100.00	100.00	100.00	100.00	100.00	100.00
Trace Elements (ppm)							
Sc			22.5				
Ni							
Rb			18.7				
Sr			194				
Y			33.0				
Zr			147				
Nb			4.16				
Cs			0.63				
Ba			108				
La			10.6				
Ce			30.0				
Pr			4.48				
Nd			19.6				
Sm			5.90				
Eu			1.44				
Gd			6.41				
Tb							
Dy							
Ho			1.71				
Er			3.61				
Tm							
Yb			3.73				
Lu			0.50				
Hf			4.06				
Ta			0.27				
Pb			3.35				
Th			0.94				
U			0.45				

Table 1: Site U1437 glass chemistry

Interval	U1437B-21f-1-93/94		U1437B-33X-1-88/86				
ID	B-21F-1_glass18	B-21F-1_glass19	B-33X-1_glass1	B-33X-1_glass2	B-33X-1_glass3	B-33X-1_glass4	B-33X-1_glass5
Depth (mbsf)	135.93	135.93	224.08	224.08	224.08	224.08	224.08
Age (Ma	1.15	1.15	1.89	1.89	1.89	1.89	1.89
Major Elements (wt. %)							
SiO2	68.37	68.85	49.34	50.95	54.38	61.84	76.23
TiO2	0.88	0.81	1.08	1.48	1.93	0.93	0.21
Al2O3	16.15	16.18	15.77	15.56	13.85	15.45	13.99
FeO*	4.90	4.34	12.65	14.06	14.95	8.08	1.14
MnO	0.19	0.20	0.22	0.27	0.30	0.23	0.06
MgO	1.33	1.30	6.33	5.05	3.43	2.56	0.28
CaO	4.00	3.85	12.50	10.64	7.92	7.06	1.64
Na2O	2.90	3.10	1.32	1.13	2.30	3.17	3.05
K2O	1.03	1.10	0.78	0.87	0.94	0.52	3.38
P2O5	0.26	0.27	0.00	0.00	0.00	0.16	0.03
Total	100.00	100.00	100.00	100.00	100.00	100.00	100.00
Trace Elements (ppm)							
Sc	26.2						
Ni	8.18						
Rb	24.8						
Sr	222						
Y	39.2						
Zr	257						
Nb	6.74						
Cs	0.97						
Ba	145						
La	14.1						
Ce	42.4						
Pr	5.94						
Nd	27.8						
Sm	7.53						
Eu	1.75						
Gd	6.79						
Tb	1.13						
Dy	8.58						
Ho							
Er	5.35						
Tm							
Yb	4.87						
Lu							
Hf	4.03						
Ta	1.17						
Pb	13.60						
Th	2.25						
U	0.78						

Table 1: Site U1437 glass chemistry

Interval	U1437B-33X-1-88/89						
ID	B-33X-1_glass6	B-33X-1_glass7	B-33X-1_glass8	B-33X-1_glass9	B-33X-1_glass10	B-33X-1_glass11	B-33X-1_glass12
Depth (mbsf)	224.08	224.08	224.08	224.08	224.08	224.08	224.08
Age (Ma	1.89	1.89	1.89	1.89	1.89	1.89	1.89
Major Elements (wt. %)							
SiO2	77.23	77.25	77.35	77.45	77.46	77.61	77.77
TiO2	0.16	0.19	0.18	0.15	0.16	0.17	0.19
Al2O3	13.64	13.56	13.64	13.43	13.48	13.24	13.73
FeO*	0.88	1.02	0.90	1.07	1.08	1.05	0.95
MnO	0.10	0.13	0.09	0.06	0.03	0.09	0.07
MgO	0.23	0.21	0.24	0.20	0.21	0.23	0.23
CaO	1.27	1.29	1.30	1.30	1.31	1.29	1.26
Na2O	3.21	2.67	3.14	3.04	3.14	3.10	2.99
K2O	3.25	3.62	3.12	3.28	3.12	3.21	2.80
P2O5	0.03	0.05	0.03	0.02	0.00	0.02	0.02
Total	100.00	100.00	100.00	100.00	100.00	100.00	100.00
Trace Elements (ppm)							
Sc							
Ni							
Rb							
Sr							
Y							
Zr							
Nb							
Cs							
Ba							
La							
Ce							
Pr							
Nd							
Sm							
Eu							
Gd							
Tb							
Dy							
Ho							
Er							
Tm							
Yb							
Lu							
Hf							
Ta							
Pb							
Th							
U							

Table 1: Site U1437 glass chemistry

Interval	U1437B-33X-1-88/89				U1437B-35X-2-6/7		
ID	B-33X-1_glass13	B-33X-1_glass14	B-33X-1_glass15	B-33X-1_glass16	B-35X-2_glass1	B-35X-2_glass2	B-35X-2_glass3
Depth (mbsf)	224.08	224.08	224.08	224.08	244.16	244.16	244.16
Age (Ma	1.89	1.89	1.89	1.89	2.02	2.02	2.06
Major Elements (wt. %)							
SiO2	77.81	77.85	77.95	78.01	78.91	78.93	78.93
TiO2	0.17	0.15	0.13	0.13	0.14	0.18	0.18
Al2O3	13.75	13.44	13.92	13.37	12.61	12.62	12.62
FeO*	0.86	1.02	0.88	1.03	1.25	1.36	1.36
MnO	0.10	0.07	0.07	0.03	0.06	0.00	0.00
MgO	0.24	0.21	0.23	0.22	0.18	0.17	0.17
CaO	1.34	1.29	1.30	1.30	1.14	1.20	1.20
Na2O	2.78	2.87	2.87	2.83	2.89	2.30	2.30
K2O	2.94	3.07	2.63	3.02	2.80	3.21	3.21
P2O5	0.02	0.04	0.00	0.05	0.02	0.03	0.03
Total	100.00	100.00	100.00	100.00	100.00	100.00	100.00
Trace Elements (ppm)							
Sc							11.6
Ni							
Rb							41.2
Sr							88
Y							19.7
Zr							130
Nb							4.69
Cs							1.03
Ba							221
La							13.4
Ce							25.5
Pr							3.37
Nd							11.0
Sm							3.24
Eu							0.43
Gd							2.13
Tb							0.46
Dy							2.57
Ho							
Er							2.01
Tm							0.27
Yb							2.25
Lu							0.53
Hf							3.35
Ta							0.47
Pb							6.50
Th							2.99
U							1.24

Table 1: Site U1437 glass chemistry

Interval	U1437B-35X-2-6/7					U1437B-45X-1-79/81	
ID	B-35X-2_glass4	B-35X-2_glass5	B-35X-2_glass6	B-35X-2_glass7	B-35X-2_glass8	B-45X-1_glass1	B-45X-1_glass2
Depth (mbsf)	244.16	244.16	244.16	244.16	244.16	340.385	340.385
Age (Ma	2.06	2.06	2.06	2.02	2.02	2.48	2.48
Major Elements (wt. %)							
SiO_2	79.01	79.28	79.31	79.91	80.33	50.52	51.66
TiO_2	0.16	0.18	0.21	0.20	0.13	1.60	1.77
Al_2O_3	12.73	12.43	12.88	12.77	12.85	13.95	13.53
FeO*	1.27	1.08	1.50	1.18	1.31	15.04	16.15
MnO	0.02	0.02	0.04	0.05	0.07	0.25	0.26
MgO	0.18	0.17	0.24	0.19	0.21	5.40	4.52
CaO	1.28	1.17	1.55	1.29	1.28	10.49	9.21
Na_2O	2.76	2.48	2.05	2.22	2.36	2.27	2.37
K_2O	2.60	3.19	2.22	2.18	1.41	0.48	0.54
P_2O_5	0.00	0.00	0.01	0.02	0.05	0.00	0.00
Total	100.00	100.00	100.00	100.00	100.00	100.00	100.00
Trace Elements (ppm)							
Sc	12.0	11.5	14.7			50.8	28.6
Ni	3.97	5.29				15.10	8.90
Rb	42.7	43.6	37.3			15.4	25.6
Sr	79	81	132			362	467
Y	17.2	19.5	25.0			18.2	13.6
Zr	113	130	215			55	42
Nb	4.48	4.17	4.91			2.04	1.67
Cs	1.13	1.34	0.92			0.91	0.51
Ba	199	244	235			73	60
La	10.0	11.9	14.2			5.2	
Ce	26.1	27.7	29.4			13.1	26.1
Pr		2.89	3.94			2.02	3.54
Nd	11.8	11.6	14.9			8.7	14.3
Sm	1.97	3.19	3.19			2.76	4.79
Eu	0.40	0.57	0.83			1.04	
Gd	2.46	1.87				3.41	
Tb	0.40		0.61				0.49
Dy	2.57	2.62				3.92	3.70
Ho	0.62	0.60	0.95			0.79	0.59
Er	1.59	2.30	3.43				1.73
Tm	0.25					0.28	
Yb		2.15	3.01			2.42	
Lu	0.40	0.52	0.46			0.32	0.16
Hf	2.99	3.42	4.28			1.93	0.97
Ta	0.27	0.40	0.30			0.11	
Pb	20.18	6.00	4.72			4.08	1.77
Th	2.53	2.66	3.11			0.68	0.66
U	1.01	0.89	0.83			0.40	0.29

Table 1: Site U1437 glass chemistry

Interval	U1437B-45X-1-79/81		U1437B-52X-CC-2/4				
ID	B-45X-1_glass3	B-45X-1_glass4	B-52X-CC_glass1	B-52X-CC_glass2	B-52X-CC_glass3	B-52X-CC_glass4	B-52X-CC_glass5
Depth (mbsf)	340.385	340.385	410.46	410.46	410.46	410.46	410.46
Age (Ma	2.48	2.48	2.84	2.84	2.84	2.84	2.84
Major Elements (wt. %)							
SiO2	78.08	79.98	78.57	78.58	78.75	79.01	79.07
TiO2	0.18	0.10	0.34	0.33	0.34	0.32	0.32
Al2O3	13.30	12.66	12.18	12.05	12.12	12.21	11.91
FeO*	0.86	1.21	1.83	1.75	1.82	1.78	1.79
MnO	0.09	0.03	0.12	0.06	0.13	0.06	0.09
MgO	0.23	0.11	0.23	0.24	0.23	0.24	0.23
CaO	1.21	0.91	1.27	1.29	1.26	1.32	1.25
Na2O	3.16	1.91	3.02	3.40	3.58	2.17	3.16
K2O	2.81	3.08	2.43	2.25	1.72	2.87	2.13
P2O5	0.09	0.00	0.02	0.04	0.03	0.01	0.04
Total	100.00	100.00	100.00	100.00	100.00	100.00	100.00
Trace Elements (ppm)							
Sc							
Ni							
Rb							
Sr							
Y							
Zr							
Nb							
Cs							
Ba							
La							
Ce							
Pr							
Nd							
Sm							
Eu							
Gd							
Tb							
Dy							
Ho							
Er							
Tm							
Yb							
Lu							
Hf							
Ta							
Pb							
Th							
U							

Table 1: Site U1437 glass chemistry

Interval	U1437B-52X-CC-2/4						
ID	B-52X-CC_glass6	B-52X-CC_glass7	B-52X-CC_glass8	B-52X-CC_glass9	B-52X-CC_glass10	B-52X-CC_glass11	B-52X-CC_glass12
Depth (mbsf)	410.46	410.46	410.46	410.46	410.46	410.46	410.46
Age (Ma	2.84	2.84	2.84	2.84	2.84	2.84	2.84
Major Elements (wt. %)							
SiO_2	79.13	79.63	79.87	80.09	80.20	80.85	82.32
TiO_2	0.33	0.32	0.32	0.32	0.33	0.34	0.33
Al_2O_3	12.12	12.23	12.21	11.84	12.02	12.16	12.33
FeO*	1.62	1.67	1.64	1.76	1.80	1.84	1.80
MnO	0.12	0.10	0.10	0.07	0.10	0.10	0.08
MgO	0.22	0.22	0.23	0.23	0.22	0.23	0.24
CaO	1.27	1.25	1.25	1.25	1.16	1.26	1.26
Na_2O	3.16	2.73	2.29	2.64	2.20	2.14	0.65
K_2O	1.98	1.84	2.09	1.79	1.96	1.05	0.98
P_2O_5	0.04	0.01	0.01	0.01	0.01	0.02	0.01
Total	100.00	100.00	100.00	100.00	100.00	100.00	100.00
Trace Elements (ppm)							
Sc							
Ni							
Rb							
Sr							
Y							
Zr							
Nb							
Cs							
Ba							
La							
Ce							
Pr							
Nd							
Sm							
Eu							
Gd							
Tb							
Dy							
Ho							
Er							
Tm							
Yb							
Lu							
Hf							
Ta							
Pb							
Th							
U							

Table 1: Site U1437 glass chemistry

Interval	U1437D-05r-2-102-103						
ID	D-05R-2_glass1	D-05R-2_glass2	D-05R-2_glass3	D-05R-2_glass4	D-05R-2_glass5	D-05R-2_glass6	D-05R-2_glass7
Depth (mbsf)	458.82	458.82	458.82	458.82	458.82	458.82	458.82
Age (Ma	3.10	3.10	2.84	3.10	3.10	3.10	3.10
Major Elements (wt. %							
SiO_2	53.96	54.94	74.81	75.84	76.06	76.56	76.58
TiO_2	1.62	1.55	0.28	0.19	0.20	0.13	0.15
Al_2O_3	13.27	14.10	13.97	13.53	13.95	13.50	13.64
FeO*	16.04	13.12	1.79	1.63	1.64	1.46	1.35
MnO	0.29	0.27	0.15	0.10	0.16	0.16	0.13
MgO	4.39	3.77	0.32	0.17	0.16	0.10	0.14
CaO	9.43	7.80	1.45	1.08	1.09	1.02	1.05
Na_2O	0.87	3.17	3.98	3.98	3.15	3.55	3.52
K_2O	0.14	0.97	3.26	3.47	3.58	3.51	3.42
P_2O_5	0.00	0.30	0.00	0.00	0.01	0.01	0.01
Total	100.00	100.00	100.00	100.00	100.00	100.00	100.00
Trace Elements (ppm)							
Sc	18.3		18.1	15.7	19.5		21.1
Ni			3.01		3.57		
Rb	40.1		39.2	31.5	41.5		43.6
Sr	46		232	80	159		233
Y	32.4		46.8	41.7	56.0		48.9
Zr	155		193	181	221		197
Nb	5.26		7.02	7.06	6.98		7.64
Cs	0.94		1.39	0.81	1.57		1.72
Ba	82		256	224	294		256
La	9.7		18.2	15.2	20.8		19.0
Ce	29.5		40.3	38.1	46.5		43.9
Pr	3.33		5.92	5.24	6.68		6.07
Nd	14.5		27.4	23.5	32.0		27.4
Sm	4.75		6.90	6.42	7.76		7.28
Eu			1.84	1.42	1.79		1.45
Gd	5.44		7.49	5.76	9.17		9.57
Tb			1.17	1.02	1.51		1.16
Dy	6.25		8.20	7.31	9.56		7.79
Ho	1.13		1.59	1.52	1.98		1.68
Er	3.14		5.43	4.61	6.28		5.79
Tm	0.53		0.76	0.67	0.99		0.79
Yb	2.49		5.48	4.68	6.75		4.98
Lu			0.81	0.73	1.05		0.85
Hf	3.30		5.77	5.03	6.48		4.91
Ta	0.20		0.46	0.46	0.65		0.61
Pb	3.21		6.44	5.39	7.01		8.21
Th	1.58		2.58	2.19	3.39		3.50
U	0.61		0.98	0.86	1.04		1.18

Table 1: Site U1437 glass chemistry

Interval	U1437D-05R-2-102/103						
ID	D-05R-2_glass8	D-05R-2_glass9	D-05R-2_glass12	D-05R-2_glass13	D-05R-2_glass14	D-05R-2_glass15	D-05R-2_glass16
Depth (mbsf)	458.82	458.82	458.82	458.82	458.82	458.82	458.82
Age (Ma	3.10	3.10	3.10	3.10	3.10	3.10	3.10
Major Elements (wt. %)							
SiO2	76.79	76.79	77.21	77.23	77.74	77.81	78.26
TiO2	0.12	0.14	0.17	0.27	0.12	0.14	0.20
Al2O3	13.55	13.20	13.03	13.57	13.15	13.09	13.30
FeO*	1.56	1.46	1.50	2.51	1.47	1.62	1.46
MnO	0.14	0.14	0.10	0.09	0.18	0.18	0.11
MgO	0.11	0.11	0.13	0.15	0.11	0.13	0.10
CaO	1.03	1.01	0.89	1.03	0.90	0.99	0.95
Na2O	3.12	3.61	3.59	2.60	3.09	2.50	2.31
K2O	3.57	3.53	3.36	2.51	3.24	3.52	3.31
P2O5	0.01	0.01	0.01	0.04	0.01	0.01	0.01
Total	100.00	100.00	100.00	100.00	100.00	100.00	100.00
Trace Elements (ppm)							
Sc	16.1	17.5	14.2		14.5	19.7	17.8
Ni	1.29	2.02	2.26			9.97	
Rb	37.4	38.8	27.3		33.0	50.7	36.4
Sr	111	126	156		70	293	82
Y	47.9	53.2	30.3		36.1	52.6	47.5
Zr	158	176	103		125	211	188
Nb	6.41	8.11	5.86		6.37	7.58	7.29
Cs	1.06	1.21	0.65		0.78	2.12	1.03
Ba	290	288	227		219	354	269
La	16.7	19.3	12.2		13.6	21.7	18.0
Ce	38.5	42.8	32.3		35.7	44.4	40.4
Pr	5.48	6.22	4.16		4.80	6.38	5.98
Nd	24.2	27.6	17.5		22.0	31.1	28.3
Sm	6.74	7.54	4.49		5.06	7.53	7.06
Eu	1.32	1.58	1.67		1.21	1.74	1.30
Gd	6.97	7.97	4.74		5.72	7.88	6.94
Tb	1.05	1.32	0.80		0.94	1.33	1.28
Dy	7.45	9.08	5.14		6.35	8.95	7.54
Ho	1.60	1.75	1.02		1.24	2.05	1.69
Er	4.85	5.88	3.41		3.84	5.78	4.92
Tm	0.71	0.83	0.45		0.55	0.90	0.76
Yb	4.87	5.57	3.70		4.22	5.60	5.38
Lu	0.77	0.89	0.52		0.62	0.92	0.80
Hf	4.60	5.41	3.34		3.44	6.45	4.96
Ta	0.49	0.51	0.45		0.48	0.65	0.54
Pb	8.42	6.11	5.09		6.10	7.03	8.43
Th	2.40	2.77	1.64		2.08	3.69	2.22
U	0.88	1.06	0.73		0.89	1.33	0.93

Table 1: Site U1437 glass chemistry

Interval	U1437D-05R-2-102/103					U1437D-08R-1-68/69	
ID	D-05R-2_glass17	D-05R-2_glass18	D-05R-2_glass19	D-05R-2_glass20	D-05R-2_glass21	D-08R-1_glass1	D-08R-1_glass2
Depth (mbsf)	458.82	458.82	458.82	458.82	458.82	486.08	486.08
Age (Ma	3.10	3.10	3.10	3.10	3.10	3.24	3.24
Major Elements (wt. %)							
SiO2	78.29	79.01	79.24	79.96	80.59	52.84	56.23
TiO2	0.14	0.19	0.19	0.15	0.17	1.46	1.21
Al2O3	13.55	13.06	13.55	13.64	13.31	14.68	13.67
FeO*	1.48	1.56	1.47	1.49	1.23	12.58	13.37
MnO	0.12	0.18	0.10	0.09	0.08	0.24	0.28
MgO	0.16	0.13	0.15	0.11	0.23	5.05	3.64
CaO	1.00	0.85	0.98	0.94	1.37	9.55	8.37
Na2O	2.62	2.47	2.37	2.11	1.76	2.81	2.65
K2O	2.62	2.55	1.93	1.48	1.25	0.50	0.43
P2O5	0.03	0.01	0.02	0.02	0.01	0.31	0.16
Total	100.00	100.00	100.00	100.00	100.00	100.00	100.00
Trace Elements (ppm)							
Sc							
Ni							
Rb							
Sr							
Y							
Zr							
Nb							
Cs							
Ba							
La							
Ce							
Pr							
Nd							
Sm							
Eu							
Gd							
Tb							
Dy							
Ho							
Er							
Tm							
Yb							
Lu							
Hf							
Ta							
Pb							
Th							
U							

Table 1: Site U1437 glass chemistry

Interval	U1437D-08R-1-68/69		U1437D-23R-4-56/57			U1437D-26R-4-53/54	
ID	D-08R-1_glass3	D-08R-1_glass5	D-23R-4_glass1	D-23R-4_glass2	D-23R-4_glass3	D-26R-4_glass1	D-26R-4_glass2
Depth (mbsf)	486.08	486.08	635.87	635.87	635.87	665.13	665.13
Age (Ma	3.24	3.24	4.02	4.02	4.02	4.18	4.18
Major Elements (wt. %)							
SiO2	69.58	73.46	62.45	67.81	68.48	54.64	57.08
TiO2	0.54	0.30	0.92	0.63	0.64	1.49	1.26
Al2O3	16.16	15.47	16.69	16.81	16.77	13.46	15.30
FeO*	4.24	2.93	7.76	5.57	5.30	13.34	10.24
MnO	0.15	0.14	0.23	0.10	0.21	0.29	0.29
MgO	0.72	0.32	2.05	0.90	0.90	3.72	3.33
CaO	2.64	1.71	5.30	3.40	3.31	8.54	7.26
Na2O	3.42	3.32	1.68	1.42	1.27	2.99	3.60
K2O	2.40	2.31	2.63	3.18	2.93	1.16	1.19
P2O5	0.14	0.03	0.29	0.18	0.19	0.37	0.45
Total	100.00	100.00	100.00	100.00	100.00	100.00	100.00
Trace Elements (ppm)							
Sc	26.2			26.3	24.4	42.6	30.9
Ni				8.37	8.66	12.18	4.53
Rb	56.6			64.6	57.9	18.7	19.5
Sr	363			345	315	321	341
Y	63.8			37.4	58.8	33.2	37.2
Zr	231			241	309	133	140
Nb	6.27			12.11	10.43	3.61	4.11
Cs	1.54			2.08	1.48	0.70	0.57
Ba	227			310	301	97	151
La	21.9			24.4		10.2	12.8
Ce	44.5			43.2	39.4	20.1	27.0
Pr	7.92			6.20	6.33	3.44	4.19
Nd	36.4			27.7	30.3	17.2	21.7
Sm	9.28			6.16	9.06	4.36	5.66
Eu	2.53			1.77	1.71	1.58	1.85
Gd	9.66			7.73	8.46	5.42	6.47
Tb	1.47				1.28	0.94	1.00
Dy				6.64	9.38	6.04	6.65
Ho				1.40	1.73	1.32	1.37
Er	6.61			3.63	6.16	3.67	4.06
Tm				0.68	1.01	0.51	0.56
Yb	6.41			3.86	5.13	3.56	3.95
Lu				0.45		0.52	0.62
Hf	5.94			5.21	7.03	4.01	3.81
Ta	1.75			0.73	0.67	0.27	0.31
Pb	12.70			7.33	10.00	6.26	4.23
Th	2.74			4.11	4.42	1.51	1.70
U	0.55			1.02	0.84	0.48	0.59

Table 1: Site U1437 glass chemistry

Interval	U1437D-26R-4-53/54						
ID	D-26R-4_glass3	D-26R-4_glass4	D-26R-4_glass5	D-26R-4_glass6	D-26R-4_glass7	D-26R-4_glass8	D-26R-4_glass9
Depth (mbsf)	665.13	665.13	665.13	665.13	665.13	665.13	665.13
Age (Ma	4.18	4.18	4.18	4.18	4.18	4.18	4.18
Major Elements (wt. %)							
SiO2	57.72	58.05	58.30	58.40	58.81	58.89	60.07
TiO2	1.37	1.01	1.36	1.36	1.20	1.30	1.20
Al2O3	15.77	14.77	14.61	14.62	15.86	14.75	15.42
FeO*	9.75	9.78	9.79	9.69	9.47	9.34	9.39
MnO	0.29	0.23	0.26	0.23	0.23	0.25	0.23
MgO	3.18	3.86	3.47	3.49	3.00	3.37	2.83
CaO	6.90	8.13	7.71	7.69	6.77	7.62	6.47
Na2O	3.33	3.08	3.13	3.12	2.80	3.06	2.56
K2O	1.12	0.69	1.03	1.03	1.40	1.06	1.35
P2O5	0.56	0.39	0.34	0.37	0.46	0.36	0.48
Total	100.00	100.00	100.00	100.00	100.00	100.00	100.00
Trace Elements (ppm)							
Sc	28.0			39.8	38.9	39.6	33.6
Ni	6.03			4.17	4.44	4.07	7.01
Rb	17.3			13.8	19.9	17.7	22.1
Sr	336			438	400	298	328
Y	28.1			26.0	45.0	26.1	37.2
Zr	101			87	155	90	144
Nb	3.53			2.71	4.14	2.61	4.37
Cs	0.45			0.63	0.64	0.64	0.72
Ba	133			121	142	121	144
La	10.0			9.3	13.6	9.1	12.8
Ce	24.0			20.7	28.4	22.3	28.4
Pr	3.62			3.05	4.43	3.07	4.46
Nd	17.2			15.5	23.7	15.7	21.9
Sm	4.96				6.68	3.96	6.07
Eu	1.66			1.31	2.09	1.34	1.85
Gd	5.09				7.96	5.07	6.66
Tb	0.72				1.24		1.09
Dy	5.07				8.11		6.91
Ho	0.99			0.93	1.71		1.49
Er	2.93			2.32	5.17	2.94	4.10
Tm	0.45			0.41	0.61		0.60
Yb	2.89			2.68	4.43	2.86	4.14
Lu	0.44			0.43	0.68	0.41	0.52
Hf	2.92			2.58	4.23	2.44	4.19
Ta	0.22			0.10	0.32		0.29
Pb	5.07			2.91	3.86	3.11	5.50
Th	1.28			0.93	1.77	0.93	1.83
U	0.48			0.34	0.48	0.50	0.60

Table 1: Site U1437 glass chemistry

Interval	U1437D-26R-4-53/54						
ID	D-26R-4_glass10	D-26R-4_glass11	D-26R-4_glass12	D-26R-4_glass13	D-26R-4_glass14	D-26R-4_glass15	D-26R-4_glass16
Depth (mbsf)	665.13	665.13	665.13	665.13	665.13	665.13	665.13
Age (Ma	4.18	4.18	4.18	4.18	4.18	4.18	4.18
Major Elements (wt. %)							
SiO2	60.98	62.04	63.16	63.27	65.61	65.62	69.66
TiO2	0.81	1.20	1.44	1.03	0.99	1.01	0.85
Al2O3	16.23	14.03	14.14	15.72	15.38	14.85	15.08
FeO*	8.10	9.19	9.30	8.20	6.56	7.11	4.83
MnO	0.12	0.20	0.23	0.21	0.18	0.25	0.16
MgO	2.75	3.83	1.86	2.72	1.61	1.57	1.16
CaO	6.35	6.80	5.43	6.40	4.43	4.68	3.61
Na2O	3.47	1.37	1.73	1.29	3.02	2.42	2.76
K2O	0.99	1.02	1.65	0.73	1.76	2.05	1.60
P2O5	0.21	0.32	1.06	0.44	0.46	0.45	0.28
Total	100.00	100.00	100.00	100.00	100.00	100.00	100.00
Trace Elements (ppm)							
Sc	35.3	28.6	47.1		29.2	29.0	22.3
Ni	12.70	4.02	10.68		7.58	4.20	5.83
Rb	23.9	24.8	24.8		27.4	32.3	22.8
Sr	336	293	325		310	311	281
Y	52.2	31.2	41.3		55.5	57.4	46.2
Zr	202	130	160		236	251	184
Nb	5.50	4.50	5.60		6.35	6.07	4.53
Cs	0.72	0.63	1.24		0.84	0.94	0.81
Ba	158	163	221		201	221	178
La	16.4	11.3	15.3		18.0	20.5	12.9
Ce	33.4	28.9	28.4		37.2	42.3	28.2
Pr	5.37	4.35	4.32		6.15	6.49	4.45
Nd	28.8	24.0	20.6		30.0	33.1	22.0
Sm	7.76	5.71	6.04		8.82	9.09	6.49
Eu	2.20		1.67		2.38	2.34	1.91
Gd	9.71		6.78		9.81	9.84	7.10
Tb	1.48	1.19	1.21		1.55	1.61	1.24
Dy	9.26	6.58	7.42		10.77	9.95	8.24
Ho	1.95		1.60		2.01	2.16	1.76
Er	6.08	3.31	4.70		6.39	6.36	5.31
Tm	0.81		0.68		0.90	0.95	0.74
Yb	5.60	2.97	4.34		6.08	5.98	5.12
Lu	0.80	0.41	0.73		0.93	0.95	0.82
Hf	5.64	3.17	4.92		6.18	7.37	5.29
Ta	0.41	0.17	0.36		0.45	0.52	0.33
Pb	7.65	4.67	7.12		7.02	5.93	5.77
Th	2.56	1.89	3.58		2.68	3.32	1.98
U	0.75	0.70	0.71		0.83	0.98	0.67

Table 1: Site U1437 glass chemistry

Interval	U1437D-26R4-53/54	U1437D-28r-2-99/101				U1437D-28r-2-107/109	
ID	D-26R-4_glass17	D-28R-2a_glass1	D-28R-2a_glass2	D-28R-2a_glass3	D-28R-2a_glass4	D-28R-2b_glass1	D-28R-2b_glass2
Depth (mbsf)	665.13	681.99	681.99	681.99	681.99	682.07	682.07
Age (Ma	4.18	4.25	4.25	4.25	4.25	4.25	4.25
Major Elements (wt. %)							
SiO_2	73.36	74.48	74.87	75.05	75.28	74.34	74.43
TiO_2	0.68	0.32	0.33	0.33	0.29	0.32	0.26
Al_2O_3	14.67	14.08	14.40	14.13	14.05	14.64	14.64
FeO^*	4.07	2.02	2.42	2.36	2.27	2.69	2.25
MnO	0.15	0.11	0.00	0.08	0.05	0.11	0.11
MgO	0.71	0.45	0.47	0.49	0.37	0.52	0.46
CaO	2.88	2.39	2.50	2.50	2.29	2.61	2.50
Na_2O	1.10	3.29	2.22	2.24	2.46	2.09	2.35
K_2O	2.22	2.81	2.75	2.75	2.87	2.65	2.99
P_2O_5	0.15	0.05	0.04	0.06	0.06	0.04	0.00
Total	100.00	100.00	100.00	100.00	100.00	100.00	100.00
Trace Elements (ppm)							
Sc	34.0						
Ni	12.57						
Rb	26.5						
Sr	438						
Y	47.9						
Zr	204						
Nb	5.15						
Cs	0.91						
Ba	197						
La	15.0						
Ce	30.1						
Pr	4.88						
Nd	25.3						
Sm	5.83						
Eu	1.84						
Gd	9.29						
Tb	1.42						
Dy	9.31						
Ho	1.85						
Er	5.43						
Tm	0.79						
Yb	5.05						
Lu	0.76						
Hf	5.33						
Ta	0.30						
Pb	7.14						
Th	2.12						
U	0.69						

Table 1: Site U1437 glass chemistry

Interval	U1437D-28r-2-107/109				
ID	D-28R-2b_glass3	D-28R-2b_glass4	D-28R-2b_glass5	D-28R-2b_glass6	D-28R-2b_glass7
Depth (mbsf)	682.07	682.07	682.07	682.07	682.07
Age (Ma	4.25	4.25	4.25	4.25	4.25
Major Elements (wt. %)					
SiO_2	74.47	74.50	74.78	74.87	74.88
TiO_2	0.36	0.27	0.36	0.33	0.33
Al_2O_3	14.56	14.72	14.45	14.40	14.48
FeO*	2.40	2.36	2.39	2.42	2.51
MnO	0.11	0.16	0.10	0.00	0.07
MgO	0.49	0.45	0.51	0.47	0.42
CaO	2.58	2.48	2.44	2.50	2.55
Na_2O	2.18	2.31	2.18	2.22	2.05
K_2O	2.77	2.74	2.70	2.75	2.67
P_2O_5	0.06	0.01	0.09	0.04	0.05
Total	100.00	100.00	100.00	100.00	100.00
Trace Elements (ppm)					
Sc		15.8		17.4	
Ni		11.25			
Rb		32.5		28.9	
Sr		171		175	
Y		34.6		39.6	
Zr		283		269	
Nb		2.80		3.78	
Cs		1.28		0.77	
Ba		213		245	
La		14.7		15.5	
Ce		21.4		24.3	
Pr		3.27		3.83	
Nd		14.9			
Sm				3.57	
Eu		1.59			
Gd		4.71		4.75	
Tb		1.13		0.93	
Dy		6.47		5.30	
Ho				1.08	
Er		4.23		3.26	
Tm		0.69		0.64	
Yb		4.27		4.12	
Lu				0.71	
Hf		12.45		8.49	
Ta					
Pb		2.79		4.23	
Th		2.89		3.66	
U		0.18		0.72	

Table 1: Site U1437 glass chemistry

Interval	U1437D-29R-2-125/126						
ID	D-29R-2_glass1	D-29R-2_glass2	D-29R-2_glass3	D-29R-2_glass4	D-29R-2_glass5	D-29R-2_glass6	D-29R-2_glass7
Depth (mbsf)	691.8	691.8	691.8	691.8	691.8	691.8	691.8
Age (Ma	4.29	4.29	4.29	4.29	4.29	4.29	4.29
Major Elements (wt. %							
SiO2	72.09	72.47	72.48	72.73	72.94	73.57	74.05
TiO2	0.46	0.44	0.42	0.40	0.46	0.37	0.36
Al2O3	15.31	15.14	15.32	15.21	15.11	14.66	14.48
FeO*	3.15	3.19	2.88	3.33	2.92	2.95	2.85
MnO	0.11	0.12	0.13	0.11	0.22	0.13	0.14
MgO	0.69	0.70	0.72	0.64	0.66	0.43	0.45
CaO	3.00	2.95	3.13	2.94	2.97	2.34	2.26
Na2O	2.59	2.56	2.41	2.06	2.10	2.54	2.55
K2O	2.49	2.36	2.45	2.47	2.50	2.91	2.84
P2O5	0.10	0.07	0.05	0.11	0.11	0.10	0.03
Total	100.00	100.00	100.00	100.00	100.00	100.00	100.00
Trace Elements (ppm)							
Sc							
Ni							
Rb							
Sr							
Y							
Zr							
Nb							
Cs							
Ba							
La							
Ce							
Pr							
Nd							
Sm							
Eu							
Gd							
Tb							
Dy							
Ho							
Er							
Tm							
Yb							
Lu							
Hf							
Ta							
Pb							
Th							
U							

Table 1: Site U1437 glass chemistry

Interval	U1437D-29R 2-125/126	U1437D-30R-4-58/61				U1437D-30R-5- 129/132	
ID	D-29R- 2_glass8	D-30R- 4_glass1	D-30R- 4_glass2	D-30R- 4_glass3	D-30R- 4_glass4	D-30R- 5a_glass1	D-30R- 5a_glass2
Depth (mbsf)	691.8	703.42	703.42	703.42	703.42	705.58	705.58
Age (Ma	4.29	4.33	4.33	4.33	4.33	4.34	4.34
Major Elements (wt. %)							
SiO_2	74.89	76.06	76.12	76.19	76.57	73.50	73.82
TiO_2	0.29	0.36	0.29	0.36	0.26	0.31	0.24
Al_2O_3	14.19	14.06	13.71	13.96	13.43	14.54	14.32
FeO*	2.68	1.94	1.82	1.74	1.57	2.02	1.84
MnO	0.10	0.13	0.13	0.10	0.12	0.22	0.17
MgO	0.41	0.36	0.29	0.40	0.27	0.45	0.38
CaO	2.13	1.77	1.68	1.76	1.57	1.84	1.79
Na_2O	2.42	2.35	2.73	2.52	2.90	3.69	3.79
K_2O	2.86	2.93	3.22	2.96	3.29	3.43	3.66
P_2O_5	0.04	0.04	0.01	0.02	0.02	0.00	0.00
Total	100.00	100.00	100.00	100.00	100.00	100.00	100.00
Trace Elements (ppm)							
Sc							
Ni							
Rb							
Sr							
Y							
Zr							
Nb							
Cs							
Ba							
La							
Ce							
Pr							
Nd							
Sm							
Eu							
Gd							
Tb							
Dy							
Ho							
Er							
Tm							
Yb							
Lu							
Hf							
Ta							
Pb							
Th							
U							

Table 1: Site U1437 glass chemistry

Interval	U1437D-30R-5-129/132						
ID	D-30R-5a_glass3	D-30R-5a_glass4	D-30R-5a_glass5	D-30R-5a_glass6	D-30R-5a_glass7	D-30R-5a_glass8	D-30R-5a_glass9
Depth (mbsf)	705.58	705.58	705.58	705.58	705.58	705.58	705.58
Age (Ma	4.34	4.34	4.34	4.34	4.34	4.34	4.34
Major Elements (wt. %)							
SiO2	73.91	73.95	73.99	74.05	74.24	74.24	74.41
TiO2	0.26	0.33	0.29	0.25	0.25	0.25	0.34
Al2O3	14.25	14.27	14.18	14.25	14.15	14.15	13.99
FeO*	2.00	2.01	2.16	2.15	2.03	2.03	2.00
MnO	0.18	0.22	0.18	0.13	0.10	0.10	0.23
MgO	0.38	0.43	0.38	0.34	0.35	0.35	0.41
CaO	1.86	1.80	1.93	1.82	1.86	1.86	1.76
Na2O	3.82	3.53	3.86	3.45	3.81	3.81	3.37
K2O	3.35	3.46	3.05	3.56	3.21	3.21	3.50
P2O5	0.00	0.00	0.00	0.00	0.00	0.00	0.00
Total	100.00	100.00	100.00	100.00	100.00	100.00	100.00
Trace Elements (ppm)							
Sc	11.2	13.7				11.3	11.7
Ni		0.30					0.18
Rb	29.5	32.8				41.3	31.6
Sr	168	181				157	171
Y	41.6	48.3				41.4	45.9
Zr	205	251				199	218
Nb	7.97	9.32				8.42	8.69
Cs	0.80	0.61				0.88	0.65
Ba	244	261				239	257
La	16.6	17.9				16.5	17.5
Ce	41.3	41.7				42.9	42.3
Pr	5.42	5.62				5.55	6.07
Nd	24.3	26.7				23.8	24.7
Sm	6.67	6.64				6.27	6.29
Eu	1.73	1.84				1.55	1.63
Gd	6.88	7.45				6.52	6.58
Tb	1.03	1.13				1.13	1.14
Dy	7.19	8.48				6.89	8.08
Ho	1.62	1.62				1.46	1.66
Er	4.40	5.70				4.93	5.10
Tm	0.70	0.70				0.61	0.80
Yb	4.97	5.91				4.98	5.21
Lu	0.72	0.79				0.79	0.99
Hf	5.18	6.46				5.26	5.51
Ta	0.58	0.81				0.60	0.66
Pb	4.82	4.85				4.91	4.82
Th	2.39	2.94				2.61	2.38
U	0.96	1.00				0.85	0.99

Table 1: Site U1437 glass chemistry

Interval	U1437D-30R-5-129/132						
ID	D-30R-5a_glass10	D-30R-5a_glass11	D-30R-5a_glass12	D-30R-5a_glass13	D-30R-5a_glass14	D-30R-5a_glass15	D-30R-5a_glass16
Depth (mbsf)	705.58	705.58	705.58	705.58	705.58	705.58	705.58
Age (Ma	4.34	4.34	4.34	4.34	4.34	4.34	4.34
Major Elements (wt. %)							
SiO2	74.42	74.45	74.60	74.61	74.68	74.76	74.82
TiO2	0.25	0.31	0.32	0.31	0.29	0.27	0.29
Al2O3	14.05	14.15	14.17	14.13	14.21	14.26	13.88
FeO*	1.91	2.04	1.85	1.97	1.87	1.88	2.07
MnO	0.07	0.19	0.12	0.14	0.16	0.20	0.09
MgO	0.37	0.36	0.39	0.38	0.38	0.37	0.38
CaO	1.90	1.96	1.77	1.13	1.78	1.79	1.96
Na2O	4.17	3.19	4.49	4.05	4.30	4.12	3.38
K2O	2.87	3.36	2.29	3.28	2.32	2.35	3.10
P2O5	0.00	0.00	0.00	0.00	0.00	0.00	0.03
Total	100.00	100.00	100.00	100.00	100.00	100.00	100.00
Trace Elements (ppm)							
Sc					10.9		
Ni							
Rb					31.8		
Sr					161		
Y					41.1		
Zr					206		
Nb					8.73		
Cs					0.69		
Ba					245		
La					16.5		
Ce					41.9		
Pr					5.69		
Nd					24.3		
Sm					6.44		
Eu					1.64		
Gd					5.83		
Tb					1.05		
Dy					7.22		
Ho					1.45		
Er					4.29		
Tm					0.67		
Yb					4.90		
Lu					0.69		
Hf					5.36		
Ta					0.58		
Pb					4.86		
Th					2.45		
U					0.95		

Table 1: Site U1437 glass chemistry

Interval	U1437D-30R-5-129/132						
ID	D-30R-5a_glass17	D-30R-5a_glass18	D-30R-5a_glass19	D-30R-5a_glass20	D-30R-5a_glass21	D-30R-5a_glass22	D-30R-5a_glass23
Depth (mbsf)	705.58	705.58	705.58	705.58	705.58	705.58	705.58
Age (Ma	4.34	4.34	4.34	4.34	4.34	4.34	4.34
Major Elements (wt. %)							
SiO2	74.95	74.95	75.00	75.15	75.16	75.20	75.36
TiO2	0.28	0.28	0.33	0.33	0.33	0.33	0.31
Al2O3	14.21	14.21	14.27	14.09	14.06	14.02	14.76
FeO*	1.88	1.88	2.04	2.15	2.13	1.76	1.89
MnO	0.13	0.13	0.18	0.17	0.08	0.10	0.19
MgO	0.37	0.37	0.40	0.43	0.42	0.35	0.36
CaO	1.61	1.61	1.15	1.99	1.89	1.85	2.04
Na2O	3.13	3.13	3.45	2.65	2.88	3.12	1.76
K2O	3.45	3.45	3.17	2.99	2.97	3.24	3.33
P2O5	0.00	0.00	0.00	0.05	0.09	0.03	0.00
Total	100.00	100.00	100.00	100.00	100.00	100.00	100.00
Trace Elements (ppm)							
Sc			12.6				
Ni							
Rb			57.3				
Sr			150				
Y			47.3				
Zr			231				
Nb			8.92				
Cs			3.21				
Ba			143				
La			18.5				
Ce			44.0				
Pr			5.88				
Nd			26.7				
Sm			6.57				
Eu			1.90				
Gd			7.48				
Tb			1.17				
Dy			7.62				
Ho			1.73				
Er			5.44				
Tm			0.77				
Yb			5.28				
Lu			0.88				
Hf			5.91				
Ta			0.65				
Pb			4.64				
Th			2.64				
U			1.07				

Table 1: Site U1437 glass chemistry

Interval	U1437D-30R-5-129/132						
ID	D-30R-5a_glass24	D-30R-5a_glass25	D-30R-5a_glass26	D-30R-5a_glass27	D-30R-5a_glass28	D-30R-5a_glass29	D-30R-5a_glass30
Depth (mbsf)	705.58	705.58	705.58	705.58	705.58	705.58	705.58
Age (Ma	4.34	4.34	4.34	4.34	4.34	4.34	4.34
Major Elements (wt. %)							
SiO2	75.39	75.39	75.39	75.39	75.40	75.44	75.48
TiO2	0.35	0.27	0.32	0.33	0.31	0.34	0.28
Al2O3	14.42	14.12	14.33	14.16	14.20	13.86	14.31
FeO*	2.12	2.07	1.96	2.16	2.41	1.95	1.98
MnO	0.22	0.11	0.16	0.09	0.15	0.14	0.14
MgO	0.42	0.36	0.36	0.38	0.38	0.35	0.41
CaO	1.17	1.98	1.91	1.96	1.72	1.83	1.96
Na2O	2.85	2.73	2.62	2.57	2.12	2.80	2.51
K2O	3.06	2.94	2.92	2.91	3.31	3.21	2.85
P2O5	0.00	0.04	0.03	0.04	0.00	0.08	0.08
Total	100.00	100.00	100.00	100.00	100.00	100.00	100.00
Trace Elements (ppm)							
Sc							
Ni							
Rb							
Sr							
Y							
Zr							
Nb							
Cs							
Ba							
La							
Ce							
Pr							
Nd							
Sm							
Eu							
Gd							
Tb							
Dy							
Ho							
Er							
Tm							
Yb							
Lu							
Hf							
Ta							
Pb							
Th							
U							

Table 1: Site U1437 glass chemistry

Interval	U1437D-30R-5-129/132						
ID	D-30R-5a_glass31	D-30R-5a_glass32	D-30R-5a_glass33	D-30R-5a_glass34	D-30R-5a_glass35	D-30R-5a_glass36	D-30R-5a_glass37
Depth (mbsf)	705.58	705.58	705.58	705.58	705.58	705.58	705.58
Age (Ma	4.34	4.34	4.34	4.34	4.34	4.34	4.34
Major Elements (wt. %)							
SiO2	75.48	75.59	75.66	75.66	75.70	75.72	75.73
TiO2	0.30	0.31	0.30	0.28	0.30	0.24	0.30
Al2O3	14.11	14.06	13.89	13.99	13.91	14.16	13.96
FeO*	1.99	1.93	2.17	1.83	1.82	2.01	1.98
MnO	0.18	0.09	0.13	0.13	0.14	0.16	0.12
MgO	0.38	0.36	0.46	0.38	0.37	0.31	0.40
CaO	1.96	1.82	1.88	1.77	1.80	1.75	1.96
Na2O	2.63	3.31	2.59	3.29	3.07	2.31	2.56
K2O	2.95	2.46	2.88	2.63	2.83	3.35	2.91
P2O5	0.01	0.07	0.03	0.04	0.06	0.00	0.07
Total	100.00	100.00	100.00	100.00	100.00	100.00	100.00
Trace Elements (ppm)							
Sc						16.5	
Ni						2.06	
Rb						36.6	
Sr						151	
Y						35.2	
Zr						316	
Nb						7.91	
Cs						0.78	
Ba						303	
La						14.0	
Ce						35.6	
Pr						4.29	
Nd						19.4	
Sm						4.84	
Eu						1.33	
Gd						5.14	
Tb						0.99	
Dy						6.09	
Ho						1.42	
Er						4.09	
Tm						0.66	
Yb						4.47	
Lu						0.60	
Hf						8.94	
Ta							
Pb						17.00	
Th						3.65	
U						0.93	

Table 1: Site U1437 glass chemistry

Interval	U1437D-30R-5-129/132					U1437D-30R-6-10/11	
ID	D-30R-5a_glass38	D-30R-5a_glass39	D-30R-5a_glass40	D-30R-5a_glass41	D-30R-5a_glass42	D-30R-6a_glass1	D-30R-6a_glass2
Depth (mbsf)	705.58	705.58	705.58	705.58	705.58	705.74	705.74
Age (Ma	4.34	4.34	4.34	4.34	4.34	4.34	4.34
Major Elements (wt. %)							
SiO_2	75.76	75.84	75.97	76.04	76.16	73.52	73.77
TiO_2	0.31	0.31	0.34	0.18	0.30	0.31	0.27
Al_2O_3	14.58	14.03	13.68	14.12	14.40	14.12	14.30
FeO*	1.79	1.87	1.86	1.61	1.69	2.02	1.98
MnO	0.16	0.10	0.12	0.16	0.12	0.23	0.18
MgO	0.32	0.38	0.35	0.23	0.28	0.36	0.36
CaO	1.80	1.76	1.71	1.77	1.56	1.87	1.83
Na_2O	1.91	2.77	2.97	2.50	2.05	4.06	3.80
K_2O	3.39	2.92	2.95	3.40	3.45	3.51	3.52
P_2O_5	0.00	0.03	0.05	0.00	0.00	0.00	0.00
Total	100.00	100.00	100.00	100.00	100.00	100.00	100.00
Trace Elements (ppm)							
Sc	14.2						12.1
Ni	1.60						0.08
Rb	37.9						31.1
Sr	162						164
Y	53.5						46.4
Zr	278						225
Nb	8.93						8.55
Cs	0.68						0.71
Ba	311						247
La	20.3						17.6
Ce	47.9						43.4
Pr	6.26						5.71
Nd	28.3						26.7
Sm	8.12						6.18
Eu	2.62						1.68
Gd	8.35						7.27
Tb	1.47						1.18
Dy	9.32						8.34
Ho	2.05						1.75
Er	5.95						4.77
Tm	0.98						0.84
Yb	5.23						5.24
Lu	0.82						0.84
Hf	8.19						6.32
Ta							0.63
Pb	16.70						5.49
Th	4.30						2.54
U	0.95						0.89

Table 1: Site U1437 glass chemistry

Interval	U1437D-30R-6-10/11						
ID	D-30R-6a_glass3	D-30R-6a_glass4	D-30R-6a_glass5	D-30R-6a_glass6	D-30R-6a_glass7	D-30R-6a_glass9	D-30R-6a_glass10
Depth (mbsf)	705.74	705.74	705.74	705.74	705.74	705.74	705.74
Age (Ma	4.34	4.34	4.34	4.34	4.34	4.34	4.34
Major Elements (wt. %)							
SiO2	73.90	73.90	73.97	73.98	74.04	74.17	74.21
TiO2	0.29	0.29	0.26	0.35	0.23	0.29	0.26
Al2O3	14.32	14.25	14.36	14.31	14.40	14.25	14.25
FeO*	2.00	2.14	1.97	2.09	1.93	2.09	1.94
MnO	0.19	0.14	0.17	0.11	0.14	0.16	0.21
MgO	0.40	0.40	0.43	0.40	0.46	0.42	0.33
CaO	1.67	1.94	1.79	1.39	1.91	1.95	1.73
Na2O	4.19	3.42	4.19	3.79	4.19	3.18	3.80
K2O	3.02	3.51	2.86	3.58	2.70	3.50	3.27
P2O5	0.00	0.00	0.00	0.00	0.00	0.00	0.00
Total	100.00	100.00	100.00	100.00	100.00	100.00	100.00
Trace Elements (ppm)							
Sc			11.9			11.8	
Ni						0.14	
Rb			31.1			34.5	
Sr			167			168	
Y			47.8			47.6	
Zr			227			227	
Nb			8.66			8.65	
Cs			0.68			0.71	
Ba			250			250	
La			17.6			17.6	
Ce			42.5			42.0	
Pr			5.83			5.64	
Nd			24.8			26.0	
Sm			6.64			6.65	
Eu			1.73			1.74	
Gd			7.02			7.32	
Tb			1.28			1.17	
Dy			8.17			7.91	
Ho			1.61			1.77	
Er			5.12			5.66	
Tm			0.80			0.79	
Yb			5.61			5.43	
Lu			0.85			0.77	
Hf			6.18			6.17	
Ta			0.53			0.55	
Pb			4.34			4.90	
Th			2.67			2.64	
U			1.01			0.96	

Table 1: Site U1437 glass chemistry

Interval	U1437D-30R-6-10/11						
ID	D-30R-6a_glass11	D-30R-6a_glass12	D-30R-6a_glass13	D-30R-6a_glass14	D-30R-6a_glass15	D-30R-6a_glass16	D-30R-6a_glass17
Depth (mbsf)	705.74	705.74	705.74	705.74	705.74	705.74	705.74
Age (Ma	4.34	4.34	4.34	4.34	4.34	4.34	4.34
Major Elements (wt. %)							
SiO2	74.29	74.37	74.43	74.60	74.61	74.62	74.68
TiO2	0.27	0.27	0.28	0.26	0.24	0.25	0.28
Al2O3	14.17	14.09	14.26	14.24	14.32	14.26	14.33
FeO*	1.96	1.98	2.04	2.00	2.06	1.95	1.96
MnO	0.19	0.17	0.18	0.16	0.19	0.18	0.17
MgO	0.35	0.37	0.43	0.35	0.39	0.36	0.39
CaO	1.75	1.76	1.95	1.73	1.84	1.70	1.87
Na2O	3.68	3.56	2.95	3.31	3.00	3.32	3.08
K2O	3.35	3.44	3.49	3.34	3.36	3.37	3.24
P2O5	0.00	0.00	0.00	0.00	0.00	0.00	0.00
Total	100.00	100.00	100.00	100.00	100.00	100.00	100.00
Trace Elements (ppm)							
Sc	11.5			11.6			13.9
Ni	0.10			0.16			2.26
Rb	30.7			58.1			41.3
Sr	163			172			166
Y	44.8			46.7			48.5
Zr	213			223			271
Nb	8.46			8.66			7.97
Cs	0.70			0.72			1.17
Ba	242			260			272
La	17.4			17.2			18.1
Ce	41.8			43.7			46.7
Pr	5.57			5.84			5.48
Nd	25.6			26.2			26.9
Sm	6.55			6.93			7.03
Eu	1.67			1.66			1.56
Gd	6.85			7.11			6.29
Tb	1.11			1.18			1.27
Dy	7.39			7.85			7.65
Ho	1.60			1.61			1.96
Er	5.10			5.34			5.73
Tm	0.79			0.69			0.89
Yb	5.27			5.20			5.87
Lu	0.73			0.85			0.87
Hf	6.00			6.25			7.91
Ta	0.58			0.69			1.10
Pb	4.92			5.19			7.90
Th	2.54			2.91			3.51
U	1.06			1.04			1.09

Table 1: Site U1437 glass chemistry

Interval	U1437D-30R-6-10/11						
ID	D-30R-6a_glass18	D-30R-6a_glass19	D-30R-6a_glass20	D-30R-6a_glass21	D-30R-6a_glass22	D-30R-6a_glass23	D-30R-6a_glass24
Depth (mbsf)	705.74	705.74	705.74	705.74	705.74	705.74	705.74
Age (Ma	4.34	4.34	4.34	4.34	4.34	4.34	4.34
Major Elements (wt. %)							
SiO2	74.93	75.29	75.59	75.59	75.88	76.02	76.07
TiO2	0.35	0.34	0.35	0.32	0.35	0.31	0.32
Al2O3	14.46	14.00	14.07	14.04	14.61	13.86	14.60
FeO*	2.04	2.16	1.94	2.02	1.98	1.89	2.01
MnO	0.15	0.07	0.10	0.14	0.19	0.13	0.18
MgO	0.40	0.41	0.40	0.41	0.39	0.46	0.40
CaO	1.60	1.93	1.94	1.94	1.82	1.94	1.86
Na2O	3.04	2.71	2.53	2.52	2.30	2.44	2.01
K2O	3.02	3.09	3.01	3.00	2.47	2.89	2.53
P2O5	0.00	0.01	0.07	0.03	0.00	0.05	0.00
Total	100.00	100.00	100.00	100.00	100.00	100.00	100.00
Trace Elements (ppm)							
Sc	11.7						11.7
Ni							
Rb	31.4						43.0
Sr	164						168
Y	46.3						45.5
Zr	222						221
Nb	8.48						8.62
Cs	0.71						1.11
Ba	261						222
La	17.8						17.4
Ce	44.8						43.4
Pr	6.14						5.98
Nd	26.1						25.0
Sm	6.88						6.20
Eu	1.90						1.71
Gd	7.98						7.19
Tb	1.20						1.07
Dy	9.08						8.01
Ho	1.69						1.61
Er	4.91						4.97
Tm	0.75						0.80
Yb	5.63						5.39
Lu	0.84						0.76
Hf	5.45						6.45
Ta	0.57						0.48
Pb	5.26						4.60
Th	2.61						2.82
U	1.06						0.99

Table 1: Site U1437 glass chemistry

Interval	U1437D-30R 6-10/11	U1437D-30R-6-33/34					
ID	D-30R-6a_glass25	D-30R-6b_glass1	D-30R-6b_glass2	D-30R-6b_glass3	D-30R-6b_glass4	D-30R-6b_glass5	D-30R-6b_glass6
Depth (mbsf)	705.74	705.97	705.97	705.97	705.97	705.97	705.97
Age (Ma	4.34	4.34	4.34	4.34	4.34	4.34	4.34
Major Elements (wt. %)							
SiO2	76.13	73.57	73.91	74.04	74.35	74.44	74.50
TiO2	0.33	0.38	0.39	0.36	0.29	0.25	0.23
Al2O3	14.42	14.40	14.20	14.33	14.45	14.36	14.39
FeO*	2.15	3.07	2.08	2.01	1.87	1.76	1.89
MnO	0.16	0.18	0.21	0.20	0.14	0.17	0.16
MgO	0.44	0.38	0.34	0.38	0.40	0.38	0.38
CaO	1.89	2.06	1.96	1.83	1.83	1.84	1.78
Na2O	2.48	2.84	3.24	3.22	3.17	3.20	3.11
K2O	1.95	3.13	3.66	3.63	3.51	3.62	3.57
P2O5	0.05	0.00	0.00	0.00	0.00	0.00	0.00
Total	100.00	100.00	100.00	100.00	100.00	100.00	100.00
Trace Elements (ppm)							
Sc				11.4			12.1
Ni							
Rb				32.0			32.4
Sr				166			170
Y				45.3			46.8
Zr				217			225
Nb				8.68			8.73
Cs				0.71			0.72
Ba				257			252
La				17.7			17.6
Ce				42.5			41.7
Pr				5.83			5.95
Nd				26.1			26.5
Sm				6.11			6.71
Eu				1.72			1.68
Gd				7.41			7.68
Tb				1.11			1.14
Dy				7.86			8.29
Ho				1.68			1.59
Er				5.27			5.25
Tm				0.74			0.74
Yb				5.40			5.25
Lu				0.85			0.86
Hf				6.14			5.65
Ta				0.65			0.67
Pb				4.71			5.10
Th				2.40			2.76
U				0.92			0.85

Table 1: Site U1437 glass chemistry

Interval	U1437D-30R-6-33/34						
ID	D-30R-6b_glass7	D-30R-6b_glass8	D-30R-6b_glass9	D-30R-6b_glass10	D-30R-6b_glass11	D-30R-6b_glass12	D-30R-6b_glass13
Depth (mbsf)	705.97	705.97	705.97	705.97	705.97	705.97	705.97
Age (Ma	4.34	4.34	4.34	4.34	4.34	4.34	4.34
Major Elements (wt. %)							
SiO2	74.61	74.63	74.64	74.70	74.91	74.91	75.29
TiO2	0.30	0.27	0.27	0.27	0.34	0.34	0.33
Al2O3	14.41	14.49	14.35	14.53	14.84	14.84	14.28
FeO*	1.89	2.00	2.01	2.03	2.97	2.97	1.73
MnO	0.18	0.23	0.16	0.24	0.18	0.18	0.17
MgO	0.40	0.33	0.40	0.36	0.41	0.41	0.31
CaO	1.74	1.73	1.81	1.77	2.08	2.08	1.93
Na2O	3.06	2.92	3.03	2.84	1.97	1.97	2.87
K2O	3.42	3.39	3.33	3.27	2.29	2.29	3.05
P2O5	0.00	0.00	0.00	0.00	0.00	0.00	0.04
Total	100.00	100.00	100.00	100.00	100.00	100.00	100.00
Trace Elements (ppm)							
Sc			12.5	13.3	16.3	15.3	
Ni			0.27	1.46	3.16	0.50	
Rb			57.2	58.3	33.7	33.6	
Sr			174	180	167	178	
Y			50.2	52.0	50.6	53.9	
Zr			239	244	286	281	
Nb			8.43	9.69	9.37	9.33	
Cs			0.82	1.60	0.76	0.68	
Ba			256	299	253	238	
La			18.4	18.8	17.3	18.9	
Ce			43.8	44.1	40.0	42.6	
Pr			6.01	6.41	5.55	5.99	
Nd			27.3	29.1	25.6	27.4	
Sm			7.40	7.82	7.76	7.29	
Eu			1.69	1.99	1.80	1.95	
Gd			7.84	7.73	7.65	9.27	
Tb			1.39	1.46	1.25	1.35	
Dy			8.90	8.43	9.69	10.00	
Ho			1.81	2.02	1.80	1.90	
Er			5.77	5.18	5.76	6.41	
Tm			0.87	0.82	0.81	0.94	
Yb			5.56	5.82	5.63	6.24	
Lu			0.89	1.07	0.89	1.05	
Hf			6.06	6.95	7.71	8.32	
Ta			0.67	0.73	9.79	0.81	
Pb			5.50	6.27	10.32	5.44	
Th			2.79	3.07	2.56	2.52	
U			0.84	1.00	0.84	0.85	

Table 1: Site U1437 glass chemistry

Interval	U1437D-30R-6-33/34			U1437D-30R-6-51/52			
ID	D-30R-6b_glass14	D-30R-6b_glass15	D-30R-6b_glass16	D-30R-6c_glass1	D-30R-6c_glass2	D-30R-6c_glass3	D-30R-6c_glass4
Depth (mbsf)	705.97	705.97	705.97	706.15	706.15	706.15	706.15
Age (Ma	4.34	4.34	4.34	4.34	4.34	4.34	4.34
Major Elements (wt. %)							
SiO_2	75.31	75.50	75.76	75.30	75.39	75.39	75.39
TiO_2	0.30	0.32	0.36	0.33	0.34	0.34	0.34
Al_2O_3	14.09	14.10	14.17	13.96	14.72	14.72	14.72
FeO*	1.90	1.97	2.03	2.25	2.05	2.05	2.05
MnO	0.21	0.08	0.11	0.18	0.24	0.24	0.24
MgO	0.29	0.42	0.42	0.38	0.43	0.43	0.43
CaO	1.84	1.98	1.93	1.89	1.92	1.92	1.92
Na_2O	2.84	2.54	2.43	2.63	2.29	2.29	2.29
K_2O	3.22	3.06	2.78	3.02	2.62	2.62	2.62
P_2O_5	0.02	0.03	0.01	0.04	0.00	0.00	0.00
Total	100.00	100.00	100.00	100.00	100.00	100.00	100.00
Trace Elements (ppm)							
Sc					12.2	12.0	
Ni							
Rb					32.0	34.6	
Sr					173	173	
Y					48.7	48.4	
Zr					235	234	
Nb					9.14	9.06	
Cs					0.74	0.86	
Ba					253	283	
La					18.4	18.4	
Ce					42.9	43.8	
Pr					6.00	5.92	
Nd					26.8	25.9	
Sm					6.43	6.90	
Eu					1.77	1.72	
Gd					7.60	7.58	
Tb					1.16	1.18	
Dy					7.63	7.97	
Ho					1.74	1.64	
Er					5.54	5.70	
Tm					0.79	0.84	
Yb					5.61	6.16	
Lu					0.87	0.92	
Hf					6.32	6.20	
Ta					0.63	0.67	
Pb					5.38	5.42	
Th					2.56	2.96	
U					0.94	0.89	

Table 1: Site U1437 glass chemistry

Interval	U1437D-30R-6-51/52			U1437D-30R-6-62/63			
ID	D-30R-6c_glass5	D-30R-6c_glass6	D-30R-6c_glass7	D-30R-6d_glass1	D-30R-6d_glass2	D-30R-6d_glass3	D-30R-6d_glass4
Depth (mbsf)	706.15	706.15	706.15	706.26	706.26	706.26	706.26
Age (Ma	4.34	4.34	4.34	4.34	4.34	4.34	4.34
Major Elements (wt. %)							
SiO2	75.50	75.60	75.82	73.24	73.43	73.51	75.25
TiO2	0.30	0.34	0.31	0.26	0.31	0.35	0.31
Al2O3	13.82	13.91	14.04	14.47	14.26	14.10	14.45
FeO*	1.80	2.04	2.17	2.20	1.94	2.17	2.01
MnO	0.12	0.14	0.00	0.20	0.24	0.23	0.12
MgO	0.40	0.39	0.41	0.36	0.45	0.41	0.44
CaO	1.81	1.98	1.95	1.79	1.89	1.92	1.96
Na2O	2.99	2.61	2.39	3.89	3.97	3.40	2.52
K2O	3.22	3.01	2.85	3.59	3.51	3.91	2.87
P2O5	0.03	0.00	0.06	0.00	0.00	0.00	0.07
Total	100.00	100.00	100.00	100.00	100.00	100.00	100.00
Trace Elements (ppm)							
Sc							
Ni							
Rb							
Sr							
Y							
Zr							
Nb							
Cs							
Ba							
La							
Ce							
Pr							
Nd							
Sm							
Eu							
Gd							
Tb							
Dy							
Ho							
Er							
Tm							
Yb							
Lu							
Hf							
Ta							
Pb							
Th							
U							

Table 1: Site U1437 glass chemistry

Interval	U1437D-30R-6-62/63				U1437D-31R-3-41/43		
ID	D-30R-6d_glass5	D-30R-6d_glass6	D-30R-6d_glass7	D-30R-6d_glass8	D-31R-3a_glass1	D-31R-3a_glass2	D-31R-3a_glass3
Depth (mbsf)	706.26	706.26	706.26	706.26	712.07	712.07	712.07
Age (Ma	4.34	4.34	4.34	4.34	4.36	4.36	4.36
Major Elements (wt. %)							
SiO2	75.46	75.51	75.70	75.77	73.99	74.29	74.30
TiO2	0.36	0.33	0.31	0.29	0.37	0.38	0.43
Al2O3	14.24	14.23	14.20	14.45	14.48	14.47	14.49
FeO*	2.14	1.95	2.05	2.15	2.93	2.95	3.15
MnO	0.14	0.08	0.22	0.15	0.17	0.16	0.12
MgO	0.39	0.37	0.41	0.44	0.40	0.44	0.41
CaO	2.00	1.94	1.94	1.74	2.11	2.18	2.19
Na2O	2.39	2.48	2.22	2.25	2.66	2.30	2.16
K2O	2.87	3.04	2.85	2.76	2.84	2.78	2.70
P2O5	0.01	0.05	0.11	0.00	0.04	0.04	0.05
Total	100.00	100.00	100.00	100.00	100.00	100.00	100.00
Trace Elements (ppm)							
Sc							
Ni							
Rb							
Sr							
Y							
Zr							
Nb							
Cs							
Ba							
La							
Ce							
Pr							
Nd							
Sm							
Eu							
Gd							
Tb							
Dy							
Ho							
Er							
Tm							
Yb							
Lu							
Hf							
Ta							
Pb							
Th							
U							

Table 1: Site U1437 glass chemistry

Interval	U1437D-31r-3-82/83				U1437D-31R-4-79/81		
ID	D-31R-3b_glass1	D-31R-3b_glass2	D-31R-3b_glass3	D-31R-3b_glass4	D-31R-4a_glass1	D-31R-4a_glass2	D-31R-4a_glass3
Depth (mbsf)	712.47	712.47	712.47	712.47	713.46	713.46	713.46
Age (Ma	4.37	4.37	4.37	4.37	4.37	4.37	4.37
Major Elements (wt. %							
SiO2	73.90	74.06	74.20	75.24	71.45	71.97	72.08
TiO2	0.36	0.37	0.39	0.24	0.38	0.36	0.34
Al2O3	14.29	14.38	14.28	13.75	14.78	14.60	14.68
FeO*	3.27	2.96	3.04	3.47	3.26	2.98	3.15
MnO	0.16	0.19	0.16	0.05	0.27	0.18	0.14
MgO	0.38	0.39	0.46	0.17	0.53	0.48	0.45
CaO	2.13	2.13	2.13	1.80	2.10	2.07	2.18
Na2O	2.60	2.64	2.50	2.30	3.72	4.22	4.41
K2O	2.79	2.80	2.80	2.94	3.51	3.15	2.57
P2O5	0.11	0.08	0.04	0.04	0.00	0.00	0.00
Total	100.00	100.00	100.00	100.00	100.00	100.00	100.00
Trace Elements (ppm)							
Sc	2514.1	2464.8	2407.1	2454.3			
Ni	0.33	0.12	0.15	0.47			
Rb	49.1	34.0	33.2	56.4			
Sr	162	171	163	146			
Y	48.7	56.2	52.2	48.6			
Zr	230	272	260	233			
Nb	9.26	9.42	9.31	8.85			
Cs	2.27	0.75	0.74	1.14			
Ba	87	264	249	190			
La	17.2	19.5	18.6	16.9			
Ce	39.2	42.6	41.2	39.9			
Pr	5.13	5.90	5.83	5.43			
Nd	24.5	28.0	26.3	24.7			
Sm	5.99	7.94	7.74	6.77			
Eu	1.76	2.04	2.02	1.91			
Gd	6.71	7.78	7.49	6.82			
Tb	1.21	1.36	1.30	1.16			
Dy	7.37	9.42	9.25	8.00			
Ho	1.84	2.07	2.02	1.67			
Er	5.17	6.26	5.86	4.86			
Tm	0.82	0.85	0.89	0.81			
Yb	5.66	6.48	6.68	5.67			
Lu	0.96	1.02	1.03	0.90			
Hf	5.89	7.09	6.57	6.42			
Ta	0.52	0.67	0.56	0.52			
Pb	5.63	7.15	7.40	5.81			
Th	2.56	3.05	2.90	2.61			
U	0.92	0.91	0.92	0.88			

Table 1: Site U1437 glass chemistry

Interval	U1437D-31R-4-79/81						
ID	D-31R-4a_glass4	D-31R-4a_glass5	D-31R-4a_glass6	D-31R-4a_glass7	D-31R-4a_glass8	D-31R-4a_glass9	D-31R-4a_glass10
Depth (mbsf)	713.46	713.46	713.46	713.46	713.46	713.46	713.46
Age (Ma	4.37	4.37	4.37	4.37	4.37	4.37	4.37
Major Elements (wt. %)							
SiO2	72.62	72.92	73.05	73.20	73.20	73.45	74.09
TiO2	0.34	0.32	0.41	0.39	0.32	0.38	0.37
Al2O3	14.55	14.44	14.70	14.10	14.42	14.46	13.92
FeO*	2.82	3.01	3.09	2.84	2.68	3.28	2.78
MnO	0.20	0.21	0.13	0.16	0.17	0.13	0.17
MgO	0.42	0.39	0.35	0.48	0.42	0.44	0.39
CaO	1.95	1.85	1.16	2.05	1.93	2.25	1.94
Na2O	3.73	4.01	4.18	3.44	3.74	2.73	3.23
K2O	3.37	2.85	2.85	3.29	3.13	2.86	3.06
P2O5	0.00	0.00	0.08	0.06	0.00	0.02	0.05
Total	100.00	100.00	100.00	100.00	100.00	100.00	100.00
Trace Elements (ppm)							
Sc							
Ni							
Rb							
Sr							
Y							
Zr							
Nb							
Cs							
Ba							
La							
Ce							
Pr							
Nd							
Sm							
Eu							
Gd							
Tb							
Dy							
Ho							
Er							
Tm							
Yb							
Lu							
Hf							
Ta							
Pb							
Th							
U							

Table 1: Site U1437 glass chemistry

Interval	U1437D-31R-4-79/81			U1437D-31r-4-81/82			
ID	D-31R-4a_glass11	D-31R-4a_glass12	D-31R-4a_glass13	D-31R-4b_glass2	D-31R-4b_glass3	D-31R-4b_glass4	D-31R-4b_glass5
Depth (mbsf)	713.46	713.46	713.46	713.48	713.48	713.48	713.48
Age (Ma	4.37	4.37	4.37	4.37	4.37	4.37	4.37
Major Elements (wt. %)							
SiO2	74.92	74.95	75.44	72.89	73.25	73.32	73.36
TiO2	0.37	0.42	0.40	0.35	0.42	0.40	0.42
Al2O3	14.36	14.18	14.62	14.66	14.69	14.79	14.74
FeO*	2.83	2.01	2.86	3.06	3.10	2.98	2.95
MnO	0.16	0.13	0.13	0.22	0.22	0.22	0.21
MgO	0.45	0.30	0.44	0.44	0.49	0.46	0.49
CaO	1.14	0.94	1.08	2.20	2.25	2.22	2.24
Na2O	3.31	4.41	2.81	3.24	2.66	2.63	2.63
K2O	2.37	2.56	2.17	2.85	2.85	2.88	2.90
P2O5	0.09	0.10	0.07	0.10	0.07	0.09	0.07
Total	100.00	100.00	100.00	100.00	100.00	100.00	100.00
Trace Elements (ppm)							
Sc					2544.1		2825.5
Ni					0.16		6.29
Rb					34.1		42.8
Sr					141		170
Y					42.3		48.3
Zr					197		228
Nb					8.56		10.09
Cs					0.79		1.72
Ba					189		188
La					15.6		18.1
Ce					37.3		39.9
Pr					4.74		5.41
Nd					23.2		26.1
Sm					5.70		6.62
Eu					1.67		1.92
Gd					6.41		7.21
Tb					1.11		1.19
Dy					7.34		8.52
Ho					1.55		1.84
Er					4.69		5.34
Tm					0.70		0.78
Yb					5.24		5.77
Lu					0.74		0.87
Hf					4.95		5.78
Ta					0.40		0.52
Pb					5.19		5.99
Th					2.17		2.46
U					0.93		0.78

Table 1: Site U1437 glass chemistry

Interval	U1437D-31r-4-81/82			U1437D-31R-6-29/32			
ID	D-31R-4b_glass6	D-31R-4b_glass7	D-31R-4b_glass8	D-31R-4b_glass1	D-31R-4b_glass2	D-31R-4b_glass3	D-31R-4b_glass4
Depth (mbsf)	713.48	713.48	713.48	714.98	714.98	714.98	714.98
Age (Ma	4.37	4.37	4.37	4.37	4.37	4.37	4.37
Major Elements (wt. %)							
SiO_2	73.36	73.42	73.46	72.90	73.09	73.21	73.27
TiO_2	0.42	0.40	0.46	0.51	0.44	0.49	0.49
Al_2O_3	14.74	14.87	14.79	14.82	14.74	14.78	14.78
FeO*	2.95	3.29	3.11	3.47	3.38	3.15	3.68
MnO	0.21	0.09	0.17	0.15	0.11	0.09	0.17
MgO	0.49	0.49	0.46	0.57	0.51	0.52	0.55
CaO	2.24	2.33	2.37	2.42	2.38	2.53	2.53
Na_2O	2.63	2.34	2.51	2.49	2.65	2.51	2.03
K_2O	2.90	2.68	2.64	2.63	2.63	2.63	2.44
P_2O_5	0.07	0.10	0.05	0.04	0.06	0.08	0.07
Total	100.00	100.00	100.00	100.00	100.00	100.00	100.00
Trace Elements (ppm)							
Sc			2512.6				
Ni			0.10				
Rb			47.4				
Sr			144				
Y			46.7				
Zr			224				
Nb			9.07				
Cs			1.82				
Ba			135				
La			17.1				
Ce			40.0				
Pr			5.24				
Nd			24.9				
Sm			6.88				
Eu			1.81				
Gd			7.28				
Tb			1.25				
Dy			8.18				
Ho			1.74				
Er			5.34				
Tm			0.80				
Yb			5.70				
Lu			0.86				
Hf			5.97				
Ta			0.52				
Pb			5.11				
Th			2.40				
U			0.88				

Table 2: Site U1437 Minerals, Plagioclase

Interval	U1437B-20F-2-101/102		U1437B-21F-1-93/94			U1437B-33X-1-88/88		U1437B-35x-6-6/7	U1437D-05R-2-102/103			U1437D-08R-1-68/69
ID	20f-2w 101-102_plag 3_02	20f-2w 101-102_plag 2_03	21f-1w 93-94_plag 1_01	21f-1w 93-94_plag 2_02	21f-1w 93-94_plag 3_02	33x-1w_88-89_plag 1_04	33x-1w_88-89_plag 2_04	35x-6w 6-7_plag 1_02	05r-2w 102-103_plag 2_03	05r-2w 102-103_plag 2ul_05	05r-2w 102-103_plag 3_03	08r-1w 68-69 plag 1_03
Depth (mbsf)	132.81	132.81	135.93	135.93	135.93	224.08	224.08	244.16	458.82	458.82	458.82	486.08
Major elements (wt. %)												
SiO2	51.4	51.3	51.5	46.9	48.0	49.3	59.2	59.5	57.3	52.3	58.3	58.4
Al2O3	30.0	29.7	30.1	33.7	31.8	31.9	26.0	25.4	27.1	29.5	25.6	26.0
FeO*	0.79	0.82	0.80	0.68	0.89	0.76	0.31	0.27	0.31	0.48	0.26	0.22
CaO	13.9	13.8	13.6	17.4	16.0	15.5	7.9	7.6	9.3	13.1	8.0	8.2
Na2O	3.39	3.44	3.45	1.52	2.18	2.51	6.62	6.87	6.10	3.99	6.57	6.51
K2O	0.07	0.07	0.06	0.02	0.05	0.08	0.29	0.22	0.14	0.08	0.20	0.28
Total	99.7	99.2	99.7	100.4	99.1	100.2	100.3	100.0	100.4	99.6	99.0	99.6
An	67.9	68.4	67.6	85.4	81.0	76.2	37.4	36.1	44.6	64.2	40.9	40.4

Table 2: Site U1437 Minerals, Plagioclase

Interval	U1437D-08R-1-68/69	U1437D-23R-4-56/57	U1437D-30R-5-129/132		U1437D-30R-6-10/11	U1437D-31R-4-79/81
ID	08r-1w 68-69 plag 3_01	23r-4w_56-57_plag 1_02	30r-5w_129/132_plag 2_03	30r-5w_129/132_plag 1_01	30r-6w 10-11_plag x2_04	31r-4w_79/81_plag 1_06
Depth (mbsf)	486.08	635.87	705.58	705.58	705.97	713.46
Major elements (wt. %)						
SiO2	61.5	46.8	56.2	58.1	57.4	57.4
Al2O3	23.1	33.1	27.7	26.5	26.4	26.4
FeO*	0.66	0.78	0.41	0.39	0.38	0.37
CaO	6.1	17.2	10.2	8.7	8.9	8.5
Na2O	6.83	1.60	5.53	6.29	6.16	6.35
K2O	0.57	0.08	0.14	0.17	0.17	0.22
Total	98.9	99.6	100.2	100.2	99.4	99.3
An	28.3	86.0	49.0	41.8	44.5	44.4

Table 3: Site U1437 Minerals, Pyroxenes

Interval	U1437B-20F-2-101/102								U1437B-21F-1-93/94
ID	20f-2w 101-102_pyx 1_01	20f-2w 101-102_pyx 2_01	20f-2w 101-102_pyx 3_01	20f-2w 101-102_pyx 4_01	20f-2w 101-102_pyx 5_01	20f-2w 101-102_pyx 6_01	20f-2w 101-102_pyx 7_01	20f-2w 101-102_pyx 8_01	21f-1w 93-94_pyx 2_01
Pyx	opx	opx	opx	opx	opx	opx	opx	opx	opx
Depth (mbsf)	132.81	132.81	132.81	132.81	132.81	132.81	132.81	132.81	135.93
Major elements (wt. %)									
SiO2	51.2	52.6	51.0	50.8	50.7	50.7	50.3	53.0	52.9
TiO2	0.19	0.29	0.23	0.24	0.23	0.29	0.25	0.26	0.21
Al2O3	0.51	1.33	0.71	0.71	0.62	0.53	0.71	0.99	0.75
FeO*	27.21	18.37	27.89	27.89	29.15	28.92	28.26	18.63	22.41
MnO	1.24	0.50	1.24	1.28	1.37	1.25	1.26	0.53	1.18
MgO	17.53	24.20	17.29	16.79	15.93	16.41	16.74	24.49	21.22
CaO	1.7	1.9	1.7	1.7	1.8	1.7	1.8	1.9	1.4
Total	99.6	99.3	100.0	99.5	99.7	99.8	99.3	99.8	100.0
Mg#	53.5	70.1	52.5	51.8	49.4	50.3	51.4	70.1	62.8

Table 3: Site U1437 Minerals, Pyroxenes

Interval	U1437B-21F-1-93/94		U1437B-45X-1-79/81	U1437D-08R-1-68/69					
ID Pyx	21f-1w 93-94_pyx 3_01 cpx	21f-1w 93-94_pyx 4_01 opx	45x-1w 79-80_pyx 1_01 cpx	08r-1w 68-69 pyx 1_01 opx	08r-1w 68-69 pyx 5_01 opx	08r-1w 68-69 pyx 6_01 opx	08r-1w 68-69 pyx 7_01 cpx	8R1W68.69_pyx5 cpx	8R1W68.69_pyx4 opx
Depth (mbsf)	135.93	135.93	340.385	486.08	486.08	486.08	486.08	486.08	486.08
Major elements (wt. %)									
SiO2	51.3	54.0	50.8	50.5	51.4	50.5	51.5	50.2	51.5
TiO2	0.67	0.26	0.51	0.18	0.19	0.16	0.45	0.30	0.24
Al2O3	2.47	0.96	1.85	0.52	0.59	0.39	1.40	0.91	0.53
FeO*	9.37	18.48	14.88	30.68	26.64	31.44	13.40	18.85	25.65
MnO	0.38	0.80	0.48	1.90	1.67	1.94	0.46	1.31	1.57
MgO	14.97	24.39	13.15	14.44	17.96	14.03	13.19	9.78	18.26
CaO	19.6	1.5	17.3	1.7	1.5	1.5	18.9	17.7	1.5
Total	98.7	100.4	98.9	100.0	100.0	100.0	99.3	99.0	99.2
Mg#	74.0	70.2	61.2	45.6	54.6	44.3	63.7	48.0	55.9

Table 3: Site U1437 Minerals, Pyroxenes

Interval	U1437D-08R-1-68/69	U1437D-23R-4-56/57							
ID	8R1W68.69_ pyx2	23R4_56.57_ pyx4	23R4_56.57_ pyx3	23R4_56.57_ pyx2	23R4_56.57_ pyx1	23r-4w_56-57_pyx 1_01	23r-4w_56-57_pyx 2_01	23r-4w_56-57_pyx 3_01	23r-4w_56-57_pyx 4_01
Pyx	opx	cpx	cpx	cpx	cpx	cpx	cpx	cpx	cpx
Depth (mbsf)	486.08	635.87	635.87	635.87	635.87	635.87	635.87	635.87	635.87
Major elements (wt. %)									
SiO2	51.6	50.8	51.3	51.1	51.2	51.6	51.5	51.5	51.1
TiO2	0.31	0.69	0.54	0.57	0.62	0.53	0.56	0.54	0.61
Al2O3	0.86	2.34	1.89	2.30	3.00	2.39	2.38	2.38	3.10
FeO*	23.11	8.95	9.97	9.77	8.73	10.22	12.10	10.44	9.34
MnO	1.22	0.32	0.38	0.33	0.27	0.34	0.36	0.35	0.30
MgO	20.22	14.68	14.69	14.97	14.62	14.75	15.01	14.89	14.59
CaO	1.6	20.7	20.1	20.1	20.9	19.6	17.7	19.3	20.4
Total	98.9	98.4	98.8	99.1	99.3	99.5	99.6	99.4	99.5
Mg#	60.9	74.5	72.4	73.2	74.9	72.0	68.9	71.8	73.6

Table 3: Site U1437 Minerals, Pyroxenes

Interval	U1437D-26R-4-53/54		U1437D-30R-5-129/132						
ID	26r-4w 53-54 pyx 1_01	26r-4w 53-54 pyx 3_01	30r-5w 129-132 cpx	30r-5w 129-132 opx	30r-5w 129-132 pyx1	30r-5w 129-132 pyx2	30r-5w 129-132 pyx3a	30r-5w_129/132_pyx 1_01	30r-5w_129/132_pyx 3_01
Pyx	opx	opx	cpx	opx	opx	opx	opx	opx	opx
Depth (mbsf)	681.99	681.99	705.58	705.58	705.58	705.58	705.58	705.58	705.58
Major elements (wt. %)									
SiO2	52.7	52.7	52.1	53.3	52.4	51.7	52.4	53.0	53.0
TiO2	0.29	0.11	0.20	0.15	0.15	0.13	0.13	0.14	0.14
Al2O3	1.38	0.50	1.04	0.66	0.45	0.44	0.49	0.51	0.54
FeO*	18.36	22.37	10.25	20.30	21.36	21.74	20.87	22.45	22.08
MnO	0.85	1.35	1.03	1.60	1.87	2.06	1.79	1.91	1.90
MgO	23.65	21.50	14.34	22.51	21.30	21.03	22.14	21.43	21.61
CaO	1.7	1.0	19.4	1.2	1.2	1.2	1.3	1.2	1.2
Total	99.0	99.6	98.3	99.7	98.7	98.3	99.1	100.6	100.4
Mg#	69.7	63.1	71.4	66.4	64.0	63.3	65.4	63.0	63.6

Table 3: Site U1437 Minerals, Pyroxenes

Interval	U1437D-30R-5-129/132	U1437D-30R-6-10/11				U1437D-30R-6-62/63			U1437D-31R-4-79/81
ID	30r-5w_129/132_pyx 4_01	30r-6w 10-11 pyx2	30r-6w 10-11 pyx3	30r-6w 10-11_pyx 1_01	30r-6w 10-11_pyx 2_01	30r-6w 62-63 pyx1	30r-6w 62-63 pyx2	30r-6w 62-63 pyx3-c	31r-4w 79-81 pyx1
Pyx	opx	cpx	opx	opx	opx	cpx	cpx	opx	opx
Depth (mbsf)	705.58	705.74	705.74	705.74	705.74	706.26	706.26	706.26	713.46
Major elements (wt. %)									
SiO2	52.4	51.4	52.5	52.3	52.6	50.2	52.0	51.6	50.2
TiO2	0.17	0.56	0.10	0.18	0.11	0.61	0.24	0.14	0.22
Al2O3	0.70	2.17	0.47	0.65	0.43	2.98	1.08	0.61	0.56
FeO*	23.49	10.77	21.92	22.49	22.26	9.06	9.85	22.13	26.61
MnO	1.92	0.99	1.98	1.97	1.93	0.59	0.70	1.94	1.93
MgO	20.54	13.60	21.48	21.10	21.33	13.93	14.13	21.61	18.22
CaO	1.2	19.9	1.2	1.2	1.1	20.8	20.9	1.2	1.5
Total	100.4	99.4	99.6	99.9	99.8	98.2	98.9	99.2	99.2
Mg#	60.9	69.2	63.6	62.6	63.1	73.3	71.9	63.5	55.0

Table 3: Site U1437 Minerals, Pyroxenes

Interval	U1437D-31R-4-79/81				
ID	31r-4w_79/81_pyx 1_01	31r-4w_79/81_pyx 2_01	31r-4w_79/81_pyx 3_01	31r-4w_79/81_pyx 4_01	31r-4w_79/81_pyx 5_01
Pyx	opx	cpx	opx	cpx	opx
Depth (mbsf)	713.46	713.46	713.46	713.46	713.46
Major elements (wt. %)					
SiO2	51.4	51.3	51.4	51.6	51.4
TiO2	0.19	0.46	0.19	0.30	0.19
Al2O3	0.54	2.70	0.54	1.13	0.55
FeO*	27.03	9.90	27.30	13.86	26.80
MnO	1.92	0.33	1.91	1.11	1.86
MgO	17.72	14.63	17.76	12.74	18.17
CaO	1.5	20.2	1.5	19.1	1.5
Total	100.3	99.5	100.6	99.8	100.4
Mg#	53.9	72.5	53.7	62.1	54.7

Table 4: Site U1437 Minerals, Amphibole

Interval	U1437D-30R-5-129/132		U1437D-30R-6-10/11
ID	30r-5w_129/132_amph3_05	30r-5w_129/132_amph2_04	30r-6w 10-11_amph2_01
Depth (mbsf)	705.58	705.58	705.74
Major elements (wt. %)			
SiO2	46.0	45.2	45.3
TiO2	2.00	2.17	2.24
Al2O3	8.2	9.0	9.1
FeO*	14.18	14.87	14.79
MnO	0.69	0.66	0.63
MgO	13.95	13.30	13.62
CaO	10.9	10.8	10.7
Na2O	1.88	2.01	1.95
K2O	0.20	0.23	0.24
Total	98.0	98.2	98.5
Mg#	63.7	61.5	62.2

Table 5: Site U1437 Isotopic analyses

Interval	U1437D-30R-6-54/55	U1437D-30R-6-10/12	U1437D-31R-4-79/81
ID	30R3W	30R6W	31R4W
^{87}Sr/^{86}Sr	0.703339	0.703264	0.704566
+/- 2 s.e.	19	17	17
^{143}Nd/^{144}Nd	0.513045	0.513052	0.513053
+/- 2 s.e.	7	8	8
eNd	8.05787	8.20143	8.22094
^{176}Hf/^{177}Hf	0.283186	0.283198	0.283182
+/- 2 s.e.	5	9	6
eHf	14.1804	14.6047	14.0389
^{206}Pb/^{204}Pb	18.3236	18.26382	18.26952
^{207}Pb/^{204}Pb	15.49403	15.48995	15.4937
^{208}Pb/^{204}Pb	38.1326	38.0893	38.0958

The instrumental mass bias is corrected by normalizing to ^{146}Nd/^{145}Nd = 2.0719425 (equivalent to ^{146}Nd/^{144}Nd = 0.7219), ^{86}Sr/^{88}Sr = 0.1194, and ^{179}Hf/^{177}Hf = 0.7325. Measurements of international standard glasses listed in Appendix A Table 3. 2 s.e. represents two sigma error in the sixth digit.

Epsilon Hf and Nd using chondritic uniform reservoir values (CHUR) from Bouvier et al., 2008.

Table 6: New whole rock analyses

Interval	n/a	n/a	n/a	n/a	U1437E-35R-1-110/113	U1437E-35R-2-13/16	U1437E-35R-2-48/51
ID	Dredge 12-1	Dredge 12-4	Dredge 85-1	Dredge 83-3	35r-1-110-113	34r-2-13-16	35r-2-48-51
Latitude (° N)	31.975	31.975	31.430	31.473	31.790	31.790	31.790
Longitude (° E)	139.07	139.07	139.30	139.327	139.026	139.026	139.026
Age (Ma)					12.9	12.9	12.9
Major Elements (wt. %)							
SiO_2	75.1	75.9	73.9	70.9	78.0	77.5	76.0
TiO_2	0.18	0.17	0.25	0.27	0.28	0.27	0.26
Al_2O_3	12.8	13.0	13.9	13.0	11.0	11.9	13.1
FeO^*	1.57	1.51	2.10	2.36	2.66	2.17	1.66
MnO	0.85	0.09	0.04	0.10	0.04	0.04	0.03
MgO	0.46	0.40	0.20	1.01	0.60	0.47	0.23
CaO	1.43	1.41	1.11	2.81	0.88	0.57	0.80
Na_2O	4.22	4.23	3.56	8.54	6.08	6.69	7.27
K_2O	3.33	3.17	4.95	0.98	0.36	0.31	0.60
P_2O_5	0.03	0.03	0.03	0.05	0.09	0.07	0.06
Total	100	100	100	100	100	100	100
LOI %	3.91	3.49	0.72	8.01	2.80	1.65	0.96
Trace Elements (ppm)							
Sc	4.3	4.8	9.0	10.2	7.3	5.8	5.8
Rb	46.7	45.6	170.1	9.4	1.8	1.5	2.9
Sr	97	104	104	137	8.0	6.8	8.0
Y	26.24	26.16	29.56	31.60	20.93	17.74	16.94
Zr	97	95	311	117	92	102	103
Nb	6.63	6.69	17.68	1.15	0.82	0.87	0.85
Cs	1.11	1.08	10.56	0.62	0.03	0.03	0.03
Ba	329	321	876	154	14	12	23
La	18.85	18.52	45.93	5.49	5.71	5.43	3.66
Ce	38.18	38.55	86.67	14.82	15.65	14.42	10.53
Pr	4.77	4.68	10.32	2.33	2.19	2.02	1.55
Nd	18.22	18.07	36.87	11.25	9.40	8.51	6.73
Sm	3.94	3.85	7.25	3.41	2.36	2.15	1.88
Eu	0.65	0.68	0.96	1.03	0.73	0.68	0.60
Gd	3.83	3.81	6.14	4.27	2.63	2.35	2.21
Tb	0.68	0.68	1.00	0.80	0.46	0.43	0.41
Dy	4.35	4.32	5.87	5.39	3.19	2.82	2.80
Ho	0.92	0.92	1.14	1.18	0.70	0.62	0.61
Er	2.78	2.72	3.04	3.49	2.14	1.89	1.83
Tm	0.44	0.44	0.44	0.54	0.35	0.29	0.29
Yb	2.98	2.92	2.71	3.49	2.43	2.07	2.05
Lu	0.51	0.48	0.42	0.57	0.41	0.36	0.35
Hf	3.17	3.04	8.51	3.36	2.55	2.81	2.78
Ta	0.62	0.62	1.33	0.10	0.11	0.11	0.11
Pb	4.12	4.19	29.16	3.12	2.42	3.56	1.89
Th	3.66	3.65	15.07	0.63	1.01	1.11	1.12
U	1.20	1.16	2.34	0.31	0.46	0.48	0.47

Dredged rocks come from a sampling program conducted using the R/V Moana Wave in 1995, for more details see Hochstaedter et al. (2000).

Session		JS090215					JS100215								
Major element wt. %	Lipari lit	Lipari	Lipari	Lipari	Lipari	Lipari	Lipari	Lipari	Lipari	Lipari	Lipari	Lipari	Lipari	Lipari	Lipari
SiO2	74.35	75.09	75.26	75.29	74.61	74.55	74.54	74.30	74.88	74.55	75.03	75.83	73.85	74.30	74.38
TiO2	0.1	0.06	0.07	0.09	0.09	0.12	0.10	0.09	0.09	0.12	0.08	0.07	0.08	0.07	0.09
Al2O3	12.85	13.19	13.14	13.06	12.95	13.11	13.16	13.19	13.12	13.18	13.27	13.02	13.26	13.11	12.97
FeO*	1.51	1.48	1.59	1.58	1.52	1.53	1.56	1.59	1.39	1.87	1.67	1.59	1.67	1.37	1.56
MnO	0.07	0.04	0.09	0.11	0.13	0.05	0.04	0.05	0.08	0.03	0.13	0.05	0.09	0.01	0.08
MgO	0.05	0.04	0.02	0.04	0.03	0.01	0.06	0.04	0.01	0.01	0.03	0.01	0.04	0.04	0.06
CaO	0.74	0.75	0.77	0.77	0.68	0.77	0.78	0.77	0.79	0.74	0.75	0.74	0.73	0.73	0.75
Na2O	3.93	3.61	3.71	3.64	3.77	3.63	3.62	3.66	3.59	3.64	3.57	3.82	3.80	3.61	3.89
K2O	5.11	4.94	4.97	4.95	5.02	5.04	5.03	5.06	5.00	4.98	5.01	5.00	5.04	5.10	5.01
P2O5	0.01	0.01	0.03	0.00	0.01	0.00	0.01	0.01	0.00	0.02	0.00	0.00	0.03	0.04	0.02
Total	98.72	99.21	99.65	99.53	98.82	98.81	98.90	98.76	98.95	99.14	99.54	100.13	98.59	98.37	98.80

Session		JS10021!	JS110215								
Major element wt. %	Lipari lit	Lipari	Lipari	Lipari	Lipari	Lipari	Lipari	Lipari	Lipari	Lipari	
SiO2	74.35	74.34	73.20	74.51	73.83	74.31	74.50	74.90	74.22	74.08	
TiO2	0.1	0.08	0.09	0.06	0.08	0.08	0.08	0.08	0.09	0.08	
Al2O3	12.85	13.14	13.24	13.35	13.28	13.05	13.15	13.19	13.41	13.05	
FeO*	1.51	1.59	1.40	1.51	1.76	1.33	1.53	1.54	1.47	1.41	
MnO	0.07	0.00	0.03	0.06	0.03	0.02	0.04	0.06	0.04	0.04	
MgO	0.05	0.05	0.02	0.03	0.06	0.04	0.06	0.08	0.04	0.02	
CaO	0.74	0.80	0.73	0.83	0.76	0.75	0.75	0.77	0.73	0.68	
Na2O	3.93	3.70	3.54	3.63	3.70	3.65	3.73	3.78	3.62	3.81	
K2O	5.11	5.02	5.07	5.06	5.07	5.00	4.97	5.01	5.07	5.06	
P2O5	0.01	0.00	0.00	0.00	0.01	0.01	0.00	0.02	0.01	0.01	
Total	98.72	98.72	97.32	99.04	98.58	98.23	98.80	99.43	98.70	98.24	

Session		JS090215				JS100215									
Major element wt. %	VGA lit	VGA	VGA	VGA	VGA	VGA	VGA	VGA	VGA	VGA	VGA	VGA	VGA	VGA	VGA
SiO2	**50.94**	50.45	50.81	51.41	51.28	51.91	52.03	51.57	51.62	51.66	51.67	51.28	51.66	51.25	51.52
TiO2	**4.06**	4.03	4.11	4.09	4.09	4.11	4.07	4.10	4.06	4.07	4.05	4.14	4.20	4.01	4.15
Al2O3	**12.49**	12.68	12.22	12.55	12.53	12.46	12.31	12.30	12.57	12.41	12.55	12.58	12.48	12.28	12.52
FeO*	**13.3**	13.47	13.05	13.33	13.16	13.11	12.87	13.39	13.61	13.73	13.44	13.52	13.36	13.24	13.00
MnO	**0.15**	0.26	0.20	0.25	0.12	0.21	0.18	0.20	0.18	0.20	0.25	0.20	0.15	0.15	0.16
MgO	**5.08**	5.22	5.05	5.07	5.02	5.05	4.93	5.01	4.90	4.97	5.00	5.00	5.09	5.00	4.90
CaO	**9.3**	9.10	9.34	9.33	9.26	9.35	9.19	9.30	9.22	9.32	9.30	9.21	9.42	9.39	9.30
Na2O	**2.66**	2.70	2.82	2.83	2.76	2.72	2.83	2.72	2.65	2.72	2.77	2.62	2.56	2.78	2.76
K2O	**0.82**	0.80	0.80	0.83	0.83	0.82	0.82	0.83	0.81	0.78	0.80	0.84	0.81	0.83	0.82
P2O5	**0.38**	0.34	0.37	0.34	0.40	0.39	0.38	0.38	0.40	0.35	0.35	0.35	0.37	0.31	0.40
Total	99.18	99.05	98.77	100.02	99.45	100.14	99.60	99.80	100.01	100.20	100.18	99.74	100.10	99.25	99.53

Session		JS100215		JS110215								UI 06/2016	
Major element wt. %	VGA lit	VGA	VGA	VGA	VGA	VGA	VGA	VGA	VGA	VGA	VGA	VGA	VGA
SiO2	**50.94**	51.35	51.29	50.53	51.32	50.75	50.90	51.13	51.21	50.92	51.05	51.062	50.936
TiO2	**4.06**	4.12	4.12	4.10	4.14	4.15	4.13	4.04	4.06	4.05	4.06	3.981	4.108
Al2O3	**12.49**	12.69	12.79	12.66	12.57	12.54	12.16	12.75	12.79	12.59	12.84	12.306	12.389
FeO*	**13.3**	13.31	13.43	12.94	13.40	12.96	13.18	13.27	13.82	13.50	13.43	12.859	12.925
MnO	**0.15**	0.11	0.16	0.18	0.15	0.19	0.19	0.21	0.19	0.26	0.18	0.209	0.202
MgO	**5.08**	5.10	4.97	5.00	5.07	5.10	5.06	4.94	5.05	5.20	4.91	5.223	5.314
CaO	**9.3**	9.29	9.29	9.27	9.29	9.21	9.19	9.24	9.30	9.21	9.20	9.147	9.113
Na2O	**2.66**	2.81	2.86	2.62	2.70	2.76	2.72	2.83	2.98	2.66	2.80	2.744	2.655
K2O	**0.82**	0.80	0.80	0.80	0.80	0.81	0.84	0.84	0.83	0.81	0.83	0.854	0.838
P2O5	**0.38**	0.35	0.35	0.41	0.36	0.35	0.33	0.32	0.30	0.36	0.37	0.469	0.503
Total	99.18	99.94	100.05	98.51	99.79	98.82	98.70	99.57	100.53	99.56	99.67	98.85	98.98

Session	UI 06/2016		
Major element wt. %	BCR-2G lit	BCR-2G	BCR-2G
SiO2	54.40	54.952	54.817
TiO2	2.27	2.264	2.297
Al2O3	13.40	13.531	13.473
FeO*	12.4	11.868	12.054
MnO	0.19	0.195	0.196
MgO	3.56	3.763	3.715
CaO	7.06	6.997	7.009
Na2O	3.23	2.995	3.025
K2O	1.74	1.847	1.836
P2O5	0.37	0.4	0.343
Total	98.62	98.81	98.77

Appendix A, Table 2: LA-ICP-MS standards

Session		020916 WWU							
Trace elements (ppm)	BHVO-2G lit	BHVOAA	BHVOAB	BHVOAC	BHVOAD	BHVOAE	BHVOAF	BHVO01	BHVO02
Sc	33	29.8	29.7	30.7	30.4	30.6	30.7	32.0	31.2
Ni	116	123.1	123.8	123.1	121.4	127.1	125.1	127.1	121.5
Rb	9.2	9.17	9.30	9.15	9.34	8.76	9.50	9.54	9.14
Sr	396	387.9	392.1	382.1	384.9	391.0	393.4	386.6	398.7
Y	26	21.3	22.3	22.2	22.0	22.3	23.0	23.8	22.7
Zr	170	149.2	149.6	150.5	153.2	154.1	154.9	163.5	159.4
Nb	18.3	17.75	17.27	17.13	17.45	17.31	17.91	18.00	18.11
Cs	0.2	0.13	0.09	0.09	0.09	0.07	0.10	0.08	0.09
Ba	131	127.3	125.4	129.2	129.5	128.4	130.4	131.2	131.6
La	15.2	14.49	14.48	14.42	14.48	14.71	14.92	14.98	14.96
Ce	37.6	36.0	36.4	36.3	36.2	36.7	37.4	37.0	38.0
Pr	5.35	4.96	5.11	4.88	5.07	5.24	5.16	5.15	5.14
Nd	24.5	23.0	23.5	22.8	22.7	23.5	23.6	23.6	24.2
Sm	6.1	5.54	6.06	5.59	5.87	6.01	5.58	6.22	6.2
Eu	2.07	2.01	1.92	2.00	2.08	2.04	2.03	2.08	2.11
Gd	6.16	5.61	5.26	5.64	5.30	6.01	5.55	5.30	5.50
Tb	0.92	0.783	0.839	0.800	0.809	0.751	0.761	0.848	0.811
Dy	5.28	4.67	4.99	4.35	4.8	5.13	4.93	5.17	5.10
Ho	0.98	0.783	0.849	0.821	0.827	0.892	0.867	0.973	0.989
Er	2.56	2.23	2.47	2.27	2.42	2.27	2.22	2.46	2.51
Tm	0.34	0.28	0.294	0.307	0.282	0.285	0.296	0.273	0.332
Yb	2.01	1.682	1.856	1.709	1.873	1.721	1.809	1.91	1.84
Lu	0.279	0.240	0.191	0.255	0.258	0.247	0.258	0.249	0.243
Hf	4.32	3.79	4.04	3.95	4.29	4.24	4.33	4.21	4.04
Ta	1.15	1.077	1.082	0.970	1.097	1.16	1.185	1.067	1.202
Pb	1.7	1.791	1.654	1.472	1.634	1.868	1.688	1.914	1.634
Th	1.22	1.139	1.102	1.176	1.058	1.103	1.011	1.159	1.18
U	0.403	0.425	0.406	0.369	0.390	0.435	0.418	0.369	0.395

Appendix A, Table 2: LA-ICP-MS standards

Session		012815 WWU						
Trace elements (ppm)	**BHVO-2G lit**	BHVO03	BHVO04	BHVO05	BHVO06	BHVO07	BHVO08	BHVO09
Sc	33.0	30.4	30.9	31.3	30.5	30.6	30.7	31.1
Ni	116	126.5	121.6	123.8	120.1	119.4	121.2	122.7
Rb	9.2	9.3	9.29	9.34	8.81	9.06	9.08	9.05
Sr	396	394.1	386.1	391.1	388.2	384.1	387.9	396.8
Y	26	21.6	22.7	23.3	22.6	22.9	22.6	22.9
Zr	170	151.5	151.5	158.7	154.0	156.0	154.7	155.3
Nb	18.3	17.86	17.66	18.16	17.53	17.39	17.69	18.48
Cs	0.2	0.10	0.07	0.09	0.10	0.09	0.09	0.09
Ba	131	133.4	129.5	129.5	128.3	127.7	128.7	131.3
La	15.2	14.46	14.6	14.93	14.78	14.63	14.72	15.25
Ce	37.6	36.7	36.5	37.2	36.1	35.9	36.8	36.9
Pr	5.35	5.18	4.97	5.19	5.15	5.11	5.16	5.25
Nd	24.5	23.1	22.8	23.3	22.3	23.4	23.2	23.5
Sm	6.1	6.08	5.65	6.00	5.95	5.48	6.02	6.22
Eu	2.07	2.05	2.01	2.03	1.93	1.92	2.06	2.02
Gd	6.16	5.84	5.68	5.85	5.86	5.68	5.74	5.47
Tb	0.92	0.879	0.858	0.788	0.82	0.838	0.743	0.803
Dy	5.28	4.73	5.02	4.93	4.89	5.06	4.99	4.58
Ho	0.98	0.825	0.868	0.918	0.879	0.84	0.88	0.858
Er	2.56	2.53	2.5	2.48	2.33	2.39	2.53	2.19
Tm	0.34	0.203	0.308	0.302	0.288	0.287	0.278	0.309
Yb	2.01	1.77	1.731	1.94	1.84	1.84	1.95	2.02
Lu	0.279	0.238	0.257	0.230	0.271	0.258	0.295	0.253
Hf	4.32	4.10	4.13	4.48	3.89	4.26	4.12	4.05
Ta	1.15	1.105	1.114	1.187	1.071	1.077	1.199	1.127
Pb	1.7	1.699	1.712	1.794	1.77	1.603	1.716	1.71
Th	1.22	1.065	1.182	1.102	1.135	1.205	1.189	1.209
U	0.403	0.415	0.456	0.442	0.404	0.452	0.408	0.363

Session		100215 WWU		
Trace elements (ppm)	**BHVO-2G lit**	BHVOA	BHVOB	BHVOC
Sc	33.0	36.4	36.7	36.3
Ni	116	127.0	127.6	129.7
Rb	9.2	9.35	9.36	9.6
Sr	396	405.6	394.8	396.2
Y	26	22.9	23.2	23.0
Zr	170	158.4	158.6	158.0
Nb	18.3	18.06	17.77	18.09
Cs	0.2	0.10	0.10	0.08
Ba	131	134.4	130.6	134.1
La	15.2	15.36	15.25	15.61
Ce	37.6	37.5	36.6	37.0
Pr	5.35	5.26	5.2	5.24
Nd	24.5	23.9	23.8	23.8
Sm	6.1	5.72	5.87	5.95
Eu	2.07	2.03	2.03	2.04
Gd	6.16	5.8	5.85	5.92
Tb	0.92	0.854	0.841	0.859
Dy	5.28	4.99	4.97	4.68
Ho	0.98	0.962	0.927	0.891
Er	2.56	2.47	2.37	2.52
Tm	0.34	0.292	0.287	0.29
Yb	2.01	1.84	1.86	1.9
Lu	0.279	0.254	0.253	0.268
Hf	4.32	4.16	4.17	4.3
Ta	1.15	1.103	1.166	1.041
Pb	1.7	1.616	1.703	1.664
Th	1.22	1.145	1.181	1.229
U	0.403	0.422	0.424	0.456

Session		092716 OSU							
Trace elements (ppm)	**BHVO-2G lit**	BHVO-2g-1	BHVO-2g-2	BHVO-2G-1	BHVO-2G-2	BHVO-2G-1	BHVO-2G-2	BHVO-2G-1	BHVO-2G-2
Sc	33.0	28.5	28.6	36.9	32.7	35.1	40.2	40.6	36.7
Ni	116.0	118.6	130.3	136.9	128.5	122.5	132.2	120.6	120.6
Rb	9.2	9.06	8.51	9.13	8.75	8.78	9.31	8.58	9.32
Sr	396	343.3	349.1	409.5	379.1	403.5	407.3	394.3	405.5
Y	26	19.8	17.1	21.1	20.2	22.1	23.1	21.2	24.8
Zr	170	130.3	118.7	150.1	151.1	157.6	175.0	151.8	161.4
Nb	18.3	14.91	15.03	16.24	15.75	15.92	18.07	18.03	16.41
Cs	0.2		0.09	0.15	0.07	0.09	0.12	0.04	0.08
Ba	131	122.2	119.8	134.7	130.3	129.5	144.0	140.4	130.0
La	15.2	12.44	12.85	15.18	14.16	14.42	15.80	14.58	16.43
Ce	37.6	36.9	34.5	38.5	39.1	36.4	39.5	38.5	36.3
Pr	5.35	4.12	4.67	5.27	4.66	5.30	5.52	4.78	4.89
Nd	24.5	21.4	20.8	23.0	22.5	23.0	24.9	25.5	22.7
Sm	6.1	5.27	4.62	4.75	5.59	5.44	5.89	5.04	6.10
Eu	2.07	2.10	1.86	1.94	1.87	1.83	1.96	1.38	2.21
Gd	6.16	4.72	5.13	5.25	4.86	5.61	5.16	5.12	4.29
Tb	0.92	0.66	0.67	0.75	0.64	0.71	0.77	0.86	0.95
Dy	5.28	4.58	4.06	3.59	4.78	4.48	4.83	5.28	4.83
Ho	0.98	0.67	0.71	0.63	0.60	0.82	0.70	0.90	0.77
Er	2.56	1.81	2.02	2.59	2.22	2.61	2.07	2.11	2.85
Tm	0.34	0.26	0.25	0.18	0.26	0.28	0.31	0.23	0.28
Yb	2.01	1.35	1.20	2.03	1.26	1.85	1.80	1.43	1.95
Lu	0.279	0.14	0.21	0.24	0.23	0.17	0.17	0.29	0.19
Hf	4.32	3.70	2.32	3.38	2.61	4.26	3.74	4.59	3.70
Ta	1.15	0.67	0.91	0.90	0.91	0.67	0.96	0.95	1.06
Pb	1.7	1.32	1.87	2.10	1.46	1.68	2.27	1.68	1.83
Th	1.22	1.00	0.91	0.89	1.19	1.03	0.67	1.08	1.20
U	0.403	0.50	0.42	0.56	0.26	0.36	0.36	0.65	0.39

Appendix A, Table 2: LA-ICP-MS standards

Session		092716 OSU			
Trace elements (ppm)	**BHVO-2G lit**	BHVO-2G-1	BHVO-2G-2	BHVO-2G-1	BHVO-2G-2
Sc	33.0	28.0	31.2	35.4	31.9
Ni	116	129.2	120.7	124.2	126.3
Rb	9.2	8.69	8.07	8.91	8.51
Sr	396	361.4	349.1	374.2	357.2
Y	26	16.8	19.0	18.8	18.8
Zr	170	135.5	136.4	146.9	127.3
Nb	18.3	15.50	14.22	15.83	14.03
Cs	0.2	0.08	0.01	0.07	0.14
Ba	131	125.7	120.6	130.6	122.5
La	15.2	12.24	12.94	14.20	12.36
Ce	37.6	35.3	32.4	35.7	36.0
Pr	5.35	4.67	4.89	4.94	4.71
Nd	24.5	20.0	21.8	22.1	22.5
Sm	6.1	4.34	4.92	5.78	5.52
Eu	2.07	1.82	1.85	1.85	1.69
Gd	6.16	4.98	5.15	5.01	4.76
Tb	0.92	0.69	0.62	0.75	0.68
Dy	5.28	4.36	4.66	4.03	4.05
Ho	0.98	0.54	0.77	0.72	0.70
Er	2.56	2.07	1.28	1.62	2.06
Tm	0.34	0.07	0.26	0.21	0.19
Yb	2.01	1.70	1.23	0.99	1.52
Lu	0.279	0.13	0.15	0.23	0.24
Hf	4.32	2.02	3.93	2.95	2.86
Ta	1.15	0.93	0.75	0.74	0.79
Pb	1.7	1.84	1.49	2.04	1.60
Th	1.22	1.10	1.19	0.84	1.04
U	0.403	0.40	0.42	0.34	0.40

Appendix A, Table 2: LA-ICP-MS standards

Session		092716 OSU							
Trace elements (ppm)	BCR-2G lit	BCR-2g-1	BCR-2g-2	BCR-2G-1	BCR-2G-2	BCR-2G-1	BCR-2G-2	BCR-2G-1	BCR-2G-2
Sc	33.0	33.6	34.6	42.9	41.1	37.8	40.5	46.0	40.7
Ni	13	11.9	13.2	11.4	11.1	11.5	12.3	13.1	11.8
Rb	47	46.66	45.29	42.67	43.67	43.48	41.11	43.59	45.75
Sr	342	313.5	326.8	340.2	344.2	359.4	307.3	364.9	370.1
Y	35	28.3	27.5	31.8	30.9	34.0	32.1	36.1	37.2
Zr	184	166.8	158.6	178.7	182.9	188.5	194.5	188.7	209.6
Nb	12.5	11.05	12.14	11.73	11.61	11.63	11.37	12.69	12.73
Cs	1.16	1.27	0.91	1.18	1.12	1.10	0.97	1.21	1.10
Ba	683	642.7	656.2	695.4	646.3	698.5	645.7	748.0	726.8
La	24.7	23.35	24.09	26.53	23.98	25.03	23.76	26.66	29.59
Ce	53.3	50.2	49.8	52.3	53.1	52.0	48.0	57.7	52.9
Pr	6.7	5.69	6.11	6.93	6.34	6.70	5.55	7.71	6.96
Nd	28.9	25.4	28.0	29.8	26.8	28.5	25.0	30.9	29.2
Sm	6.59	7.06	7.16	6.98	6.95	6.12	6.51	7.88	6.70
Eu	1.97	1.69	1.70	2.18	1.87	1.94	1.79	2.26	2.06
Gd	6.71	6.36	5.72	6.40	7.38	6.50	6.27	6.64	7.61
Tb	1.02	0.90	0.78	1.26	0.84	0.88	0.75	1.00	0.99
Dy	6.44	6.95	4.89	6.13	5.76	5.84	6.91	7.37	6.47
Ho	1.27	0.93	1.31	1.17	1.22	1.36	1.35	1.23	1.39
Er	3.7	3.44	3.17	3.18	3.71	3.94	4.34	3.97	4.54
Tm	0.51	0.43	0.38	0.51	0.44	0.41	0.47	0.56	0.68
Yb	3.39	2.98	3.09	2.96	2.69	2.99	3.23	3.46	3.45
Lu	0.503	0.48	0.47	0.46	0.52	0.45	0.33	0.47	0.56
Hf	4.84	3.82	4.32	5.85	3.46	5.32	4.67	5.36	7.03
Ta	0.78	0.60	0.64	0.61	0.65	0.59	0.71	0.61	0.76
Pb	11	10.55	9.67	10.38	10.09	10.16	8.97	10.90	11.01
Th	5.9	6.05	5.12	6.34	5.68	5.63	5.37	6.74	5.26
U	1.69	1.98	1.57	1.88	1.41	1.59	1.32	1.61	1.72

Appendix A, Table 2: LA-ICP-MS standards

Session		092716 OSU			
Trace elements (ppm)	BCR-2G lit	BCR-2G-1	BCR-2G-2	BCR-2G-1	BCR-2G-2
Sc	33.0	37.1	37.8	42.4	37.2
Ni	13	11.4	11.3	11.2	12.1
Rb	47	44.81	45.97	46.34	43.79
Sr	342	333.8	318.1	348.8	307.5
Y	35	29.3	31.6	34.1	30.7
Zr	184	167.8	178.3	185.6	161.5
Nb	12.5	11.56	11.40	12.53	10.95
Cs	1.16	1.28	1.17	1.11	0.98
Ba	683	652.8	648.5	736.5	644.8
La	24.7	22.52	23.32	25.99	22.54
Ce	53.3	50.7	48.6	53.6	53.1
Pr	6.7	6.21	6.36	6.53	5.92
Nd	28.9	26.8	27.6	30.0	25.8
Sm	6.59	7.87	7.51	7.00	5.58
Eu	1.97	1.90	1.79	2.19	2.01
Gd	6.71	6.48	7.68	5.94	6.14
Tb	1.02	0.82	0.92	0.89	0.94
Dy	6.44	5.78	5.46	6.69	5.13
Ho	1.27	1.01	1.24	1.41	1.10
Er	3.7	3.11	3.16	3.91	3.34
Tm	0.51	0.58	0.43	0.42	0.37
Yb	3.39	2.69	3.09	3.01	3.27
Lu	0.503	0.47	0.42	0.42	0.46
Hf	4.84	4.43	4.72	3.92	4.24
Ta	0.78	0.69	0.63	0.78	0.63
Pb	11	10.48	10.43	10.89	10.78
Th	5.9	5.81	6.40	5.46	5.43
U	1.69	1.74	1.89	1.75	1.83

	JND-1	BCR2	BHVO2	SRM981	SRM981	SRM981	SRM981	SRM981	SRM981
$^{87}Sr/^{86}Sr$		0.705012							
+/- 2 s.e.		18							
$^{143}Nd/^{144}Nd$	0.512104	0.512632	0.512995						
+/- 2 s.e.	9	8	6						
$^{176}Hf/^{177}Hf$		0.282868	0.283104						
+/- 2 s.e.		7	5						
$^{206}Pb/^{204}Pb$				16.938	16.937	16.934	16.934	16.933	16.934
$^{207}Pb/^{204}Pb$				15.491	15.490	15.487	15.488	15.487	15.488
$^{208}Pb/^{204}Pb$				36.716	36.710	36.701	36.703	36.697	36.700

87Sr/86Sr normalised to 88Sr/86Sr=8.37521 and reported relative to SRM987 = 0.710230
143Nd/144Nd normalised to 146/144=0.7219 and reported relative to La Jolla=0.511860
176Hf/177Hf normalised to 179Hf/177Hf = 0.7325 and reported relative to JMC475 = 0.282160
Pb isotope mass bias corrected using thallium doping and reported realtive to SRM981
with 206/204=16.935, 207/204=15.489, 208/204=36.701

Repeated measurements of BHVO-2g standard glass as a secondary standard at the Western Washington University (WWU) LA-ICP-MS facility showed that certain elemental isotopes measured consistently lower than recommended values from Jochum et al., 2005. Because of this, a set of correction factors were developed to correct for WWU instrumental bias. Correction factors were calculated based on average measured values for 44 ablations of BHVO-2g standard glass analyzed over the course of this study, with identical machine operating conditions. The following isotopes were corrected using the factor listed in parentheses: Y-89 (1.154), Zr-90 (1.113), Pr-141 (1.037), Nd-146 (1.060), Sm-147 (1.050), Gd-157 (1.113), Tb-157 (1.119), Dy-163 (1.096), Ho-165 (1.183), Er-166 (1.068), Tm-169 (1.108), Lu-175 (1.121), Ta-181 (1.239). These correction factors were applied to all natural glass data collected on the WWU laser included in this study.
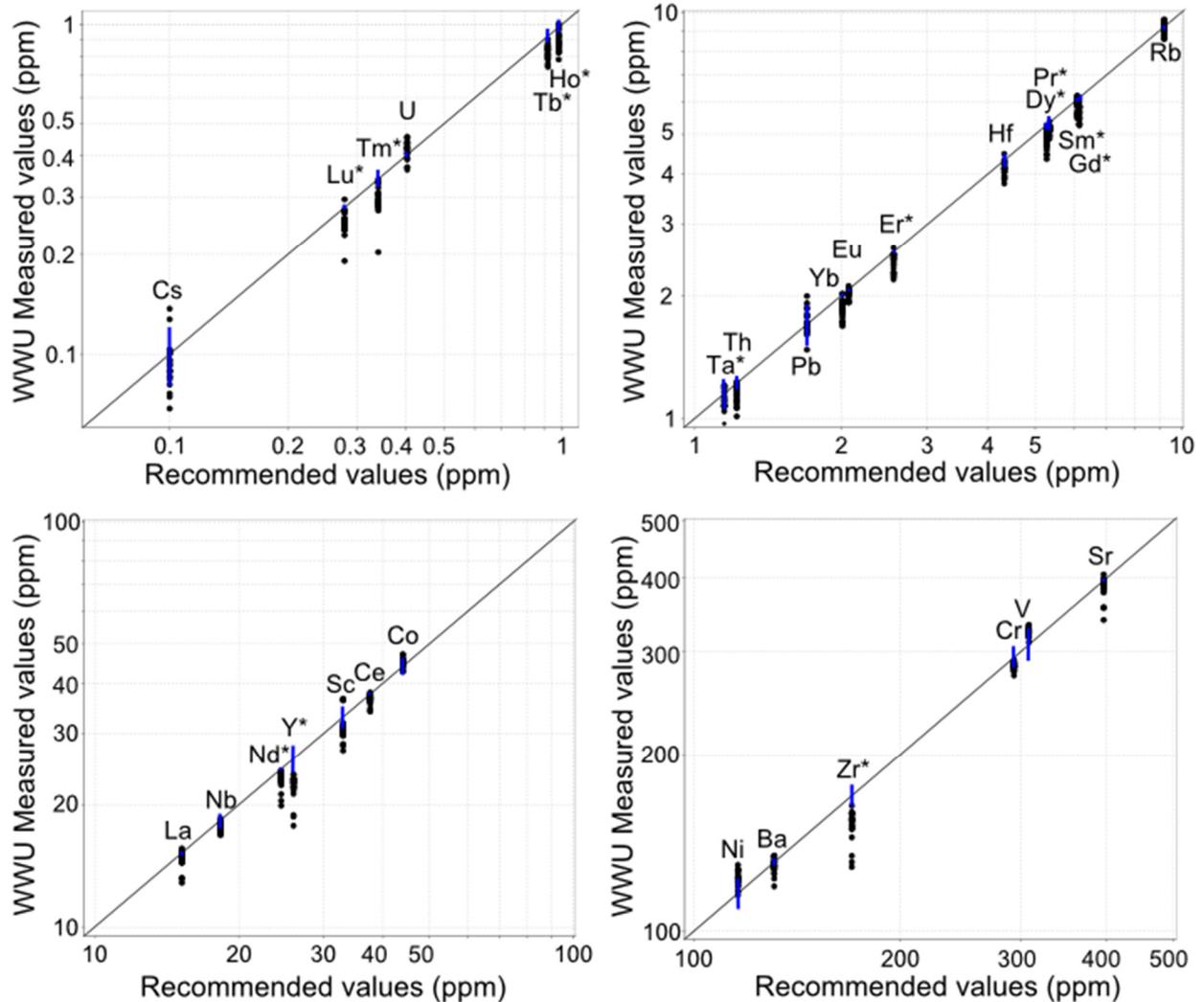
Appendix A, Section 4, figure 1: WWU measured values of BHVO-2g standard glass plotted against recommended values from Jochum et al., 2005 with 1-1 line. Uncertainty on recommended values is shown by a blue vertical bar. Elements indicated with an asterisk were corrected using numerical factors listed in text.

Works cited:

Jochum, K. P., Nohl, U., Herwig, K., Lammel, E., Stoll, B., & Hofmann, A. W. (2005). GeoReM: a new geochemical database for reference materials and isotopic standards. Geostandards and Geoanalytical Research, 29(3), 333–338.

Appendix B, Table 1: Fe-Ti oxide thermometer/fugacity meter

	Interval	D-31r-3-42/43	D-31r-3-42/43	D-31r-3-82/83	D-31r-3-82/83	D-31r-3-82/83	D-28r-2-107/109	D-28r-2-107/109	D-30r-5-129/132	D-30r-5-129/132	B-21f-1-93/94
Ulvospinel	SiO2	0.078	0.086	0.090	0.103	0.085	0.074	0.067	0.065	0.065	0.074
	TiO2	14.3	13.6	14.3	14.4	14.2	9.14	9.12	8.99	8.99	11.1
	Al2O3	2.06	2.09	2.05	2.08	2.06	2.31	2.28	2.02	2.02	3.12
	FeO(T)	74.9	75.6	74.7	75.0	74.8	80.3	79.9	80.4	80.4	74.4
	MnO	1.14	1.07	1.12	1.15	1.07	0.60	0.57	1.04	1.04	0.58
	MgO	1.29	1.30	1.34	1.31	1.24	1.45	1.39	1.38	1.38	2.87
	Cr2O3	0.050	0.032	0.039	0.031	0.036	0.080	0.086	0.033	0.033	0.079
	ZnO	0.215	0.191	0.215	0.163	0.187	0.089	0.087	0.214	0.214	0.123
	V2O3	0.591	0.437	0.524	0.677	0.674	1.908	2.047	0.558	0.558	2.429
	NiO	0.000	0.015	0.042	0.050	0.040	0.030	0.034	0.033	0.033	0.020
Ilmenite	SiO2	0.034	0.000	0.020	0.020	0.020	0.013	0.013	0.019	0.028	0.024
	TiO2	46.9	46.8	47.1	47.1	47.1	44.2	44.2	45.0	43.5	42.5
	Al2O3	0.151	0.170	0.160	0.160	0.160	0.202	0.202	0.146	0.190	0.372
	FeO(T)	48.0	48.2	48.1	48.1	48.1	50.4	50.4	49.8	50.2	49.0
	MnO	1.46	1.37	1.35	1.35	1.35	0.77	0.77	1.37	1.34	0.59
	MgO	2.05	2.05	2.15	2.15	2.15	2.43	2.43	2.31	2.47	3.63
	Cr2O3	0.001	0.010	0.022	0.022	0.022	0.015	0.015	0.007	0.003	0.009
	ZnO	0.028	0.081	0.042	0.042	0.042	0.010	0.010	0.061	0.067	0.015
	V2O3	0.000	0.025	0.000	0.000	0.000	0.526	0.526	0.032	0.110	0.872
	NiO	0.022	0.026	0.020	0.020	0.020	0.006	0.006	0.010	0.008	0.017
	Temp (deg C)	890	882	889	891	889	853	854	840	854	904
	log10 fo2	-12	-12	-12	-12	-12	-12	-12	-12	-12	-11

Appendix B, Table 1: Fe-Ti oxide thermometer/fugacity meter

	Interval	B-35x-2-6/7	B-35x-2-6/7	B-20f-2-101/102	B-20f-2-101/102
Ulvospinel	SiO2	0.096	0.096	0.086	0.085
	TiO2	6.86	6.86	16.6	16.1
	Al2O3	1.60	1.60	2.34	2.52
	FeO(T)	82.1	82.1	73.5	72.1
	MnO	0.81	0.81	0.75	0.76
	MgO	0.95	0.95	1.80	1.88
	Cr2O3	0.060	0.060	0.068	0.029
	ZnO	0.207	0.207	0.177	0.140
	V2O3	1.349	1.349	0.602	0.844
	NiO	0.049	0.049	0.011	0.035
Ilmenite	SiO2	0.018	0.024	0.011	0.011
	TiO2	44.7	43.9	47.5	47.5
	Al2O3	0.141	0.142	0.216	0.216
	FeO(T)	50.9	50.2	47.6	47.6
	MnO	1.25	1.29	0.90	0.90
	MgO	1.87	1.81	2.62	2.62
	Cr2O3	0.025	0.009	0.018	0.018
	ZnO	0.091	0.041	0.065	0.065
	V2O3	0.237	0.264	0.127	0.127
	NiO	0.015	0.029	0.020	0.020
	Temp (deg C)	814	815	930	926
	log10 fo2	-13	-13	-12	-12

Appendix B, Table 2: 2-pyroxene thermometry

	Sample	B-21f-1-93/94	B-21f-1-93/94	B-21f-1-93/94	B-21f-1-93/94	B-33x-1-88/89	D-30r-5-129/132	D-30r-5-129/132	D-30r-5-129/132	D-30r-6-10/11	D-30r-6-10/11	D-30r-6-10/11
Clinopyroxene	SiO2	52.5	52.5	51.3	51.3	48.8	52.1	52.4	52.4	45.8	51.4	45.8
	TiO2	0.286	0.286	0.666	0.666	0.868	0.203	0.186	0.186	2.004	0.560	2.004
	Al2O3	1.14	1.14	2.47	2.47	5.63	1.04	0.77	0.77	8.00	2.17	8.00
	FeO*	14.3	14.3	9.37	9.37	9.28	10.3	17.9	17.9	13.9	10.8	13.9
	MnO	0.72	0.72	0.38	0.38	0.20	1.03	1.59	1.59	0.70	0.99	0.70
	MgO	16.9	16.9	15.0	15.0	13.7	14.3	18.1	18.1	14.1	13.6	14.1
	CaO	13.5	13.5	19.6	19.6	20.6	19.4	8.8	8.8	10.5	19.9	10.5
	Na2O	0.186	0.186	0.302	0.302	0.181	0.270	0.144	0.144	2.002	0.396	2.002
	K2O	0.001	0.001	0.006	0.006	0.020			0.006	0.006		
	Cr2O3	0.007	0.007	0.001	0.001	0.101	0.018	0.001	0.001	0.015	0.016	0.015
Orthopyroxene	SiO2	52.9	54.0	52.9	54.0	52.8	53.3	52.4	53.0	52.5	52.5	52.3
	TiO2	0.208	0.261	0.208	0.261	0.232	0.153	0.148	0.144	0.101	0.101	0.179
	Al2O3	0.749	0.956	0.749	0.956	1.012	0.665	0.452	0.511	0.473	0.473	0.647
	FeO*	22.4	18.5	22.4	18.5	20.1	20.3	21.4	22.4	21.9	21.9	22.5
	MnO	1.18	0.80	1.18	0.80	0.48	1.60	1.87	1.91	1.98	1.98	1.97
	MgO	21.2	24.4	21.2	24.4	20.0	22.5	21.3	21.4	21.5	21.5	21.1
	CaO	1.36	1.52	1.36	1.52	5.56	1.20	1.22	1.17	1.17	1.17	1.23
	Na2O	0.015	0.019	0.015	0.019	0.062	0.018	0.068	0.018	0.027	0.027	0.014
	K2O	0.009	0.006	0.009	0.006	0.003			0.006			0.005
	Cr2O3	0.004	0.001	0.004	0.001	0.009	0.044	0.050	0.000	0.033	0.033	0.005
	T (°C)*	949	1008	892	940	953	849	873	861	847	809	850
	KD(Fe-Mg)	0.797	1.111	0.593	0.826	0.679	0.793	0.988	0.946	0.966	0.776	0.925

*Eq. 36; Putirka, 2008

Appendix B, Table 2: 2-pyroxene thermometry

	Sample	D-30r-6-10/11	D-31r-4-79/81	D-31r-4-79/81	D-31r-4-79/81	D-31r-4-79/81
Clinopyroxene	SiO_2	51.4	51.3	51.6	51.3	51.6
	TiO_2	0.560	0.456	0.296	0.456	0.296
	Al_2O_3	2.17	2.70	1.13	2.70	1.13
	FeO*	10.8	9.90	13.9	9.90	13.9
	MnO	0.99	0.33	1.11	0.33	1.11
	MgO	13.6	14.6	12.7	14.6	12.7
	CaO	19.9	20.2	19.1	20.2	19.1
	Na_2O	0.396	0.298	0.288	0.298	0.288
	K_2O		0.008	0.004	0.008	0.004
	Cr_2O_3	0.016	0.003	0.000	0.003	0.000
Orthopyroxene	SiO_2	52.3	50.2	50.2	51.4	51.4
	TiO_2	0.179	0.217	0.217	0.187	0.187
	Al_2O_3	0.647	0.557	0.557	0.543	0.543
	FeO*	22.5	26.6	26.6	27.3	27.3
	MnO	1.97	1.93	1.93	1.91	1.91
	MgO	21.1	18.2	18.2	17.8	17.8
	CaO	1.23	1.50	1.50	1.47	1.47
	Na_2O	0.014	0.033	0.033	0.036	0.036
	K_2O	0.005			0.007	0.007
	Cr_2O_3	0.005	0.026	0.026	0.000	0.000
	T (°C)*	808	831	846	828	843
	KD(Fe-Mg)	0.743	0.463	0.745	0.440	0.708

*Eq. 36; Putirl

Appendix B, Table 3: Amphibole barometry

Interval	D-30r-5-129/132	D-30r-5-129/132	D-30r-6-10/11
SiO2	46.0	45.2	45.3
TiO2	2.00	2.17	2.24
Al2O3	8.22	8.95	9.06
FeO*	14.2	14.9	14.8
MnO	0.690	0.663	0.633
MgO	13.9	13.3	13.6
CaO	10.9	10.8	10.7
Na2O	1.88	2.01	1.95
K2O	0.199	0.229	0.240
Total	98.0	98.2	98.5
T (°C)	841	858	860
uncertainty (σest)	22	22	22
P (MPa)	142	171	173
uncertainty (Max error)	15.6	18.8	19.0
oceanic depth (km)	5.0	6.0	6.1
ΔNNO	1.2	1.0	1.1
logfO2	-11.8	-11.7	-11.5
uncertainty (σest)	0.4	0.4	0.4
H2Omelt (wt.%)	5.4	5.7	5.6
uncertainty	0.4	0.4	0.8

Appendix B, Table 4 Plagioclase hygrometer

	Interval	B-20f2-101/102	B-21f-1-93/94	B-35x-2-6/7	D-30r-5-129/132	D-31r-4-79/81
	Temp (°C)	928	904	815	847	888
	P (Bars)	1000	1000	1000	1000	1000
Plag	Xan (xtl)	0.673	0.816	0.269	0.459	0.414
Plag	Xab (xtl)	0.327	0.184	0.731	0.541	0.586
Glass	SiO2	66.7	65.4	79.5	74.9	73.6
Glass	TiO2	0.811	0.931	0.179	0.294	0.377
Glass	Al2O3	16.25	16.45	12.76	14.14	14.49
Glass	FeO*	5.36	5.39	1.26	1.97	2.92
Glass	MgO	1.12	1.48	0.190	0.372	0.427
Glass	CaO	4.28	4.86	1.27	1.78	1.69
Glass	Na2O	3.69	3.58	2.47	3.10	3.46
Glass	K2O	1.13	1.14	2.13	3.09	2.72
	wt% H2O calc	4.50	5.68	4.90	5.24	4.44

Appendix C, Table 1: Subtraction modeling

Step 1

Melt fraction (F)	Starting comp	Ending comp
	1.00	0.65
SiO2	50.4	54.4
TiO2	1.60	0.48
Al2O3	13.9	13.7
FeO*	15.0	14.3
MnO	0.24	0.17
MgO	5.38	3.55
CaO	10.5	9.11
Na2O	2.26	3.11
K2O	0.48	0.73
P2O5	0.29	0.44

Step 2

Melt fraction (F)	Starting comp	Ending comp
	0.65	0.30
SiO2	54.4	68.9
TiO2	1.49	-0.35
Al2O3	13.7	15.5
FeO*	14.3	6.33
MnO	0.29	-0.13
MgO	3.55	0.73
CaO	9.11	4.32
Na2O	3.11	5.43
K2O	0.73	1.35
P2O5	0.44	0.31

Step 3

Melt fraction (F)	Starting comp	Ending comp
	0.30	0.225
SiO2	68.9	77.9
TiO2	0.90	0.45
Al2O3	15.5	14.1
FeO*	6.33	3.78
MnO	0.20	0.13
MgO	0.73	0.08
CaO	4.32	0.98
Na2O	5.43	6.77
K2O	1.35	1.79
P2O5	0.31	0.04

Step 1: F = 1.0-0.65

	Total	Cpx74	Cpx69	Opx70	Opx63	An86	Ilm	Ulv
Data source:		1	1	1	1	1	2	2
Modal %	100	18.8	12.0	11.1	5.1	39.3	3.4	10.3
SiO2	42.9	51.8	51.6	53.0	52.9	46.8	0.01	0.09
TiO2	3.67	0.67	0.56	0.29	0.11	0	48.0	17.5
Al2O3	14.4	2.49	2.38	1.34	0.51	33.5	0.22	2.46
FeO*	16.3	9.47	12.12	18.5	22.5	0.61	48.2	77.3
MnO	0.36	0.39	0.36	0.5	1.35	0.02	0.91	0.79
MgO	8.76	15.1	15.0	24.4	21.6	0.05	2.65	1.89
CaO	13.0	19.8	17.7	1.94	1.04	17.5	0	0
Na2O	0.70	0.3	0.24	0.03	0	1.55	0	0
K2O	0.01	0.01	0.01	0.01	0	0.02	0	0
P2O5	0	0	0	0	0	0	0	0

Data sources:

1. Site 1437 core
2. Idealized composition based on mineral formula
3. Johnson, 2007: hornblende from felsic pluton, Talkeetna Arc

Appendix C, Table 1: Subtraction modeling

Step 2: F = 0.65-0.30

	Total	Cpx48	Opx63	Opx45	An86	An76	An40	Ilm	Ulv	Hbld	Apa
Data source:		1	1	1	1	1	1	2	2	3	2
Modal %	100	32.1	2.5	2.0	2.0	28.1	2.0	1.0	13.0	16.0	1.3
SiO_2	41.9	50.6	52.9	50.5	46.8	49.2	58.4	0.0	0.1	46.4	-
TiO_2	3.06	0.3	0.11	0.18	0	0.011	0	48.0	17.5	1.25	0
Al_2O_3	12.1	0.92	0.51	0.52	33.5	31.8	26.3	0.22	2.46	8.46	0.0
FeO*	21.2	19.0	22.5	30.7	0.61	0.76	0.36	48.2	77.3	19.5	0.0
MnO	0.65	1.32	1.35	1.9	0.02	0.0	0	0.91	0.79	0.270	0
MgO	5.98	9.85	21.59	14.44	0.05	0.14	0.02	2.65	1.89	10.5	0
CaO	13.2	17.8	1.04	1.72	17.5	15.5	8.34	0	0	11.5	57
Na_2O	1.11	0.23	0	0.02	1.55	2.5	6.45	0	0	1.11	0
K_2O	0.20	0.02	0	0	0.02	0.08	0.18	0	0	1.02	0
P_2O_5	0.56	0	0	0.01	0	0	0	0	0	0	43

Step 3: F = 0.30-0.225

	Total	Cpx48	Opx45	An86	An76	Ilm	Ulv	Hbld	Apa
Data source:		1	1	1	1	2	2	3	2
Modal %	100	18.6	3.7	11.2	48.5	0.4	11.2	3.7	2.6
SiO_2	42.1	50.6	50.5	46.8	49.2	0.01	0.09	46.4	0
TiO_2	2.24	0.3	0.18	0	0.011	48.03	17.5	1.25	0
Al_2O_3	19.6	0.92	0.52	33.5	31.8	0.22	2.46	8.46	0
FeO*	14.0	19.0	30.7	0.61	0.76	48.2	77.3	19.5	0
MnO	0.42	1.32	1.9	0.02	0.01	0.91	0.79	0.270	0
MgO	2.67	9.85	14.4	0.05	0.14	2.65	1.89	10.5	0
CaO	14.3	17.8	1.72	17.5	15.5	0	0	11.5	57
Na_2O	1.43	0.23	0.02	1.55	2.5	0	0	1.11	0
K_2O	0.04	0.02	0	0.02	0.08	0	0	1.02	0
P_2O_5	1.12	0	0.01	0	0	0	0	0	43

Data sources:

1. Site 1437 core

2. Idealized composition based on mineral formula

3. Johnson, 2007: hornblende from felsic pluton, Talkeetna Arc

Appendix C, Table 2: Trace element modeling

Step 1

Melt fraction (F)	Starting comp 1.00	Ending comp 0.65
Ba	73.18	107.94
La	5.19	7.71
Ce	13.06	19.54
Pr	2.02	3.00
Nd	8.74	12.89
Sm	2.76	3.96
Eu	1.04	1.39
Gd	3.41	4.83
Tb	0.60	0.85
Dy	3.92	5.51
Ho	0.79	1.11
Er	2.21	3.08
Yb	2.20	3.05
Lu	0.32	0.45
Sr	361.73	405.87
Rb	15.42	23.35
Zr	54.71	79.40
K	1996.40	3071.39

Step 2

Melt fraction (F)	Starting comp 0.65	Ending comp 0.30
Ba	107.94	202.95
La	7.71	14.66
Ce	19.54	37.18
Pr	3.00	5.45
Nd	12.89	22.61
Sm	3.96	6.36
Eu	1.39	2.31
Gd	4.83	7.17
Tb	0.85	1.21
Dy	5.51	7.37
Ho	1.11	1.52
Er	3.08	4.33
Yb	3.05	4.43
Lu	0.45	0.65
Sr	405.87	421.60
Rb	23.35	50.06
Zr	79.40	149.06
K	3071.39	6654.67

Step 3

Melt fraction (F)	Starting comp 0.30	Ending comp 0.10
Ba	202.95	292.21
La	14.66	31.84
Ce	37.18	83.99
Pr	5.45	11.67
Nd	22.61	45.86
Sm	6.36	11.40
Eu	2.31	2.36
Gd	7.17	11.75
Tb	1.21	1.96
Dy	7.37	11.80
Ho	1.52	2.50
Er	4.33	7.31
Yb	4.43	7.97
Lu	0.65	1.20
Sr	421.60	0.06
Rb	50.06	140.45
Zr	149.06	358.63
K	6654.67	19964.00

Appendix C, Table 2: Trace element modeling

Step 1: F = 1.0-0.65

Partition coefficients

	Bulk D	Plag	Cpx	Opx	FeTi oxides
Modal %	100	39	31	16	14
Ba	0.098	0.23	0.026	0	0
La	0.080	0.1477	0.056	0.031	0.001
Ce	0.065	0.0815	0.092	0.028	0.002
Pr	0.081	0.0683	0.161	0.028	0.002
Nd	0.098	0.0551	0.23	0.028	0.005
Sm	0.159	0.0394	0.445	0.028	0.007
Eu	0.326	0.443	0.474	0.028	0.011
Gd	0.193	0.031	0.556	0.039	0.016
Tb	0.201	0.027	0.57	0.0575	0.030
Dy	0.208	0.0228	0.582	0.076	0.050
Ho	0.219	0.0215	0.583	0.1145	0.080
Er	0.230	0.0202	0.583	0.153	0.120
Yb	0.244	0.0187	0.542	0.254	0.200
Lu	0.255	0.0187	0.506	0.323	0.280
Sr	0.733	1.83	0.06	0	0.003
Rb	0.037	0.071	0.031	0	0
Zr	0	0	0	0	0
K	0.135	0.048	0.1	0.046	0.56

Appendix C, Table 2: Trace element modeling

Step 2: F = 0.65-0.30
Partition coefficients

	Bulk D	Cpx	Plag	Hbld	FeTi oxides	Opx
Modal %	100	32	32	16	14	5
Ba	0.183	0.02	0.503	0.1	0	0
La	0.17	0.047	0.228	0.5	0.001	0.031
Ce	0.168	0.084	0.136	0.6	0.002	0.028
Pr	0.228	0.133	0.1255	0.9	0.002	0.028
Nd	0.273	0.183	0.115	1.1	0.005	0.028
Sm	0.388	0.377	0.077	1.5	0.007	0.028
Eu	0.342	0.48	0.079	1	0.011	0.028
Gd	0.489	0.583	0.056	1.75	0.016	0.039
Tb	0.536	0.678	0.0505	1.85	0.030	0.0575
Dy	0.625	0.774	0.045	2.2	0.050	0.076
Ho	0.588	0.741	0.0425	2	0.080	0.1145
Er	0.56	0.708	0.04	1.85	0.120	0.153
Yb	0.515	0.633	0	1.7	0.200	0.254
Lu	0.523	0.665	0.046	1.5	0.280	0.323
Sr	0.951	0	2.82	0.3	0.003	0
Rb	0.013	0.016	0.006	0.04	0	0
Zr	0	0	0	0	0	0
K	0.185	0.162	0.01	0.31	0.56	0.046

Appendix C, Table 2: Trace element modeling

Step 3: F = 0.30-0.10

Partition coefficients

	Bulk D	Plag	Cpx	FeTi oxides	Opx	Hbld	Apatite
Modal %	100	58	19.00	12	4	4.00	0.25
Ba	0.668	1.15	0	0	0.03	0	0
La	0.294	0.38	0.015	0.001	0.05	0.8	14.5
Ce	0.258	0.267	0.044	0.002	0.15	0.899	21.1
Pr	0.307	0.235	0.105	0.002	0.185	1.89	26.95
Nd	0.356	0.203	0.166	0.005	0.22	2.89	32.8
Sm	0.469	0.165	0.457	0.007	0.27	3.99	46
Eu	0.984	1.2	0.411	0.011	0.17	3.44	25.5
Gd	0.551	0.125	0.703	0.016	0.34	5.48	43.9
Tb	0.561	0.1185	0.7395	0.030	0.4	5.84	39.35
Dy	0.572	0.112	0.776	0.050	0.46	6.2	34.8
Ho	0.548	0.105	0.7375	0.080	0.555	6.07	28.75
Er	0.523	0.095	0.699	0.120	0.65	5.94	22.7
Yb	0.466	0.09	0.64	0.200	0.86	4.89	15.4
Lu	0.432	0.092	0.683	0.280		4.53	13.8
Sr	9.068	15.633	0	0.003	0.009	0	0
Rb	0.061	0.105	0	0	0.003	0	0
Zr	0	0	0	0	0	0	0
K	0.201	0.135	0.184	0.56	0.2	0.31	0.000

Appendix C, Table 3. Partition Coefficients

Step 1

	Plagio-clase	Clino-pyroxene	Ortho-pyroxene	Fe-Ti oxides
Ba	0.23	0.026		
La	0.1477	0.056	0.031	0.001
Ce	0.0815	0.092	0.028	0.002
Pr	0.0683	0.161	0.028	0.002
Nd	0.0551	0.23	0.028	0.005
Sm	0.0394	0.445	0.028	0.007
Eu	1.1255	0.474	0.028	0.011
Gd	0.031	0.556	0.039	0.016
Tb	0.027	0.57	0.0575	0.030
Dy	0.0228	0.582	0.076	0.050
Ho	0.0215	0.583	0.1145	0.080
Er	0.0202	0.583	0.153	0.120
Yb	0.0187	0.542	0.254	0.200
Lu	0.0187	0.506	0.323	0.280
Sr	1.83	0.06		0.003
Rb	0.071	0.031		
Zr	0.048	0.1	0.046	0.56
Data sources	1,2	1,2	2,3	4

Sources   Grey indicates partition coefficients interpolated from literature

1. Rollinson, 1993
2. Fujimaki et al., 1984
3. Pearce and Norry, 1979
4. Klemme et al., 2006
5. Greene and Pearson, 1985
6. Nash and Crecraft, 1985
7. Arth, 1976
8. Watson and Harris, 1983
9. Drake and Weill, 1975
10. Wilke and Behrens, 1999
11. Gill, 1981

Step 2

	Plagio-clase	Clino-pyroxene	Ortho-pyroxene	Fe-Ti oxides	Horn-blende
Ba	0.503	0.02			0.1
La	0.228	0.047	0.031	0.001	0.5
Ce	0.136	0.084	0.028	0.002	0.6
Pr	0.1255	0.133	0.028	0.002	0.9
Nd	0.115	0.183	0.028	0.005	1.1
Sm	0.077	0.377	0.028	0.007	1.5
Eu	0.079	0.48	0.028	0.011	1
Gd	0.056	0.583	0.039	0.016	1.75
Tb	0.0505	0.678	0.0575	0.030	1.85
Dy	0.045	0.774	0.076	0.050	2.2
Ho	0.0425	0.741	0.1145	0.080	2
Er	0.04	0.708	0.153	0.120	1.85
Yb		0.633	0.254	0.200	1.7
Lu	0.046	0.665	0.323	0.280	1.5
Sr	2.82			0.003	0.3
Rb	0.006	0.016			0.04
Zr	0.01	0.162	0.046	0.56	1.4
Data sources	9, 11	2, 3, 11	2, 3	4	5

Sources   Grey indicates partition coefficients interpolated from literature

1. Rollinson, 1993
2. Fujimaki et al., 1984
3. Pearce and Norry, 1979
4. Klemme et al., 2006
5. Greene and Pearson, 1985
6. Nash and Crecraft, 1985
7. Arth, 1976
8. Watson and Harris, 1983
9. Drake and Weill, 1975
10. Wilke and Behrens, 1999
11. Gill, 1981

Step 3

	Plagio-clase	Clino-pyroxene	Ortho-pyroxene	Fe-Ti oxides	Horn-blende	Apatite
Ba	1.15		0.03			
La	0.38	0.015	0.05	0.001	0.8	14.5
Ce	0.267	0.044	0.15	0.002	0.899	21.1
Pr	0.235	0.105	0.185	0.002	1.89	26.95
Nd	0.203	0.166	0.22	0.005	2.89	32.8
Sm	0.165	0.457	0.27	0.007	3.99	46
Eu	1.2	0.411	0.17	0.011	3.44	25.5
Gd	0.125	0.703	0.34	0.016	5.48	43.9
Tb	0.1185	0.7395	0.4	0.030	5.84	39.35
Dy	0.112	0.776	0.46	0.050	6.2	34.8
Ho	0.105	0.7375	0.555	0.080	6.07	28.75
Er	0.095	0.699	0.65	0.120	5.94	22.7
Yb	0.09	0.64	0.86	0.200	4.89	15.4
Lu	0.092	0.683	0.9	0.280	4.53	13.8
Sr	15.633		0.009	0.003		
Rb	0.105		0.003			
Zr	0.135	0.184	0.2	0.56	0.31	
Data sources	6, 10	2, 3	3, 7	4	7, 8	2

Sources   Grey indicates partition coefficients interpolated from literature
1. Rollinson, 1993
2. Fujimaki et al., 1984
3. Pearce and Norry, 1979
4. Klemme et al., 2006
5. Greene and Pearson, 1985
6. Nash and Crecraft, 1985
7. Arth, 1976
8. Watson and Harris, 1983
9. Drake and Weill, 1975
10. Wilke and Behrens, 1999
11. Gill, 1981